Zinc Oxide Nanostructures with Carbon Nanotube and Gold Additives for CO Gas Sensing Application

DISSERTATION

Submitted in fulfilment of the requirements for

MASTER'S DEGREE

OF

CHEMICAL ENGINEERING TECHNOLOGY

In the

FACULTY OF ENGINEERING AND BUILT ENVIRONMENT

At the

UNIVERSITY OF JOHANNESBURG

By

CHAUKE HLEKO

SUPERVISOR: Prof. K Moothi

CO-SUPERVISORS: Dr SG Nyembe and Dr SP Malinga

2019

DECLARATION

I declare that this thesis is my own original work under the supervision of Professor Kapil Moothi (University of Johannesburg), Dr Sanele Nyembe (Mintek) and Dr Soraya Malinga (University of Johannesburg). It is being submitted for the degree of Master of Technology in Chemical Engineering to the University of Johannesburg, Johannesburg South Africa. It has not been submitted before for any degree or examination at any University.

Hleko Chauke

Signature: ……

Date: …….

ABSTRACT

Zinc oxide (ZnO) nanostructures were synthesised for gas sensing application. In an attempt to improve the surface area and the electrical conductivity of the ZnO, nanomaterials such as the carbon nanotubes (CNTs) and gold nanoparticles (AuNPs) were used separately to produce CNTs/ZnO and Au/ZnO nanocomposites, respectively. The addition of these nanomaterials onto the ZnO nanostructures significantly improved the gas sensing properties such as the sensitivity and response time. Synthesis of gold nanoparticles was successfully achieved via gold salt ($HAuCl_4.3H_2O$) reduction using the Turkevich method. Citrate molecules were used as the stabiliser and to systematically control the sizes of the AuNPs. The sizes of AuNPs were found to increase from 14 nm to 40 nm when the concentration of citrate ions was reduced from 1 mM to 0.3 mM. The size distribution of AuNPs was relatively wider as the particle size increased. The synthesized AuNPs were stable for over a period of 4 weeks.

Carbon nanotubes synthesis was achieved using chemical vapour deposition (CVD) method using acetylene gas as the carbon source and ferrocene as the catalyst. An increase in the flowrate of the precursor gas (acetylene) yielded an increase in amorphous carbon, which was attached to the walls of the carbon nanotubes. The optimum flowrate of acetylene was found to be 150 m^3/min that yielded CNTs with an average diameter of 95 nm and a relatively narrow size distribution.

The hydrothermal chemical precipitation method was used to synthesise ZnO nanostructures. Zinc sulphate ($ZnSO_4$) and sodium hydroxide (NaOH) were used as a metal precursor and reducing agent, respectively. The NaOH concentration of 0.3 M yielded ZnO nanosheets with relatively the highest surface area of 102 m^2/g. Gas sensing analysis was conducted using carbon monoxide (CO) gas at 250°C. The sensitivity and response time were calculated to be 9.8% and 114 seconds, respectively, at a CO concentration of 200 ppm.

The composites CNTs/ZnO and Au/ZnO were prepared, separately. The average surface area of the Au/ZnO composite was 131 m^2/g and that of CNTs/ZnO composite was 153 m^2/g. The CNTs/ZnO composite showed an optimum sensitivity of 9.9% and the response time of 49 seconds when exposed to 200 ppm of CO gas at 250°C.

KEYWORDS

Zinc oxide, Gold nanoparticles, Carbon nanotubes, Microwave digestion, Turkevich method, Chemical vapour deposition, Gas sensing, Response time, Sensitivity, Transmission Electron Microscopy.

DEDICATION

This work is dedicated to my loving mother, Ms Maria Tintswalo Chauke and my entire family.

ACKNOWLEDGEMENTS

I give many thanks to the Almighty God, for his steadfast love endures forever. Mark 9:23

I would like to thank my co-supervisor Dr Sanele Nyembe for his daily guidance throughout the project. Taking your precious time even some time to spend with your family and dedicated it to helping me with the project. Thank you very much for sharing your experience and hints with me.

I would like to extend my sincere gratitude to my supervisors; Prof Kapil Moothi and Dr Soraya Malinga for their guidance and unwavering support throughout this study.

I would like to thank my mother Maria Tintswalo Chauke for her unconditional love and support throughout my project. I would to thank her for her daily prayers.

I would like to extend my gratitude to my partner Abigail Koena Moloto, for her support and input in my research project.

I would like to acknowledge Mintek, Nanotechnology Innovation Centre (NIC) team for their contribution, Dr Lucky Sikhwivhilu and Dr Gebhu Ndlovu for their support.

I would like to acknowledge the University of Johannesburg.

I would like to acknowledge the National Research Foundation (NRF) for financial assistance throughout my project.

LIST OF PRESENTATIONS

Oral Presentations

- H. Chauke, S. Nyembe, S. Malinga, K. Moothi
  Annual Postgraduate Research Conference 2018, University of Johannesburg, Postgraduate School, **19 October 2018**: Effects of Physical Properties of Nanomaterials on Gas Sensing Performance.

- H. Chauke, S. Nyembe, S. Malinga, K. Moothi
  8th Annual Gauteng Nanoscience Young Researchers Symposium (NYRS), Vaal University of Technology, the Quest Conference Estate (Vanderbijlpark), **16 November 2018**: Effects of Physical Properties of Nanomaterials on Gas Sensing Performance.

- H. Chauke, S. Malinga, S. Nyembe, K. Moothi
  Nanotechnology Innovation Centre (NIC) Group Meeting, Mintek/Advanced Materials Division (AMD) Meeting Room, Randburg on **03 December 2018**: Synthesis and Characterization of ZnO with additives (gold nanoparticles and carbon nanotubes).

- H. Chauke, S. Malinga, S. Nyembe, K. Moothi
  Nanotechnology Innovation Centre (NIC) Group Meeting, Mintek/Advanced Materials Division (AMD) Meeting Room, Randburg, **29 March 2019**: Gas sensing performance of carbon nanotubes/zinc oxide composite.

Poster Presentation

- H. Chauke, S. Malinga, S. Nyembe, K. Moothi
  DST Nanotechnology Innovation Centre's 10-year Anniversary Workshop, CSIR International Convention Centre, Pretoria, **14-16 October 2018:** The Effect of Zinc Oxide Morphology on the Physical and Structural Properties.

- H. Chauke, S. Malinga, S. Nyembe, K. Moothi
  Conference of the South African Advanced Materials Initiative (CosAAmi), Riverside Sun, Vanderbijlpark, Johannesburg, **22-25 October 2019:** Zinc oxide Nanosheets functionalized by carbon nanotubes for CO gas sensors.

Awards and Recognition

Best Oral Presentation (MTech 3rd Prize)

- H. Chauke, S. Nyembe, S. Malinga, K. Moothi
  8th Annual Gauteng Nanoscience Young Researchers Symposium (NYRS), Vaal University of Technology, the Quest Conference Estate (Vanderbijlpark), **16 November 2018:** Effects of Physical Properties of Nanomaterials on Gas Sensing Performance.

Publications

- H. Chauke, S. Malinga, S. Nyembe, K. Moothi, Zinc oxide nanosheets functionalized by carbon nanotubes for CO gas sensors, Materials Science and Engineering Journal. (**Submitted for Review**)

LIST OF ACRONYMS

ZnO	Zinc Oxide
AuNPs	Gold Nanoparticles
CNTs	Carbon Nanotubes
CVD	Chemical Vapour Deposition
XRD	X-ray Diffraction
TEM	Transmission Electron Microscope
CO	Carbon Monoxide
UV-Vis	Ultraviolet-Visible Spectroscope
FTIR	Fourier Transform Infrared Spectroscope
BET	Brunauer- Emmett –Teller

TABLE OF CONTENT

LIST OF FIGURES

LIST OF TABLES

CHAPTER 1

1.0 General Introduction

In recent years, there has been a considerable increase in the attention of nanomaterials with gas sensing capabilities, with the number of publications almost doubling every 2 to 3 years. This interest is due to undesired high response time and high operating temperatures experienced by most conventional gas sensing materials such as polymer thin films [1-2]. Furthermore, there is a growing need for accurate, reliable, low cost and portable gas sensors to enhance the safety of living organisms against toxic gases in industries and households [1-3]. Toxic gases can be emitted from industries such as the mining industry. Some households use natural gases which requires environmental monitoring. In recent years, the concentration of gases in the atmosphere has increased dramatically mainly due to urbanisation, which has increased the combustion of fossil fuels [3-6]. The combustion of fossil fuels drastically increases emissions of toxic gases such as; ammonia (NH_3), hydrogen sulphide (H_2S) and carbon monoxide (CO). The combustion of fossil fuels often releases mixed gases at low concentrations which increases the need for a highly sensitive and selective gas sensing materials [7].

There are various gas sensors which have been used to combat the increased emissions of toxic gases based on different sensing mechanisms such as optic, electrical variation, acoustic, gas chromatography (GC) and calorimetric methods [8]. These sensing mechanisms can be employed in different gas sensors such as electrochemical, polymer, surface acoustic wave (SAW), thermal conductive, solid electrolyte, carbon nanomaterials and semiconductor metal oxides (SMOs), each with a different functionality [11-12]. The effectiveness of each sensor depends on the efficiency and ability to discriminate between small concentrations (sensitivity) of different gases (selectivity) [8-9]. However, the performance of gas sensors can also be measured by parameters such as response time, recovery time and stability [10].

Nanomaterials have gained greater interest because of their unique properties such as electrical conductivity, high surface area, high mechanical strength, relatively wide bandgap and high surface area to volume ratio, hence the high number binding sites for gas molecules. The relatively high electrical conductivity and wide bandgap of nanomaterials make them ideal for gas sensing applications [1, 11].

The commonly used gas sensing nanomaterials are the SMOs such as Tin dioxide (SnO_2) and carbon-based materials such as carbon nanotubes (CNTs) because their electrical conductivities are easily changed when gas molecules are attached on their surfaces. The SMOs (ZnO, SnO_2, Titanium dioxide (TiO_2)) are ideal for gas sensing because of their properties such as high surface area, high electrical conductivity, bandgap of around 3.4 eV, low cost and stability [5,12]. The SMOs mechanism to detect gases is based on the change of electrical conductivity which changes due to interaction with surrounding gases.

The SMOs are divided into two groups which are; SMOs which follow bulk conductance and SMOs which follow surface conductance effects. SMOs that follow bulk conductance operates at high temperature (>700ºC) and some of the examples are TiO_2, Cerium (IV) oxide (CeO_2) and Niobium pentoxide (Nb_2O_5) because they respond to the changes in environmental oxygen partial pressure [12]. The second group of SMOs perform gas sensing at temperatures ranging from 300ºC to 600ºC, with examples being SnO_2 and ZnO [13-15]. Often the SMOs are doped with metals or small elements such as carbon (C) and sulphur (S), noble metals such as gold (Au), silver (Ag) and palladium (Pd) to enhance their gas sensing performance [16]. This surface modification by noble metals increases the electrical variation of the SMOs, therefore, provide a potential of improving gas sensing parameters such as response time, recovery time and sensitivity [16].

ZnO is a multifunctional SMO due to its unique properties. Gas sensors based on ZnO materials have numerous advantages such as low cost, high sensitivity and improved life span. ZnO can be synthesised in different morphologies, which affects gas sensing performance [6, 14, 16]. Previously ZnO has been incorporated with metal nanoparticles such as AuNPs, Pt, Ag and carbon-based materials to improve their gas adsorption, hence improving their gas sensing performance [17-19].

CNTs have also been investigated for gas detection by various researchers because of unique properties such as geometry and morphology [20]. Electrical properties and morphology of CNTs are altered upon contact with some gases which makes CNTs a suitable material for gas sensing [20-23]. The CNTs are sensitive to gases such as NO_3 and NH_3 because of the change in electrical conductivity of the CNTs as a result of gas adsorption on the surface [9, 16, 23]. Furthermore, properties such as high surface area and high aspect ratio enable the CNTs to detect smaller concentration (sensitivity) of gas molecules as compared to other gas sensing

materials [24]. Currently, there are different gas sensors based on CNTs such as sorption gas sensors, ionisation gas sensors, capacitance gas sensors and resonance shift gas sensors [20].

1.1 Problem Statement

Industrial gas emissions are often harmful to living organisms and the surrounding atmosphere. Some of these gases such as CO are toxic, odourless and colourless, these characteristics make these gases highly harmful to living organisms. Hence there is a need to develop gas sensing materials that can be able to selectively detect gases at low concentrations and subsequently respond timeously [24-26]. Nanostructures of different shapes have been reported to have an effect on gas sensing parameters such as selectivity, sensitivity and response time [16-17]. ZnO has been reported to have disadvantages of being unstable at higher temperatures and have high response times. To address this issue, ZnO with different morphologies will be synthesised. Additives such as AuNPs and CNTs will be added to the ZnO, which has the potential to increase electrical conductivity and surface area, potentially improving the sensing performance [27-28].

1.2 Aim and Objectives

The aim of the study is to investigate the effect of AuNPs and CNTs as additives to ZnO on gas sensing performance.

Objectives are as follows:

- To synthesize ZnO nanomaterials using a hydrothermal method.
- To investigate the chemical, structural and physical properties of the ZnO using characterization techniques such as XRD, BET, UV-Vis, FTIR and Raman.
- To make two composites of ZnO with CNTs and ZnO with AuNPs.
- To investigate the interaction of the CNTs and AuNPs with the ZnO using transmission electron microscopy.
- To determine the gas sensing performance of pristine ZnO and the composites.

1.3 Thesis Outline

Chapter 1 outlines the background of the study which includes the problem statement, the aim and the objectives to achieve the aim. **Chapter 2** covers the literature review of semiconductor metal oxides and their gas sensing performances, carbon-based materials and metal nanoparticles. In-depth explanations of the characterisation techniques are covered in **Chapter 3**. **Chapter 4** explains the synthesis and characterisation of gold nanoparticles (AuNPs) and carbon nanotubes (CNTs) additives. The synthesis and characterisation of ZnO and its gas sensing performance in terms of sensitivity and response time are explained in **Chapter 5.** The synthesis of the Au/ZnO and CNT/ZnO composites and their gas sensing performance was compared to that of pure ZnO and is discussed in **Chapter 6**. **Chapter 7** covers the general conclusions and recommendations.

1.4 References

[1] Dey, A. (2018). Semiconductor metal oxide gas sensors: A review. Materials Science and Engineering: B, 229, pp.206-217.

[2] Madhusoodanan, K., Vimalkumar, T. and Vijayakumar, K. (2018). Gas sensing application of nanocrystalline zinc oxide thin films prepared by spray pyrolysis, Bulletin of Material Science, 38 (3), pp.583-591.

[3] Liu, X., Cheng, S., Liu, H., Hu, S., Zhang, D. and Ning, H. (2012). A survey on gas sensing technology. Sensors, 12 (7), pp.9635-9665.

[4] Wang, Y. and Yeow, J. (2009). A review of carbon nanotubes-based gas sensors. Journal of Sensors, 40, pp.1-24.

[5] Gupta, B.D, Shrivastav, A.M, Usha, S.P (2016). Surface plasmon resonance-based fiber optic sensors utilizing molecular imprinting. Sensors, 16(9), pp.1381-1390.

[6] Llobet, E. (2013). Gas sensors using carbon nanomaterials: A review. Sensors and Actuators B: Chemical, 179, pp.32-45.

[7] Wang, C., Yin, L., Zhang, L., Xiang, D. and Gao, R. (2010). Metal oxide gas sensors: sensitivity and influencing factors. Sensors, 10(3), pp.2088-2106.

[8] Li, J., Lu, Y., Ye, Q., Cinke, M., Han, J. and Meyyappan, M. (2003). Carbon nanotube sensors for gas and organic vapour detection. Nano Letters, 3(7), pp.929-933.

[9] Vairavapandian, D., Vichchulada, P. and Lay, M. (2008). Preparation and modification of carbon nanotubes: Review of recent advances and applications in catalysis and sensing. Analytica Chimica Acta, 626(2), pp.119-129.

[10] Pal Singh, R., Hudiara, I. and Bhushan Rana, S. (2016). Effect of calcination temperature on the structural, optical and magnetic properties of pure and Fe-doped ZnO nanoparticles. Materials Science-Poland, 34(2), pp.451-459.

[11] Maruthupandy, M., Zuo, Y., Chen, J., Song, J., Niu, H., Mao, C., Zhang, S. and Shen, Y. (2017). Synthesis of metal oxide nanoparticles (CuO and ZnO NPs) via biological template and their optical sensor applications. Applied Surface Science, 397, pp.167-174.

[12] Hasanpoor, M., Aliofkhazraei, M. and Delavari, H. (2015). Microwave-assisted synthesis of zinc oxide nanoparticles. Procedia Materials Science, 11, pp.320-325.

[13] Zhou, X., Cheng, X., Zhu, Y., Elzatahry, A., Alghamdi, A., Deng, Y. and Zhao, D. (2018). Ordered porous metal oxide semiconductors for gas sensing. Chinese Chemical Letters, 29(3), pp.405-416

[14] Zaporotskova, I., Boroznina, N., Parkhomenko, Y. and Kozhitov, L. (2016). Carbon nanotubes: Sensor properties. A review. Modern Electronic Materials, 2(4), pp.95-105.

[15] Chang, S., Hsueh, T., Chen, I. and Huang, B. (2008). Highly sensitive ZnO nanowire CO sensors with the adsorption of Au nanoparticles. Nanotechnology, 19(17), p.175-190.

[16] Shingange, K., Tshabalala, Z., Ntwaeaborwa, O., Motaung, D. and Mhlongo, G. (2016). Highly selective NH_3 gas sensor based on Au loaded ZnO nanostructures prepared using microwave-assisted method. Journal of Colloid and Interface Science, 479, pp.127-138.

[17] Shingange, K., Swart, H. and Mhlongo, G. (2018). Au functionalized ZnO rose-like hierarchical structures and their enhanced NO_2 sensing performance. Physica B: Condensed Matter, 535, pp.216-220.

[18] Wang, Z. (2004). Zinc oxide nanostructures: growth, properties and applications. Journal of Physics: Condensed Matter, 16(25), pp.829-858.

[19] Baskoutas, S. (2018). Special Issue: Zinc oxide nanostructures: synthesis and characterization. Materials, 11(6), p.873-875.

[20] Fan, Z. and Lu, J. (2005). Zinc oxide nanostructures: synthesis and properties. Journal of Nanoscience and Nanotechnology, 5(10), pp.1561-1573.

[21] Wang, P., Liu, D. and Li, D. (2012). Hydrothermal synthesis of different zinc oxide nanostructures: growth, structure and gas sensing properties. Materials Transactions, 53(11), pp.1892-1895.

[22] Al Rifai, S. and Domashevskaya, E. (2013). The synthesis and optical properties of different zinc oxide nanostructures. Russian Journal of Physical Chemistry A, 87(13), pp.2246-2252.

[23] Kumar, S., Pavelyev, V., Mishra, P. and Tripathi, N. (2018). A review on chemiresistive gas sensors based on carbon nanotubes: Device and technology transformation. Sensors and Actuators A: Physical, 283, pp.174-186.

[24] Aroutiounian, V. (2016). Metal oxide gas sensors decorated with carbon nanotubes. Lithuanian Journal of Physics, 55(4). pp. 500-550

[25] Shingange, K., Mhlongo, G., Motaung, D. and Ntwaeaborwa, O. (2016). Tailoring the sensing properties of microwave-assisted grown ZnO nanorods: Effect of irradiation time on luminescence and magnetic behaviour. Journal of Alloys and Compounds, 657, pp.917-926.

[26] Slobodian, P., Riha, P., Lengalova, A., Svoboda, P. and Saha, P. (2011). Multi-wall carbon nanotube networks as potential resistive gas sensors for organic vapour detection. Carbon, 49(7), pp.2499-2507.

[27] Badhulika, S., Myung, N. and Mulchandani, A. (2014). Conducting polymer coated single-walled carbon nanotube gas sensors for the detection of volatile organic compounds. Talanta, 123, pp.109-114.

[28] Xu, K., Wu, C., Tian, X., Liu, J., Li, M., Zhang, Y. and Dong, Z. (2012). Single-walled carbon nanotube-based gas sensors for NO_2 detection. Integrated Ferroelectrics, 135(1), pp.132-137.

CHAPTER 2

2.0 Literature Review

2.1 Introduction

The detection and monitoring of toxic gases in the mines and atmosphere is important for life preservation and environmental safeguard. Reliable and portable gas sensors are in demand because of their wide applications in industries and for indoor air quality [1-2]. A gas sensor that is highly sensitive and selective is ideal and this has led to a search for suitable materials. SMOs are the most investigated gas sensing material because they offer high surface area to volume ratio, hence the high number of gas binding sites which are both important for gas adsorption and subsequently detection [1-3]. Most studies have focused on detection of gases such as CO_2, CO, SO_2, O_3, O_2, H_2 and organic vapours because of their toxicity in the atmosphere which affects humans and are found in high levels in the atmosphere [2-3]. Current disadvantages of commercial gas sensors are high operating temperatures and high response times [3-4].

2.2 Background

A gas sensor is a device that can be used to quantify and detect different types of gases in the atmosphere, an example is environmental monitoring. The development of a gas sensor is promoted by the increasing need to test the levels of toxic gases during daily activities either in households or the workplace. These sensors can be made from different materials such as SMOs and CNTs. Dey *et al* [1] and other researchers defined a gas/chemical sensor as a device that translates chemical data into an analytical signal [5-7]. Gas/chemical also provides important information about the composition of the gases in the environment [7-8]. They contain a physical transducer and a chemically selective layer. There are several transducer modes that can be incorporated into gas sensors such as thermal, optical and electrochemical. The output of the gas sensors is measured by the change in electrical resistance [9]. A gas sensor consists of two main components which are; the receptor part which transforms the chemical information into electrical energy and the physical transducer which converts the electrical energy into a signal [8-10].

There are different types of gas sensors made from nanomaterials including carbon nanomaterials and SMOs which are; capacitance sensors, mass sensitivity sensors, calorimetric sensors and solid-state ionic sensors. However, the most commercially used gas sensors are optical, electrochemical and chemi-resistive [10-13]. Optical gas sensors have exhibited

desirable characteristics such as high sensitivity and selectivity. However, they are expensive to fabricate which limits their applications [14]. The electrochemical sensors have low stability which also limits its application. The most commercially available gas sensors are the chemi-resistive, despite their disadvantages of low selectivity and relatively high response times [12-15].

2.2.1 Chemi-resistive Sensors

The chemi-resistive sensors have gained more interest in the past decades because of their properties such as low operational cost, smaller size (potable) and low cost of fabrication [16-18]. The chemi-resistive gas sensors operate based on electrical resistance variation that is caused by the reaction between the sensing material and the gas molecules. These types of gas sensors have the potential to be applied in different applications such as environmental monitoring, and space emissions transportation. [18]. Chemi-resistive sensors have been used to monitor different gases such as NH_3, NO_2, NO, H_2S, Cl_2 and CO, using different types of nanomaterials such as SMOs, carbon-based materials and hybrid materials [6, 18-20]. Among these materials, the SMOs present a good opportunity for use in the chemi-resistive gas sensors, however, it has disadvantages such as high operational temperature. This limits its application at room temperature environment and also decreases the stability of the sensor in terms of life span. The use of SMOs based gas sensor in sensing of gas and vapour with a low boiling point can cause a fire when it comes in contact with the SMOs hot surface [21-23]. Working at low temperatures for a gas sensor is more desirable in a work-place.

2.2.2 Characteristics of a Gas Sensor

The performance of a gas sensor is measured in terms of different characteristics such as selectivity, sensitivity, response time, recovery time, stability and detection limit [13-15].

Selectivity is defined as the capability of a gas sensor to detect a specific gas in the presence of other gases. An example is CO gas sensor which does not show response to other gases like CO_2 [13]. Selectivity can be expressed in terms of gas of interest over other gases, as shown in Equation 2.1.

$$selectivity = \frac{sensitivity\ of\ gasA}{sensitivity\ of\ gasB} \ldots\ldots\ldots\ldots\ldots\ldots (2.1)$$

Sensitivity can be explained as the lowest gas concentration that a certain gas sensor can detect at a given time. It can be expressed as R_g/R_a for reducing gases and R_a/R_g for oxidizing gases where R_a stands for the resistance of a gas sensor in the reference gas, which is commonly air

and R_g is resistance of a gas sensor in the presence of a target gas [11], and the overall sensitivity is expressed in Equation 2.2.

$$Sensitivity\ (\%) = \left[\frac{R_a - R_g}{R_a}\right] \times 100 \ldots\ldots\ldots\ldots\ldots\ldots (2.2)$$

Response time is defined as the time it takes for a gas sensor to generate a corresponding signal after the gas concentration reached a specific value [1]. Recovery time, also referred to as settling time is defined as the time taken by the signal of the sensor to return to its initial value within a certain percentage of the steady-state value [23]. Stability is defined as the ability of a sensor to reproduce the same output value when measuring the same input over a certain period. This involves maintaining the sensor selectivity, sensitivity and response time [22-23]. The detection limit is defined as the lowest gas concentration that can be detected by the sensors under a given temperature. The detection limit is shown in Equation 2.3 [21-23]. The $noise_{rms}$ (Equation 2.3) is determined by calculating the sensor noise in the gas response at baseline using the root mean square deviations (rms) and the slope is the first derivative of the response versus gas concentration graph [24-25].

$$Detection\ limit = 3\left[\frac{noise_{rms}}{slope}\right] \ldots\ldots\ldots\ldots\ldots\ldots\ldots\ldots\ldots (2.3)$$

2.2.3 Nanomaterials

Nanomaterials are defined as materials which have at least one dimension with a diameter of less than 100 nm. Nanomaterials have high surface areas. Their properties are altered and enhanced at a nanoscale, this increases their application in different fields such as water treatment, gas sensing and the energy sector [1]. Other properties include relatively high electrical conductivity and small bandgap, making them suitable for gas sensing [21]. There are different types of nanomaterials such as SMOs and carbon-based like carbon nanotubes (CNTs) that have been used successfully for gas sensing applications.

2.2.4 Semiconductor Metal Oxide (SMOs)

SMOs embody properties such as electrical conductivity, avarage bandgap and high surface area which are ideal for a gas sensor [31-32]. The SMOs are used widely to detect gases because of their low cost of production and reliability. There are different types of SMOs such as ZnO, SnO_2, TiO_2 and WO_2 which have been used as gas sensing nanomaterials [32]. The mechanism of SMOs to detect gases is based on the change in electrical conductivity which changes due to interaction with surrounding gases.

SMOs as gas sensing material provides numerous advantages as compared to other nanomaterials such as low cost. The SMOs are classified into two groups, which are transition and non-transition metal oxides. The transition metals oxides contain multiple oxidation states, some examples are Fe_3O_4 and Cr_2O_3 [32]. The non-transition are metal contains one oxidation state, such as ZnO, SnO_2 and Al_2O_3. Transition metals oxides could form different oxidation states on the surface, which enables the SMOs to be a more suitable gas sensing material [32]. There are several factors that affect the sensitivity of the SMOs, such as the microstructure, porosity and dopants [11, 32]. The sensitivity of the sensor can be improved by manipulating the microstructure of the SMOs such as grain size. SMOs with relatively high surface area and porosity exhibit increased gas sensitivity [30]. Addition of dopants such as Au and Pd can also be used to improve the sensitivity of the SMOs nanomaterials for gas sensing [33]. Gases can be classified as either reducing or oxidising gases and SMOs can be classified as p-type and n-type. The n-type metal oxides have been reported to show an increase in resistance in the presence of an oxidising gas and a decrease in resistance in the presence of a reducing gas, however, the p-typed shows an increase in the electrical resistance when exposed to a reducing gas [26].

2.2.4.1 Zinc oxide (ZnO)

Amongst SMOs, ZnO possesses superior physical and chemical properties such as high photo stability, high electrocoupling effect, and high chemical stability [34-38]. Zinc oxide is a unique group II-VI SMO whose covalence is on the boundary between the covalent and ionic semiconductor metal oxide with a bandgap of approximately 3.4 eV [36-40]. ZnO has a wurtzite hexagonal structure with lattice parameters a=0.3296 nm and c=05265 nm [40-44]. The structure of ZnO can be described as several alternating planes composed of tetrahedrally coordinated O^{2-} and Zn^{2+} ions stacked together [44-45]. ZnO can be synthesised to different structures such as one-dimensional (1D), two-dimensional (2D) and three-dimensional (3D) nanostructures. 1D consists of structures such as nano-rods, nano-rings, nano-combs, nano-helixes, nano-wires, nano-combs, nano-belts, nano-combs and nano-needles. 2D consists of structures such as the nano-pallets and nanoplates. 3D structures of ZnO include snowflakes, coniferous urchin-like and flower-like. These different structures allow ZnO to be multifunctional [45-50].

ZnO is non-toxic and easy to synthesise in bulk. ZnO is an ideal chemi-resistive material for gas sensing because of properties such as photoelectric response. ZnO has also been reported to have excellent chemical and high thermal stability [48-52]. Other researchers have

established that the ZnO has a binding energy of 60 meV band. When the ZnO surface becomes exposed to oxygen in ambient conditions, the resistance of a gas sensor can relatively be increased by the formation of depletion layers due to the trapping of electrons in the conduction [50-54]. When a reducing gas interacts with the surface of the ZnO, the oxygen species interact with the gas molecules thereby releasing the fixed electrons back to the conduction band, making the resistance of the sensor to decrease. On the contrary, exposure to oxidising gases such as NO_2 which act as an electron acceptor has been reported to increase the sensor's resistance [54-56].

Another factor in gas sensing using ZnO material is the effect of temperature. The temperature affects the kinetics, electron mobility and conductivity of the reaction. A typical ZnO material operates at a temperature range of 300-500ºC. This is due to the high thermal energy needed to overcome the activation energy needed to excite the electrons mobility. The reaction kinetics are also increased which improve sensing measurement [56-60]. High operating temperatures is one of the drawbacks as it requires more energy to operate. High temperatures also cause instability in the material leading to unreliable results. Furthermore, a gas explosion can happen as a result of flammable gases with low ignition point in standard atmosphere [60-63].

The morphology of the nanostructured ZnO affects the operating temperature, response time, selectivity, sensitivity, recovery time and stability [64]. Different dimensions and structures are synthesised using optimised conditions on different methods. 1D ZnO structures possess high conductivity, and high electron mobility promoting an improved separation of electrons and holes thereby decreasing the electrical resistance of ZnO [46, 65-66]. The effective separation makes the absorbed oxygen species to be easily created; this is due to the reaction between the surface and absorbed oxygen molecules [65-69]. Different morphologies have been investigated by different researchers, Shingange *et al*. [70] synthesised rose-like ZnO nanostructures using a microwave hydrothermal method. The synthesised structures showed an improved response time and recovery time to NO_2 at 300ºC. Furthermore, the incorporation of Au into ZnO nanostructures significantly improved the sensing performance. Venkatesh *et al* [71] reported response time of 49 seconds and a recovery time of 19 seconds at 25 ppm NH_3 at 25^0 C [73-74]. This improved performance was attributed to defects site caused by the oxygen vacancies [71]. Motaung *et al* [74] synthesised ZnO nanostructures at different times of 12 h, 24 h and 72 h, the results showed improved sensitivity and selectivity on NO_2 gas at 24 h and 72 h, which proved a change in morphology at different synthesis times.

2.2.5 Carbon Nanotubes

There are different carbon-based materials such as graphite, fullerene, mesoporous carbon, carbon nanotubes (CNTs) and activated carbon. CNTs received a lot of attention in the past decade due to their unique properties such as electrical properties and higher surface area. CNTs consist of carbon atoms with a diameter measured in nanometers [7]. Since it was discovered by Iijima in 1991 [75], more studies have been initiated mainly due to their multiple applications. CNTs can either be metallic or semiconducting depending on the configuration. CNTs can also be used to increase the performance of gas sensors. The choice of CNTs in this study was based on their high electrical conductivity, high surface area and high insulation capabilities [5]. They can be multi-walled (MWCNTs) or single-walled (SWCNTs) depending on the number of rolled graphene sheets [76]. Single-walled CNTs consists of one layer of rolled graphene sheet with a diameter of 1 nanometer and tube length of thousands of times the diameter and it is depicted in Figure 2.1 (a) [77]. Multi-walled CNTs consist of several rolled layers of graphene sheets forming a tube shape as shown in Figure 2.1 (b) [77]. The chemical or physical properties of CNTs can be controlled by the synthesis method used to synthesize them. CNTs synthesis method includes arch discharge, chemical vapour deposition (CVD) and laser ablation [78-80].

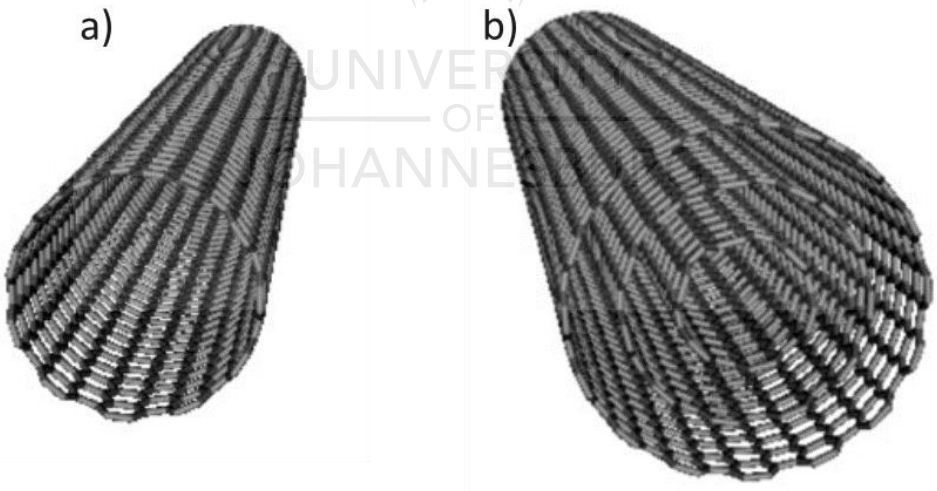

Figure 2.1: Depicts two different types of carbon nanotubes which are a) SWCNTs and b) MWCNTs [77]

2.2.5.1 Chemical Vapour Deposition (CVD)

CVD is the most studied and used method for the synthesis of CNTs. It is mostly used for mass production of different types of CNTs [78]. Currently, this method has been used to produce

controlled CNTs. CVD uses hydrocarbon gaseous carbon sources such as methane, toluene and acetylene. CVD uses transitional metal catalysts such as Ni, Co and ferrocene to promote the growth of CNTs [78-80]. CVD operates at a temperature range of 600^0 C - 1200^0 C [80]. Kumar et al [81], studied the synthesis of CNTs using CVD and concluded that there are two main things that affect the type of CNTs produced namely temperature and catalyst particle size. Lower temperature with smaller particles size catalyst mainly produces multi-walled CNTs. The disadvantages of this method are that it produces more amorphous carbon, as compared to other methods [82]. The amorphous carbons affect the electrical conductivity and the thermal characteristics of the CNTs [83]. An example of the CVD set up is depicted in Figure 2.2. [81]

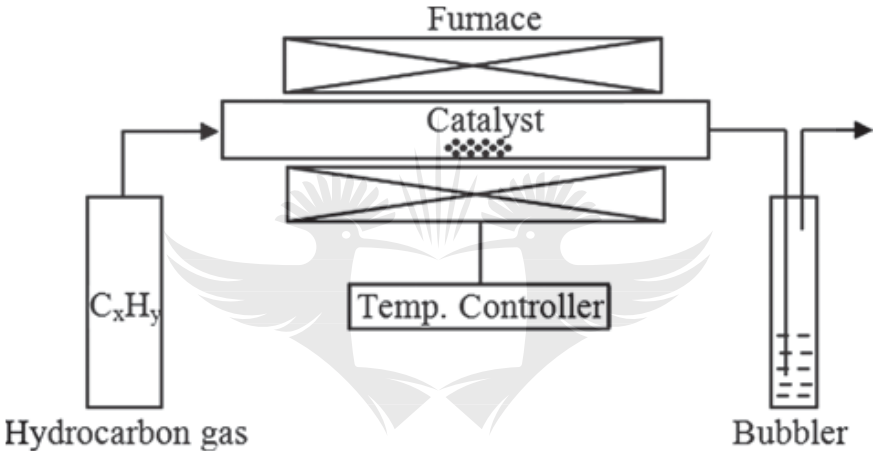

Figure 2.2: Schematic diagram of the CVD [81]

2.2.5.2 Arc Discharge

The arc discharge technique involves creating direct current (DC) between the graphite electrodes under inert conditions (e.g. argon) [84]. It was the first method to produce CNTs using two graphene electrodes. The technique produces MWCNTs without the use of a catalyst while the production of SWCNTs requires mixed metal catalyst such as Ni and Co [84-86]. The produced CNTs have a high degree of structural perfection and it is controlled by the temperature of the chamber and concentration of the catalyst [87]. Other electrodes and chemicals have been investigated also for the production of CNTs using arc discharge method [88]. A schematic diagram of the arc discharge is shown in Figure 2.3 [77]

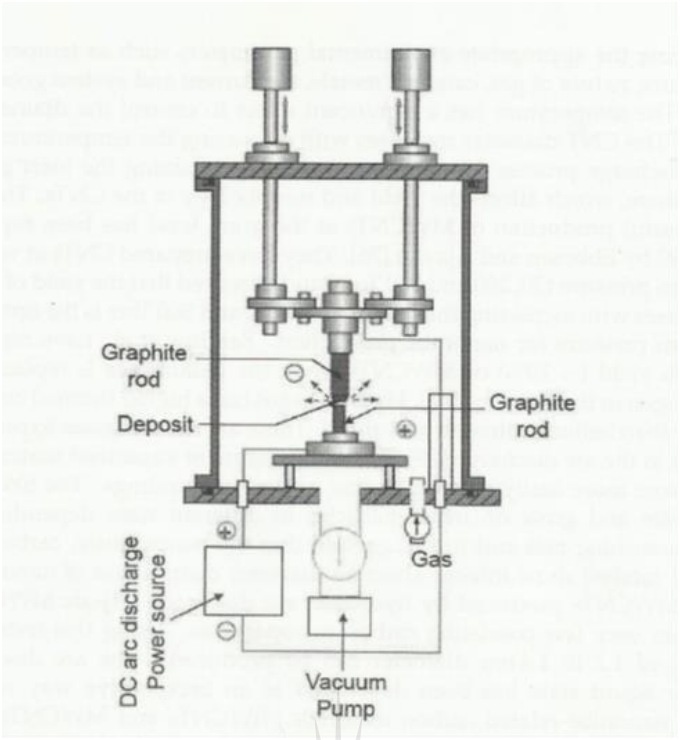

Figure 2.3: Schematic diagram of arc discharge [77]

2.2.5.3 Laser Ablation

The laser ablation technique involved the use of solid graphite mounted in the quartz boat that is placed inside the quartz tube at a high temperature of 600-1500^0 C [89]. The high temperatures vapourize the solid graphite by a laser beam pulse and the vapourized carbon-based soot is collected in the walls of the quartz tube [89-90]. The high synthesis temperature makes the produced CNTs to be structurally perfect, however, the use of high temperatures requires high power while producing small quantities which are the main disadvantages of using laser ablation [91-92]. The chemical composition of the precursor and the laser power are the main variables that affect the quantity and type of the CNTs [92]. The schematic diagram of the laser ablation technique for the synthesis of CNTs is shown in Figure 2.4 [77]

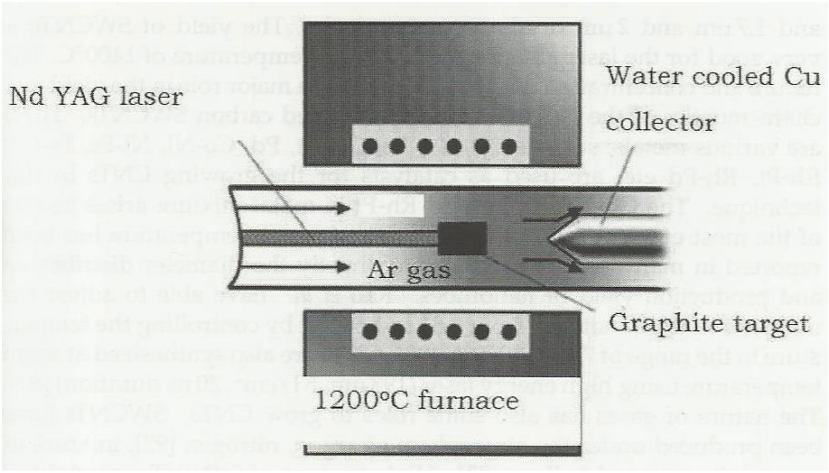

Figure 2.4: Schematic diagram of the laser ablation technique [77]

2.2.5.4 Growth Mechanisms of CNTs

Different researchers have investigated the growth mechanism of CNTs, however, the most popular growth mechanisms of CNTs from the CVD technique are the tip-growth model and base-growth model [81]. The reaction conditions and post reaction analysis determine the growth mechanism. However, a general CNTs growth mechanism is outlined as follows [93]. Hydrocarbon gas comes in contact with a hot metal catalyst, the hydrocarbon decomposes into hydrogen and carbon; Hydrogen gas goes out of the system and the carbon gets dissolved in the catalyst. Then after it reached the carbon solubility limit, the dissolved carbon precipitates out in the form of cylindrical sheets which are energetically stable [81, 77, 90].

The tip-growth model occurs when the carbon source gas is introduced on top of the metal catalyst [81], the carbon passes down through the metal catalyst and the CNTs grows from the bottom pushing the catalyst up from the substrate, as depicted in Figure 2.5 (a) [81], The CNTs continues to grow until the metal is completely covered with extra carbon and the CNTs growth stops.

The other mechanism is the base-growth model. The decomposition of hydrocarbons takes place same as the tip-growth model [81], however, the precipitation of CNTs fails to push the metal catalyst particle up, which in turn causes the CNTs to grow from the apex of the metal [94]. As depicted in Figure 2.5 (b) the carbon forms out as hemispherical which extends up. The hydrocarbons deposition happens on the lower sides of the metal catalyst surface, as the carbon diffuses upward resulting in the CNTs growing with the metal catalyst rooted in its base [81].

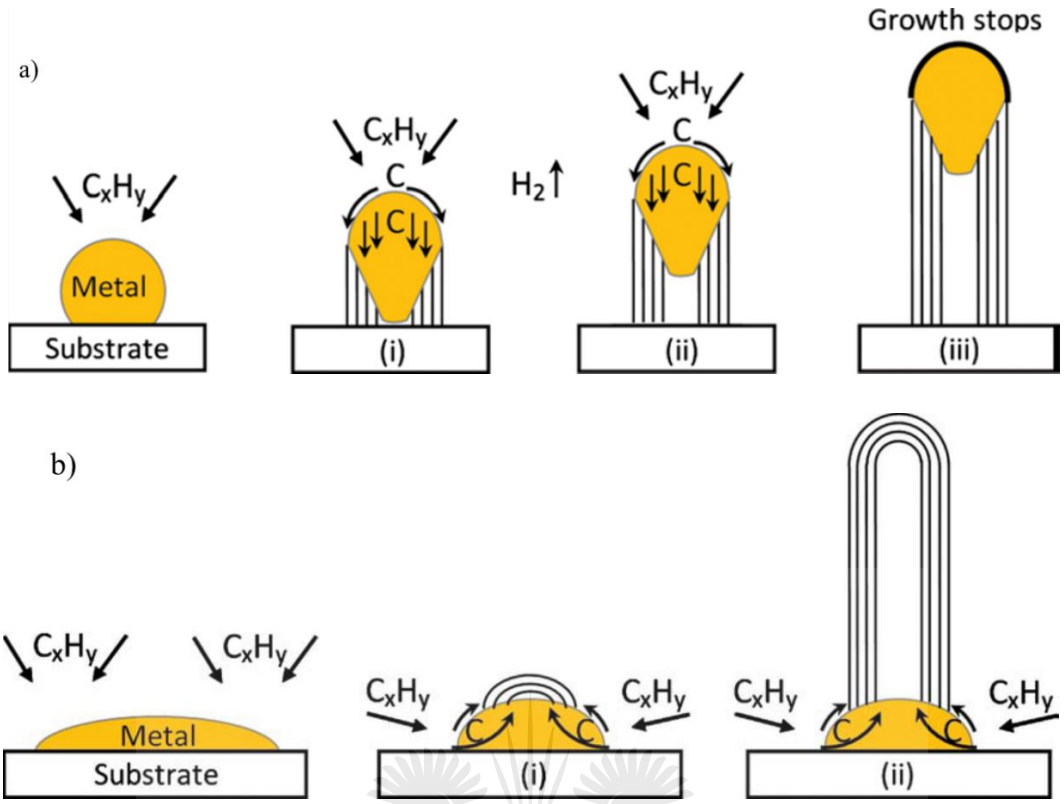

Figure 2.5: Growth mechanism of CNTs are depicted in a) tip-growth model and b) base-growth model [81]

2.2.5.5 Properties of CNTs (Electrical and Chemical Properties)

CNTs are applicable in different fields due to their unique properties. The main properties are electrical and chemical properties [80]. The electrical properties are one of the most researched properties offered by CNTs. The electrical properties can be explained in terms of the band structure of graphene [95]. The electrical properties can vary from metallic to semiconducting depending on the configuration (zigzag or chiral) [95]. As discussed earlier, CNTs are formed by rolled graphene sheets. As shown in Figure 2.6 (A), at k-points (fermi points) of the graphene sheets the conduction and valence bands are connecting resulting in a zero-bandgap, hence graphene is a zero-bandgap semiconductor [95-97]. However, as shown in Figure 2.6 (B), for carbon nanotubes each band formed from graphene known as the graphitic bands, opens up to form sub-bands, this is due to the accumulation of electrons in the radial direction [96]. When these graphitic sub-bands pass through the fermi points, the CNTs are metallic. However, if the sub-bands do not pass the fermi point as shown in Figure 2.6 (C), then the CNTs are semiconducting [98]. The direction of the rolled graphene sheets decides the formation of the CNT. The CNTs can either be armchair, zigzag or chiral [100]. Some of the CNTs form around the axis of symmetry, which results in chiral shaped CNTs. During the

synthesis of CNTs defects occurs on the produced CNTs. The presence of these structural defects such as vacancies, stone-wales and pentagon-heptagon pairs enhances the chemical reactivity of the CNTs [99-100]. The CNTs with defects absorbs gas molecules easily and can be functionalized easily [95]

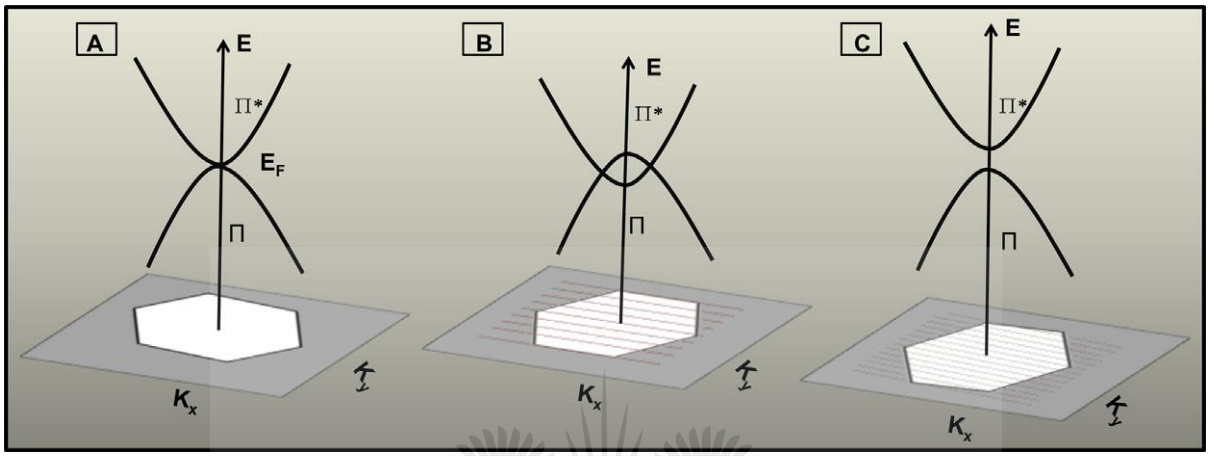

Figure 2.6: 3-D plots for the dispersion relations of a) graphene b) metallic CNTs and c) semiconducting CNTs [96]

2.2.5.6 Functionalization of CNTs

CNTs present good properties, however, functionalized CNTs exhibit properties which have potential in gas sensors due to functional groups which have been attached on the surface of the CNTs and are highly reactive and absorbs gas molecules [100]. There are different routes used to functionalize the CNTs such as physical functionalization via milling, ultra-sonication and friction, however, the most used route is the chemical route as it exploits the reactive properties of CNTs [101]. CNTs are hydrophobic in nature, this is due to van der Waal forces. During synthesis, there is amorphous carbon that is formed making CNTs insoluble in chemical solvents [103]. The functional groups determine the characteristics properties of CNTs and enhance the reactions between the CNTs and molecules [105]. The commonly used functional groups are carboxyl (-COOH), hydroxyl (-OH) and carbonyl (-C=O) [104-106]. Attaching these groups into the CNTs follows the covalent bond whereby acids are used. Nitric acid (HNO_3) and 5M diluted Sulfuric acid (H_2SO_4) with a ratio of 1:3 are usually used to functionalize the CNTs [100]. Functionalizing with acid allows for the conjugation of other materials in CNTs, makes the CNTs to be hydrophilic, improve homogeneous dispersion, remove impurities and introduces more binding sites for gas molecules [100, 106].

2.2.5.7 CNTs in Gas Sensing

CNTs have been applied in gas sensing using different methods. Avouris *et al* [99] synthesized electrodes by casting CNTs on interdigitated electrodes. The usually used CNTs are single-walled CNTs because they are semiconductors as compared to multi-walled CNTs which are mostly conducting [100]. The electrodes were synthesized using photolithography of Ti and Au in silicon oxide. The SWCNTs were prepared by dispersing in dimethylformamide and then deposited in the electrode. Another method used is dielectrophoresis (DEP) [103]. DEP method has been used to manipulate the CNTs in terms of orientation and separation. The DEP-synthesized CNTs sensors successfully detected gases such as SO_2 and NH_3 [104].

2.2.5.8 CNTs and Semiconductor metal oxides

Semiconductor Metal oxides incorporated with CNTs have been reported in the literature. There are two main methods used in making the composite, namely in-situ and ex-situ [107]. The in situ method involves synthesising CNTs within the same process with metal oxide. In this method, one of the constituents that make up the composite is synthesised in the presence of another or they can also be synthesised simultaneously in one process [107-108]. The main advantage of this method is that one constituent can become support material, same with the synthesis of CNTs and SMOs whereby the CNTs can act as a support and the SMO can settle on top [109]. The ex-situ method involves the decoration of CNTs by metal oxide after the synthesis of CNTs. In this method, the constituent that makes up the composites are synthesised separately with their desired shape and dimensions, and CNTs can also be functionalised [107, 109]. After they have been synthesised, they link together through van der Waals forces, covalent bonding, electrostatic forces, hydrogen bonds and hydrophobic interaction [110]. The main draw-back of this method is that the distribution of nanoparticles depends on the functional groups introduced in the CNTs. However, the advantage of this method is that it is easy to control the shapes and dimensions of individual constituents [107, 109].

Depending on which material is in larger quantity, the composites can be divided into two, there is CNTs decorated with SMO and SMO decorated with CNTs [107, 110]. MWCNTs are a stable p-type semiconductor making it appropriate for gas sensing applications [111]. The primary reason to decorate SMOs with CNTs is to enhance the gas sensing properties of SMOs hence it is important to choose a suitable SMO for making the composite [112-114]. Making a composite of MWCNTs with n-type SMO is more desirable [113]. This is because the formation of p-n type heterojunctions via surface decoration is an effective method to improve the gas sensing performance of SMOs [112]. For the p-type MWCNTs, the transfer of charge

carriers is through the low resistance hole accumulation layer, and through the formation of p-n heterojunctions the charge transfer path is stifled by the flow of electrons from the SMO to the MWCNTs resulting in the decrease in width of the charge carrier path [109, 114-115].

2.2.6 Gas Sensing Mechanism for SMOs

The fundamental mechanism of gas sensing has been reported in several published research [11, 23-28]. The atoms of the molecules interact with SMOs surfaces, subsequently changing the surface conductivity. The conductivity of ZnO can be altered by the presence of traces of reactive gases present in the air [28-30]. The interaction of gas molecules and the SMOs can either be physical (physisorption) or chemical (chemisorption). Chemisorption includes the reduction and oxidation of the metal oxide leading to a formation of new chemical bonds. Physisorption is due to weak Van der Waals forces between the SMOs and gas molecules [2].

The electrical conductivity variation of the sensor is caused by the trapping of electrons by absorbed molecules usually from environmental oxygen [26]. When the oxygen molecules are absorbed on to the metal oxide surface, they extract and trap the electron thereby leaving an electron depleted region (Figure 2.7) [26-30]. The reaction of the oxygen species with a reducing gas and the exchange of adsorbed oxygen species with other molecules decreases band bending thereby increasing the conductivity [11, 26]. The oxygen species is more present at the temperatures of 300-450ºC, which is the operating temperature of most SMOs for gas sensing.

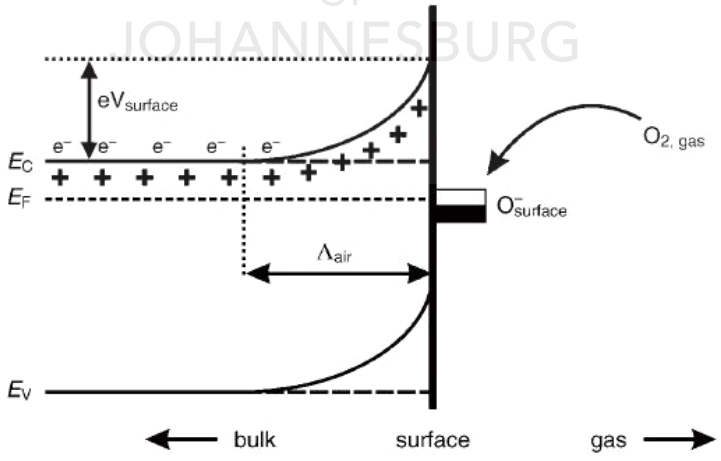

Figure 2.7: Depicts a chemisorption of charged species, where E_c is energy of the conduction band, E_v is valence band, E_f is the fermi level, Λair is the width of the space charge layer, eV surface is the potential barrier and e-,+ represent conducting electrons on the donor sites [26].

2.2.7 Factors Affecting the Sensitivity of SMOs

There are several methods that are used to improve the sensitivity of SMOs. Methods such as (ⅰ) surface modification, (ⅱ) microstructure (grain size and shape) and (ⅲ) porosity have been used to modify the SMOs to improve sensitivity. The sensing mechanism relies more on surface reactions, hence the importance of improving the surface structure of nanomaterials [76].

2.2.7.1 Surface Modification

Almost all metal oxides have a problem of low sensitivity and high operating temperature. Attempts have been made to modify the surface of the SMOs by doping them with metals [116-117]. The addition or doping with these metals has been previously reported to increase the response time and reducing the operating temperature [118]. Surface modification by noble metals such as Au and Pt increases the electrical variation of the SMOs hence improving gas sensing properties such as response time and sensitivity [117-119]. Table 2.1 shows various chemi-resistive materials with their recommended noble metal additives.

Table 2.1: Some semiconductor metal oxides with recommended additives

Chemiresistive material	Base Material	Additives	Analysing gas	Reference
Metal oxides	SnO_2	Platinum (Pt), Silver (Ag), Palladium (Pd), Gold (Au), Iron (Fe), Indium (In).	Carbon monoxide (CO), Methane (CH_4), Ammonia (NH_3), Nitrous Oxide (N_2O), Hydrogen sulphide (H_2S), Sulphur dioxide (SO_2)	118, 126-129
	TiO_2	Lanthanium (La), Platinum (Pt)	Ammonia (NH_3), hydrogen (H_2), Oxygen (O)	127-129
	WO_3	Palladium (Pd), Gold (Au), Zinc (Zn)	Hydrogen sulphide(H_2S), Ammonia (NH_3), Nitrogen dioxide (NO_2)	129-131
	Fe_2O_3	Gold (Au), Zinc (Zn), Platinum (Pt)	Carbon monoxide (CO), Propane, Toluene	131
	In_2O_3	Gold (Au), Aluminium (Al)	Sulphur dioxide (SO_2), Hydrogen sulphide(H_2S),	128-139

			Carbon dioxide (CO_2), Acetone	
	ZnO	Aluminium (Al), Tin (Sn), Copper (Cu), Palladium (Pd), Gold (Au)	Ammonia (NH_3), hydrogen (H2), Carbon monoxide (CO), Hydrogen sulphide(H_2S), Nitrogen dioxide (NO_2), Methanol, LPG, Methane	131-136

Shingange *et al* [121] synthesised rose like hierarchical Au/ZnO nanostructures using a microwave hydrothermal method. The synthesised composite structures showed an enhanced response time and faster recovery time to NO_2 gas at 300ºC as compared to the undoped ZnO. Katoch *et al* [122] investigated the effect of Au addition on the ZnO, they observed that the response time of the sensor to CO had improved when compared to the undoped ZnO. The size and dispersion of the noble metal nanoparticles have an effect on gas sensing performance.

SMOs can be mixed with other metal oxides (SnO_2-ZnO, Fe_2O_3-ZnO, ZnO-CuO) to make composites in an attempt to improve gas sensing performance [123-125]. Zhu *et al* [27] investigated the effect of the metal oxides composites SnO_2-ZnO on gas sensitivity. The composite showed an improved sensitivity on certain gases as compared to the individual metal oxides such as ZnO, which suggest a synergistic effect between the two components.

2.2.7.2 Microstructures

The sensitivity of the gas sensor can be improved by significantly changing the microstructures like grain size. There have been attempts to synthesize materials with small sizes because small grain sizes result in a larger surface area [120]. A more exposed surface area will increase the interaction between the gas molecules and material surface hence improving the sensitivity of the material. Different models have been developed to describe the effect of grain size. Xu *et al*, [128] developed a model that explains the sensing ability of the SnO_2 by comparing the grain size (D) and the thickness of the space charge layer (2L). The model suggests that when D>>2L the conductance is limited by boundary control also known as Schottky barrier [62]. This suggests that the structure is not sensitive to the charges acquired from the surface but the inner charges [141-142]. If D=2L then the conductance is limited by necks between grains, this is because the number of necks is bigger than the grain contacts and it defines the size

dependence of gas sensitivity [46, 61], if the D<2L then it suggests that the conductance is influenced by every grain. This concept is depicted in Figure 2.8.

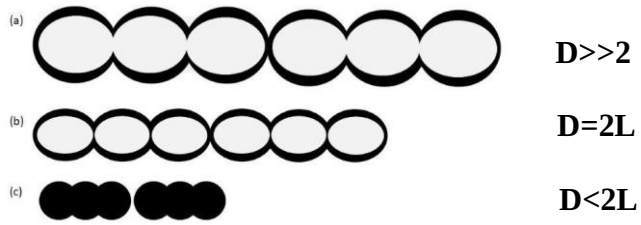

Figure 2.8: Three mechanism (a, b, c) of grain size dependence of conductance gas sensing materials

2.2.7.3 Humidity and Temperature

The humidity of the surrounding environment can affect the performance of a gas sensor. The water molecules that get absorbed in the sensor material do not donate any electrons. The most used humidity sensors are ionic-type sensors. The mechanism of humidity sensors depends on H^+ or H_3O^+ from the dissociation of adsorption water [142]. The reaction between the water molecules from the humidity and the oxygen surface causes a decrease in resistance of the gas sensor, resulting in a decrease in sensitivity [143-144]. The adsorption of water molecules hinders the chemisorption of oxygen species on the surface of the metal oxide due to the decrease in surface area, this affects the response time of the sensor. The effect of humidity on the SnO_2 gas sensor for C_2H_2 gas [103-105], showed that the water molecules acted as a barrier for the adsorption of the C_2H_2 gas which decreased the sensitivity [146].

In summary, SMOs have been used for gas sensing applications. However, they had high response times for different gases such as CO and H_2S. Different modifications have been performed in an attempted to improve the gas sensing performance of the SMOs such as making the composites of the SMOs with other materials. Different studies have been reported on composite of SMOs with heavy metals such as palladium, gold and silver. However, the response time has not been significantly improved. There is a gap in the research of carbon materials such as carbon nanotubes composite with SMOs. The carbon nanotubes have been reported to have a high surface area and highly conductive, which has the potential to increase the electrical conductivity of the SMOs and subsequently improving the sensing parameters.

2.3 Reference

[1] Dey, A. (2018). Semiconductor metal oxide gas sensors: A Review. Materials Science and Engineering: B, 229, pp.206-217.

[2] Zhu, L. and Zeng, W. (2017). Room-temperature gas sensing of ZnO-based gas sensor: A review. Sensors and Actuators A: Physical, 267, pp.242-261.

[3] Jiménez-Cadena, G., Riu, J. and Rius, F. (2007). Gas sensors based on nanostructured materials. The Analyst, 132(11), pp.1083-1084.

[4] Wang, Y. and Yeow, J. (2009). A Review of Carbon Nanotubes-Based Gas Sensors. Journal of Sensors, 40, pp.1-24.

[5] Brsan, N. and Weimar, U. (2003). Understanding the fundamental principles of metal oxide-based gas sensors; the example of CO sensing with SnO_2 sensors in the presence of humidity. Journal of Physics: Condensed Matter, 15(20), pp. 813-839.

[6] Comini, E., Baratto, C., Faglia, G., Ferroni, M., Vomiero, A. and Sberveglieri, G. (2009). Quasi-one-dimensional metal oxide semiconductors: Preparation, characterization and application as chemical sensors. Progress in Materials Science, 54(1), pp.1-67.

[7] Li, T., Zeng, W. and Wang, Z. (2015). Quasi-one-dimensional metal-oxide-based heterostructural gas-sensing materials: A review. Sensors and Actuators B: Chemical, 221, pp.1570-1585.

[8] Zappa, D., Bertuna, A., Comini, E., Kaur, N., Poli, N., Sberveglieri, V. and Sberveglieri, G. (2017). Metal oxide nanostructures: preparation, characterization and functional applications as chemical sensors. Beilstein Journal of Nanotechnology, 8, pp.1205-1217.

[9] Mirzaei, A. and Neri, G. (2016). Microwave-assisted synthesis of metal oxide nanostructures for gas sensing application: A review. Sensors and Actuators B: Chemical, 237, pp.749-775.

[10] Huang, J. and Wan, Q. (2009). Gas sensors based on semiconducting metal oxide one-dimensional nanostructures. Sensors, 9(12), pp.9903-9924.

[11] Wang, C., Yin, L., Zhang, L., Xiang, D. and Gao, R. (2010). Metal oxide gas sensors: sensitivity and influencing factors. Sensors, 10(3), pp.2088-2106.

[12] Varpula, A., Novikov, S., Sinkkonen, J. and Utriainen, M. (2008). Bias dependent sensitivity in metal-oxide gas sensors. Sensors and Actuators B: Chemical, 131(1), pp.134-142.

[13] Liu, X., Cheng, S., Liu, H., Hu, S., Zhang, D. and Ning, H. (2012). A survey on gas sensing technology. Sensors, 12(7), pp.9635-9665.

[14] Bhuvaneshwari, S. and Gopalakrishnan, N. (2016). Facile synthesis of low dimensional CuO nanostructures and their gas sensing applications. Crystal Research and Technology, 51(2), pp.145-153.

[15] Perret, B. Gründler P. (2008). Chemical sensors. An introduction for scientists and engineers. Analytical and Bioanalytical Chemistry, 392(2), pp.21-22.

[16] Barsan, N., Koziej, D. and Weimar, U. (2007). Metal oxide-based gas sensor. Sensors and Actuators B: Chemical, 121(1), pp.18-35.

[17] Govardhan, K. and Grace, A. (2016). Metal/metal mxide doped semiconductor based metal oxide gas sensors—A Review. Sensor Letters, 14(8), pp.741-750.

[18] Ayesh, A. (2016). Metal/metal-oxide nanoclusters for gas sensor applications. Journal of Nanomaterials, 25, pp.1-17.

[19] Buono, C., Mirabella, D. and Aldao, C. (2017). Sensitivity of metal oxide gas sensors to non-parabolic intergranular barriers. Sensors and Actuators B: Chemical, 246, pp.1025-1029.

[20] Liu, J., Wang, W., Li, S., Liu, M. and He, S. (2011). Advances in SAW gas sensors based on the condensate-adsorption effect. Sensors, 11(12), pp.11871-11884.

[21] Liu, J. and Lu, Y. (2014). Response mechanism for surface acoustic wave gas sensors based on surface-adsorption. Sensors, 14(4), pp.6844-6853.

[22] Feng, P., Shao, F., Shi, Y. and Wan, Q. (2014). Gas sensors based on semiconducting nanowire field-effect transistors. Sensors, 14(9), pp.17406-17429.

[23] Li, J., Lu, Y., Ye, Q., Cinke, M., Han, J. and Meyyappan, M. (2003). Carbon nanotube sensors for gas and organic vapour detection. Nano Letters, 3(7), pp.929-933.

[24] Barsan, N., Schweizer-Berberich, M. and Göpel†, W. (1999). Fundamental and practical aspects in the design of nanoscaled SnO_2 gas sensors: a status report. Fresenius' Journal of Analytical Chemistry, 365(4), pp.287-304.

[25] Sharma, A., Tomar, M. and Gupta, V. (2013). Enhanced response characteristics of SnO2 thin film based NO_2 gas sensor integrated with nanoscaled metal oxide clusters. Sensors and Actuators B: Chemical, 181, pp.735-742.

[26] Franke, M., Koplin, T. and Simon, U. (2006). Metal and metal oxide nanoparticles in chemiresistors: does the nanoscale matter. Small, 2(3), pp.301-301.

[27] Zhu, C., Chen, Y., Wang, R., Wang, L., Cao, M. and Shi, X. (2009). Synthesis and enhanced ethanol sensing properties of α-Fe_2O_3/ZnO heteronanostructures. Sensors and Actuators B: Chemical, 140(1), pp.185-189.

[28] Hu, Y., Zhou, X., Han, Q., Cao, Q. and Huang, Y. (2003). Sensing properties of CuO–ZnO heterojunction gas sensors. Materials Science and Engineering: B, 99(1), pp.41-43.

[29] Ling, Z. and Leach, C. (2004). The effect of relative humidity on the NO_2 sensitivity of a SnO_2/WO_3 heterojunction gas sensor. Sensors and Actuators B: Chemical, 102(1), pp.102-106.

[30] Van Duy, N., Van Hieu, N., Huy, P., Chien, N., Thamilselvan, M. and Yi, J. (2008). Mixed SnO_2/TiO_2 included with carbon nanotubes for gas-sensing application. Physica E: Low-dimensional Systems and Nanostructures, 41(2), pp.258-263.

[31] Gupta, B., Shrivastav, A. and Usha, S. (2016). Surface plasmon resonance-based fiber optic sensors utilizing molecular imprinting. Sensors, 16(9), p.1381.

[32] Zhou, X., Cheng, X., Zhu, Y., Elzatahry, A., Alghamdi, A., Deng, Y. and Zhao, D. (2018). Ordered porous metal oxide semiconductors for gas sensing. Chinese Chemical Letters, 29(3), pp.405-416.

[33] Madhusoodanan, K., Vimalkumar, T. and Vijayakumar, K. (2018). Gas sensing application of nanocrystalline zinc oxide thin films prepared by spray pyrolysis. Bulletin of Material Science, 38 (3), pp.583-591.

[34] Pan, Z.W., Dai, Z.R. and Wang, Z.L. (2001). Nanobelts of semiconducting oxides. Science, 291(5510), pp.1947-1949.

[35] Wang, Z. (2003). Nanobelts, nanowires, and nanodiskettes of semiconducting oxides—from materials to nanodevices. Advanced Materials, 15(5), pp.432-436.

[36] Sadek, A., Choopun, S., Wlodarski, W., Ippolito, S. and Kalantar-zadeh, K. (2007). Characterization of ZnO nanobelt-based gas sensor and hydrocarbon sensing. IEEE Sensors Journal, 7(6), pp.919-924.

[37] Gao, P.X., Ding, Y., Mai, W., Hughes, W.L., Lao, C. and Wang, Z.L. (2005). Conversion of zinc oxide nanobelts into superlattice-structured nanohelices. Science, 309(5741), pp.1700-1704.

[38] Kong, X.Y., Ding, Y., Yang, R. and Wang, Z.L. (2004). Single-crystal nanorings formed by epitaxial self-coiling of polar nanobelts. Science, 303(5662), pp.1348-1351.

[39] Deng, J., Wang, Q., Zhou, Y., Zhao, B. and Zhang, R. (2017). Facile design of a ZnO nanorod–Ni core–shell composite with dual peaks to tune its microwave absorption properties. RSC Advances, 7(15), pp.9294-9302.

[40] Cui, J., Jiang, J., Shi, L., Zhao, F., Wang, D., Lin, Y. and Xie, T. (2016). The role of Ni doping on photoelectric gas-sensing properties of ZnO nanofibers to HCHO at room-temperature. RSC Advances, 6(82), pp.78257-78263.

[41] Jing, Z. and Zhan, J. (2008). Fabrication and gas-sensing properties of porous ZnO nanoplates. Advanced Materials, 20(23), pp.4547-4551.

[42] Liu, C., Zhao, L., Wang, B., Sun, P., Wang, Q., Gao, Y., Liang, X., Zhang, T. and Lu, G. (2017). Acetone gas sensor based on NiO/ZnO hollow spheres: Fast response and recovery, and low (ppb) detection limit. Journal of Colloid and Interface Science, 495, pp.207-215.

[43] Sonker, R., Sabhajeet, S., Singh, S. and Yadav, B. (2015). Synthesis of ZnO nanopetals and its application as NO2 gas sensor. Materials Letters, 152, pp.189-191.

[44] Yu, L., Guo, F., Liu, S., Yang, B., Jiang, Y., Qi, L. and Fan, X. (2016). Both oxygen vacancies defects and porosity facilitated NO_2 gas sensing response in 2D ZnO nanowalls at room temperature. Journal of Alloys and Compounds, 682, pp.352-356.

[45] Cai, Y. and Fan, H. (2013). One-step self-assembly economical synthesis of hierarchical ZnO nanocrystals and their gas-sensing properties. CrystEngComm, 15(44), pp.9148-9149.

[46] Zhang, H., Wu, R., Chen, Z., Liu, G., Zhang, Z. and Jiao, Z. (2012). Self-assembly fabrication of 3D flower-like ZnO hierarchical nanostructures and their gas sensing properties. CrystEngComm, 14(5), pp.1775-1776.

[47] Guo, J., Zhang, J., Zhu, M., Ju, D., Xu, H. and Cao, B. (2014). High-performance gas sensor based on ZnO nanowires functionalized by Au nanoparticles. Sensors and Actuators B: Chemical, 199, pp.339-345.

[48] Hongsith, N., Viriyaworasakul, C., Mangkorntong, P., Mangkorntong, N. and Choopun, S. (2008). Ethanol sensor based on ZnO and Au-doped ZnO nanowires. Ceramics International, 34(4), pp.823-826.

[49] Patil, P., Gaikwad, G., Patil, D. and Naik, J. (2016). Synthesis of 1-D ZnO nanorods and polypyrrole/1-D ZnO nanocomposites for photocatalysis and gas sensor applications. Bulletin of Materials Science, 39(3), pp.655-665.

[50] Xu, J., Shun, Y., Pan, Q. and Qin, J. (2000). Sensing characteristics of double layer film of ZnO. Sensors and Actuators B: Chemical, 66(1-3), pp.161-163.

[51] Geng, X., Zhang, C. and Debliquy, M. (2016). Cadmium sulfide activated zinc oxide coatings deposited by liquid plasma spray for room temperature nitrogen dioxide detection under visible light illumination. Ceramics International, 42(4), pp.4845-4852.

[52] Zhu, L. and Zeng, W. (2017). A novel coral rock-like ZnO and its gas sensing. Materials Letters, 209, pp.244-246.

[53] Zhu, L., Li, Y. and Zeng, W. (2018). Hydrothermal synthesis of hierarchical flower-like ZnO nanostructure and its enhanced ethanol gas-sensing properties. Applied Surface Science, 427, pp.281-287.

[54] Liu, X., Sun, J. and Zhang, X. (2015). Novel 3D graphene aerogel–ZnO composites as efficient detection for NO_2 at room temperature. Sensors and Actuators B: Chemical, 211, pp.220-226.

[55] Chang, J., Kuo, H., Leu, I. and Hon, M. (2002). The effects of thickness and operation temperature on ZnO:Al thin film CO gas sensor. Sensors and Actuators B: Chemical, 84(3), pp.258-264.

[56] Hosseini, Z., zad, A. and Mortezaali, A. (2015). Room temperature H_2S gas sensor based on rather aligned ZnO nanorods with flower-like structures. Sensors and Actuators B: Chemical, 207, pp.865-871.

[57] Korotcenkov, G. and Cho, B. (2012). The role of grain size on the thermal instability of nanostructured metal oxides used in gas sensor applications and approaches for grain-size stabilization. Progress in Crystal Growth and Characterization of Materials, 58(4), pp.167-208.

[58] Korotcenkov, G., Cho, B., Gulina, L. and Tolstoy, V. (2009). SnO_2 thin films modified by the SnO_2–Au nanocomposites: Response to reducing gases. Sensors and Actuators B: Chemical, 141(2), pp.610-616.

[59] Korotcenkov, G. (2007). Metal oxides for solid-state gas sensors: What determines our choice?. Materials Science and Engineering: B, 139(1), pp.1-23.

[60] Korotcenkov, G., Brinzari, V., Pronin, I., Ham, M. and Cho, B. (2017). Metal oxides for application in conductometric gas sensors: how to choose. Solid State Phenomena, 266, pp.187-195.

[61] Xu, H., Liu, X., Cui, D., Li, M. and Jiang, M. (2006). A novel method for improving the performance of ZnO gas sensors. Sensors and Actuators B: Chemical, 114(1), pp.301-307.

[62] Sun, P., Zhu, Z., Zhao, P., Liang, X., Sun, Y., Liu, F. and Lu, G. (2012). Gas sensing with hollow α-Fe_2O_3 urchin-like spheres prepared via template-free hydrothermal synthesis. CrystEngComm, 14(24), pp.8335-8336.

[63] Kim, H., Choi, K., Lee, J. and Akbar, S. (2009). Highly sensitive and ultra-fast responding gas sensors using self-assembled hierarchical SnO_2 spheres. Sensors and Actuators B: Chemical, 136(1), pp.138-143.

[64] Caihong, W., Chu, X. and Wu, M. (2007). Highly sensitive gas sensors based on hollow SnO_2 spheres prepared by carbon sphere template method. Sensors and Actuators B: Chemical, 120(2), pp.508-513.

[65] Moon, C., Kim, H., Auchterlonie, G., Drennan, J. and Lee, J. (2008). Highly sensitive and fast responding CO sensor using SnO_2 nanosheets. Sensors and Actuators B: Chemical, 131(2), pp.556-564.

[66] Xue, N., Zhang, Q., Zhang, S., Zong, P. and Yang, F. (2017). Highly sensitive and selective hydrogen gas sensor using the mesoporous SnO_2 modified layers. Sensors, 17(10), pp.2351-2352.

[67] You, L., Sun, Y., Ma, J., Guan, Y., Sun, J., Du, Y. and Lu, G. (2011). Highly sensitive NO_2 sensor based on square-like tungsten oxide prepared with hydrothermal treatment. Sensors and Actuators B: Chemical, 157(2), pp.401-407.

[68] Chandra, L., Dwivedi, R. and Mishra, V. (2017). Highly sensitive NO_2 sensor using brush-coated ZnO nanoparticles. Materials Research Express, 4(10), pp.105-106.

[69] Cantalini, C., Sun, H., Faccio, M., Pelino, M., Santucci, S., Lozzi, L. and Passacantando, M. (1996). NO_2 sensitivity of WO_3 thin film obtained by high vacuum thermal evapouration. Sensors and Actuators B: Chemical, 31(2), pp.81-87.

[70] Shingange, K., Swart, H. and Mhlongo, G. (2018). Au functionalized ZnO rose-like hierarchical structures and their enhanced NO_2 sensing performance. Physica B: Condensed Matter, 535, pp.216-220.

[71] Sundara Venkatesh, P., Dharmaraj, P., Purushothaman, V., Ramakrishnan, V. and Jeganathan, K. (2015). Point defects assisted NH_3 gas sensing properties in ZnO nanostructures. Sensors and Actuators B: Chemical, 212, pp.10-17.

[72] Mirzaei, A., Kim, S. and Kim, H. (2018). Resistance-based H_2S gas sensors using metal oxide nanostructures: A review of recent advances. Journal of Hazardous Materials, 357, pp.314-331.

[73] Neri, G. (2011). Metal oxide nanostructures for solid state gas sensors: A recent patent survey. Recent Patents on Materials Sciences, 4(2), pp.146-158.

[74] Motaung, D., Mhlongo, G., Bolokang, A., Dhonge, B., Swart, H. and Sinha Ray, S. (2016). Improved sensitivity and selectivity of pristine zinc oxide nanostructures to H_2S gas: Detailed study on the synthesis reaction time. Applied Surface Science, 386, pp.210-223.

[75] Iijima, S. (1991). Helical microtubules of graphitic carbon. Nature, 354(6348), p.56.

[76] Manzano-Ramirez, A., Moreno-Barcenas, A., Apatiga-Castro, M., Rivera-Munoz, E., Nava-Mendoza, R. and Velazquez-Castillo, R. (2013). An Overview of Carbon Nanotubes: Synthesis, Purification and Characterization. Current Organic Chemistry, 17(17), pp.1858-1866.

[77] Purohit, R., Purohit, K., Rana, S., Rana, R.S. and Patel, V. (2014). Carbon nanotubes and their growth methods. Procedia Materials Science, 6, pp.716-728.

[78] Ebbesen, T. and Ajayan, P. (1992). Large-scale synthesis of carbon nanotubes. Nature, 358(6383), pp.220-222.

[79] de Oliveira, H. (2014). Synthesis and Dielectric Characterization of Multi-walled Carbon Nanotubes/Polypyrrole/Titanium Dioxide Composites. Fullerenes, Nanotubes and Carbon Nanostructures, 23(4), pp.339-345.

[80] Herrera-Ramirez, J.M., Perez-Bustamante, R. and Aguilar-Elguezabal, A. (2019). An Overview of the Synthesis, Characterization, and Applications of Carbon Nanotubes. In Carbon-Based Nanofillers and Their Rubber Nanocomposites pp. 47-75.

[81] Kumar, M. and Ando, Y. (2010). Chemical vapour deposition of carbon nanotubes: a review on growth mechanism and mass production. Journal of nanoscience and nanotechnology, 10(6), pp.3739-3758.

[82] Wei, B.Q., Vajtai, R., Jung, Y., Ward, J., Zhang, R., Ramanath, G. and Ajayan, P.M. (2002). Microfabrication technology: Organized assembly of carbon nanotubes. Nature, 416(6880), pp.495-495.

[83] Jung, D., Kim, J. and Lee, G.S. (2015). Enhanced humidity-sensing response of metal oxide coated carbon nanotube. Sensors and Actuators A: Physical, 223, pp.11-17.

[84] Arora, N. and Sharma, N.N. (2014). Arc discharge synthesis of carbon nanotubes: Comprehensive review. Diamond and Related Materials, 50, pp.135-150.

[85] Kaur, J., Gill, G.S. and Jeet, K. (2019). Applications of Carbon Nanotubes in Drug Delivery: A Comprehensive Review. In Characterization and Biology of Nanomaterials for Drug Delivery (pp. 113-135).

[86] Chimowa, G., Tshabalala, Z.P., Akande, A.A., Bepete, G., Mwakikunga, B., Ray, S.S. and Benecha, E.M. (2017). Improving methane gas sensing properties of multi-walled carbon nanotubes by vanadium oxide filling. Sensors and Actuators B: Chemical, 247, pp.11-18.

[87] Gang, X., Shenli, J., Jian, X. and Zongqian, S. (2007). Analysis of the carbon nano-structures formation in liquid arcing. Plasma Science and Technology, 9(6), p.770-771.

[88] Ando, Y., Zhao, X., Sugai, T. and Kumar, M. (2004). Growing carbon nanotubes. Materials today, 7(10), pp.22-29.

[89] Guo, T., Nikolaev, P., Thess, A., Colbert, D.T. and Smalley, R.E. (1995). Catalytic growth of single-walled manotubes by laser vapourization. Chemical physics letters, 243(1-2), pp.49-54.

[90] Koziol, K., Boskovic, B.O. and Yahya, N. (2010). Synthesis of carbon nanostructures by CVD method. In Carbon and Oxide Nanostructures 211 (2), pp. 23-49.

[91] Braidy, N., El Khakani, M.A. and Botton, G.A. (2002). Single-wall carbon nanotubes synthesis by means of UV laser vapourization. Chemical physics letters, 354(1-2), pp.88-92.

[91] Braidy, N., El Khakani, M.A. and Botton, G.A. (2001). Single-Wall Carbon Nanotubes Synthesis by Means of UV Laser Vapourization: Effects of the Furnace Temperature and the Laser Intensity Processing Parameters. MRS Online Proceedings Library Archive, pp. 703-705.

[92] Kumar, H. and Rani, R. (2013). Structural and optical characterization of ZnO nanoparticles synthesized by micro-emulsion route. International Letters of Chemistry, Physics and Astronomy, 14, pp.26-36.

[93] Gavillet, J., Loiseau, A., Journet, C., Willaime, F., Ducastelle, F. and Charlier, J.C. (2001). Root-growth mechanism for single-wall carbon nanotubes. Physical review letters, 87(27), pp.275504-275505.

[94] Huang, S., Woodson, M., Smalley, R. and Liu, J. (2004). Growth mechanism of oriented long single-walled carbon nanotubes using "fast-heating" chemical vapour deposition process. Nano Letters, 4(6), pp.1025-1028.

[95] Mittal, M. and Kumar, A. (2014). Carbon nanotube (CNT) gas sensors for emissions from fossil fuel burning. Sensors and Actuators B: Chemical, 203, pp.349-362.

[96] Avouris, P. (2002). Molecular electronics with carbon nanotubes. Accounts of chemical research, 35(12), pp.1026-1034.

[97] Zhong Xiyi, R. Saito, G. Dresselhaus and Dresselhaus, MS. (1999). Physical Properties of Carbon Nanotubes, Japanese Physical Society, 54(10), pp.832-833.

[98] Baxendale, M. (2003). The physics and applications of carbon nanotubes. Journal of Materials Science: Materials in Electronics, 14(10-12), pp.657-659.

[99] Avouris, P., Chen, Z. and Perebeinos, V. (2010). Carbon-based electronics. In Nanoscience and Technology: A Collection of Reviews from Nature Journals (pp. 174-184).

[100] Poncharal, P., Berger, C., Yi, Y., Wang, Z.L. and de Heer, W.A. (2002). Room temperature ballistic conduction in carbon nanotubes. 106(125) pp. 12104-12104

[101] Chiang, Y.C., Lin, W.H. and Chang, Y.C. (2011). The influence of treatment duration on multi-walled carbon nanotubes functionalized by H_2SO_4/HNO_3 oxidation. Applied Surface Science, 257(6), pp.2401-2410.

[102] Grüneis, A., Rümmeli, M.H., Kramberger, C., Grimm, D., Gemming, T., Barreiro, A., Ayala, P., Pichler, T., Kuzmany, H., Schamann, C. and Pfeiffer, R. (2006). Growth of carbon nanotubes from wet chemistry and thin film multilayer catalysts. physical state of the solid, 243(13), pp.3054-3057.

[103] Georgakilas, V., Kordatos, K., Prato, M., Guldi, D.M., Holzinger, M. and Hirsch, A. (2002). Organic functionalization of carbon nanotubes. Journal of the American Chemical Society, 124(5), pp.760-761.

[104] Chen, R.J., Bangsaruntip, S., Drouvalakis, K.A., Kam, N.W.S., Shim, M., Li, Y., Kim, W., Utz, P.J. and Dai, H. (2003). Noncovalent functionalization of carbon nanotubes for highly specific electronic biosensors. Proceedings of the National Academy of Sciences, 100(9), pp.4984-4989.

[105] Hirsch, A. (2002). Functionalization of single- walled carbon nanotubes. Angewandte Chemie International Edition, 41(11), pp.1853-18

[106] Balasubramanian, K. and Burghard, M. (2005). Chemically functionalized carbon nanotubes. Small, 1(2), pp.180-192.

[107] Mallakpour, S. and Khadem, E. (2016). Carbon nanotube–metal oxide nanocomposites: Fabrication, properties and applications. Chemical Engineering Journal, 302, pp.344-367.

[108] Lu, K. (2007). Rheological behavior of carbon nanotube-alumina nanoparticle dispersion systems. Powder Technology, 177(3), pp.154-161.

[109] Kwon, Y.J., Mirzaei, A., Kang, S.Y., Choi, M.S., Bang, J.H., Kim, S.S. and Kim, H.W. (2017). Synthesis, characterization and gas sensing properties of ZnO-decorated MWCNTs. Applied Surface Science, 413, pp.242-252.

[110] Hu, Y. and Guo, C. (2011). Carbon nanotubes and carbon nanotubes/metal oxide heterostructures: synthesis, characterization and electrochemical property. In Carbon Nanotubes-Growth and Applications. InTech.

[111] Yi, J., Xue, W.J., Xie, Z.P., Chen, J. and Zhu, L. (2015). A novel processing route to develop alumina matrix nanocomposites reinforced with multi-walled carbon nanotubes. Materials Research Bulletin, 64, pp.323-326.

[112] Hanzel, O., Sedláček, J. and Šajgalík, P. (2014). New approach for distribution of carbon nanotubes in alumina matrix. Journal of the European Ceramic Society, 34(7), pp.1845-1851.

[113] Tjong, S.C. (2013). Recent progress in the development and properties of novel metal matrix nanocomposites reinforced with carbon nanotubes and graphene nanosheets. Materials Science and Engineering: R: Reports, 74(10), pp.281-350.

[114] Gupta, V. and Saleh, T.A. (2011). Syntheses of carbon nanotube-metal oxides composites; adsorption and photo-degradation. In Carbon Nanotubes-From Research to Applications. IntechOpen.

[115] Chanaewa, A., Juárez, B.H., Weller, H. and Klinke, C. (2012). Oxygen and light sensitive field-effect transistors based on ZnO nanoparticles attached to individual double-walled carbon nanotubes. Nanoscale, 4(1), pp.251-256.

[116] Wang, X., Wang, W. and Liu, Y. (2012). Enhanced acetone sensing performance of Au nanoparticles functionalized flower-like ZnO. Sensors and Actuators B: Chemical, 168, pp.39-45.

[117] Shen, Y., Bi, H., Li, T., Zhong, X., Chen, X., Fan, A. and Wei, D. (2018). Low-temperature and highly enhanced NO_2 sensing performance of Au-functionalized WO_3 microspheres with a hierarchical nanostructure. Applied Surface Science, 434, pp.922-931.

[118] Tian, F., Liu, Y. and Guo, K. (2014). Au nanoparticle modified flower-like ZnO structures with their enhanced properties for gas sensing. Materials Science in Semiconductor Processing, 21, pp.140-145.

[119] Chen, W., Gao, T., Li, Q. and Gan, H. (2014). Enhanced gas sensing properties of flower-like ZnO nanostructure to acetylene. Materials Technology, 30(2), pp.96-100.

[120] Jiao, W. and Zhang, L. (2013). Preparation and gas sensing performances of palladium surface-modified flower-like SnO_2 nano-powders. Material science, 11(6), pp.743-747.

[121] Shingange, K., Tshabalala, Z., Ntwaeaborwa, O., Motaung, D. and Mhlongo, G. (2016). Highly selective NH_3 gas sensor based on Au loaded ZnO nanostructures prepared using microwave-assisted method. Journal of Colloid and Interface Science, 479, pp.127-138.

[122] Katoch, A., Byun, J., Choi, S. and Kim, S. (2014). One-pot synthesis of Au-loaded SnO_2 nanofibers and their gas sensing properties. Sensors and Actuators B: Chemical, 202, pp.38-45.

[123] Yu, J.H., Choi, G.M. (1998). Electrical and CO gas sensing properties of ZnO-SnO_2 composites. Sens. Actuators. B, 52, pp. 251-256

[124] De Lacy Costello, B.P.J.; Ewen, R.J.; Jones, P.R.H.; Ratcliffe, N.M.; Wat, R.K.M (1999). A study of the catalytic and vapour-sensing properties of zinc oxide and tin dioxide in relation to 1-butanol and dimethyldisulphide. Sensors and Actuators B, 61, pp.199-207.

[125] Yoon, D.H.; Yu, J.H., Choi, G.M (1998). CO gas sensing properties of ZnO-CuO composite. Sensors And Actuators. B, 46, 15-23

[126] Choi, S., Katoch, A., Zhang, J. and Kim, S. (2013). Electrospun nanofibers of CuOSnO2 nanocomposite as semiconductor gas sensors for H_2S detection. Sensors and Actuators B: Chemical, 176, pp.585-591.

[127] Chaudhari, G., Bende, A., Bodade, A., Patil, S. and Sapkal, V. (2006). Structural and gas sensing properties of nanocrystalline TiO_2:WO_3-based hydrogen sensors. Sensors and Actuators B: Chemical, 115(1), pp.297-302.

[128] Xu, C., Miura, N., Ishida, Y., Matsuda, K. and Yamazoe, N. (2000). Selective detection of NH_3 over NO in combustion exhausts by using Au and MoO_3 doubly promoted WO_3 element. Sensors and Actuators B: Chemical, 65(1-3), pp.163-165.

[129] Zheng, Y., Sauter, U. and Moos, R. (2018). Oxygen transport paths in screen-printed Pt-Al_2O_3 composite model electrodes on YSZ. Solid State Ionics, 316, pp.53-58.

[130] Tamaki, J., Miyaji, A., Makinodan, J., Ogura, S. and Konishi, S. (2005). Effect of micro-gap electrode on detection of dilute NO_2 using WO_3 thin film microsensors. Sensors and Actuators B: Chemical, 108(2), pp.202-206.

[131] Hazra, S. and Basu, S. (2006). Hydrogen sensitivity of ZnO p–n homojunctions. Sensors and Actuators B: Chemical, 117(1), pp.177-182.

[132] Wang, C., Chu, X. and Wu, M. (2006). Detection of H_2S down to ppb levels at room temperature using sensors based on ZnO nanorods. Sensors and Actuators B: Chemical, 113(1), pp.320-323.

[133] Hosseini, Z., zad, A. and Mortezaali, A. (2015). Room temperature H_2S gas sensor based on rather aligned ZnO nanorods with flower-like structures. Sensors and Actuators B: Chemical, 207, pp.865-871.

[134] Kashyout, A., Soliman, H., Shokry Hassan, H. and Abousehly, A. (2010). Fabrication of ZnO and ZnO:Sb Nanoparticles for Gas Sensor Applications. Journal of Nanomaterials,10, pp.1-8.

[135] Lee, K., Chung, G., Phan, D. and Uddin, A. (2015). Fabrication of low-temperature acetylene gas sensor based on Ag nanoparticles-loaded hierarchical ZnO nanostructures. Electronics Letters, 51(7), pp.572-574.

[136] Shishiyanu, S., Shishiyanu, T. and Lupan, O. (2005). Sensing characteristics of tin-doped ZnO thin films as NO_2 gas sensor. Sensors and Actuators B: Chemical, 107(1), pp.379-386.

[137] Rout, C., Hegde, M. and Rao, C. (2008). H_2S sensors based on tungsten oxide nanostructures. Sensors and Actuators B: Chemical, 128(2), pp.488-493.

[138] Wang, S., Shen, C., Su, J. and Chang, S. (2015). A room temperature nitric oxide gas sensor based on a copper-ion-doped polyaniline/tungsten oxide nanocomposite. Sensors, 15(4), pp.7084-7095.

[139] Bendahan, M., BoulmanI, R., Seguin, J. and aguir, K. (2004). Characterization of ozone sensors based on WO reactively sputtered films: influence of O concentration in the sputtering gas, and working temperature. Sensors and Actuators B: Chemical, 100(3), pp.320-324.

[140] Jiao, Z., Wu, M., Gu, J. and Sun, X. (2003). The gas sensing characteristics of ITO thin film prepared by sol–gel method. Sensors and Actuators B: Chemical, 94(2), pp.216-221.

[141] Yano, M., Iwata, T., Murakami, S., Kamei, R., Inoue, T. and Koike, K. (2018). Gas Sensing Characteristics of a WO_3 Thin Film Prepared by a Sol-Gel Method. In Multidisciplinary Digital Publishing Institute Proceedings. 2 (13), pp. 723-723.

[142] Han, N., Wu, X., Chai, L., Liu, H. and Chen, Y. (2010). Counterintuitive sensing mechanism of ZnO nanoparticle based gas sensors. Sensors and Actuators B: Chemical, 150(1), pp.230-238.

[143] Rothschild, A. and Komem, Y. (2004). The effect of grain size on the sensitivity of nanocrystalline metal-oxide gas sensors. Journal of Applied Physics, 95(11), pp.6374-6380.

[144] Qi, Q., Zhang, T., Zheng, X., Fan, H., Liu, L., Wang, R. and Zeng, Y. (2008). Electrical response of Sn_2O_3-doped SnO_2 to C_2H_2 and effect of humidity interference. Sensors and Actuators B: Chemical, 134(1), pp.36-42.

[145] Gong, J., Chen, Q., Lian, M., Liu, N., Stevenson, R. and Adami, F. (2006). Micromachined nanocrystalline silver doped SnO_2 H_2S sensor. Sensors and Actuators B: Chemical, 114(1), pp.32-39.

[146] Egashira, M., Nakashima, M., Kawasumi, S. and Selyama, T. (1981). Temperature programmed desorption study of water adsorbed on metal oxides. 2. Tin oxide surfaces. The Journal of Physical Chemistry, 85(26), pp.4125-4130.

[147] Malyshev, V. and Pislyakov, A. (2008). Investigation of gas-sensitivity of sensor structures to hydrogen in a wide range of temperature, concentration and humidity of gas medium. Sensors and Actuators B: Chemical, 134(2), pp.913-921.

CHAPTER 3

3.0 Characterization Techniques

Various characterization techniques were used to analyse the structural, physical, optical, chemical and surface properties of nanomaterials. Techniques such as X-ray diffraction (XRD), Transition Electron Microscopy (TEM), Raman spectroscopy, Ultraviolet-Visible Spectroscopy (UV-Vis), Brunauer-Emmet-Teller (BET) and Fourier Transform Infrared Spectroscopy (FTIR). Gas sensing measurements were conducted using the KINESISTEC testing station.

3.1 X-ray Diffractometer (XRD)

Figure 3.1 showed a digital image of the XRD instrument. The instrument was used for structural analysis including the phase structure and composition. The XRD has an effective non-destructive characterization technique used in material science for the identification of crystalline structure. The XRD used for this application was a D8 advance diffractometer equipped with Lynx-eye XE detector operated between 5 and 2θ. This XRD utilizes cobalt X-ray source radiation. For this study, the powder samples were mounted on an amorphous silicon sample holder and the compound identification was conducted by comparing the measured spectra with the database (JCPDS, Card No. 4-784). The beam of X-rays with a wavelength of 0.5 to 2 A, is governed by Bragg's law as shown in Equation 3.1

$$n\lambda = 2d \sin\theta \ldots\ldots\ldots\ldots\ldots (3.1)$$

Where n =1, d is the interplanar spacing between the atomic planes in the crystalline phase, λ is the wavelength (λ = 1.5418) and θ is the angle of incidence.

The nanoscale of the nanomaterials causes the broadening of the peaks due to the crystal structure [1]. The nanoparticles sizes can be determined from the broadening of the peaks by using the Debye-Scherrer equation shown in Equation 3.2

$$d = \frac{0.9\lambda}{\beta \cos\theta} \ldots\ldots\ldots\ldots\ldots\ldots\ldots (3.2)$$

Where d is the diameter of the nanoparticles, λ is the wavelength of the incident x-ray, β is the width and θ is the angle of incidence.

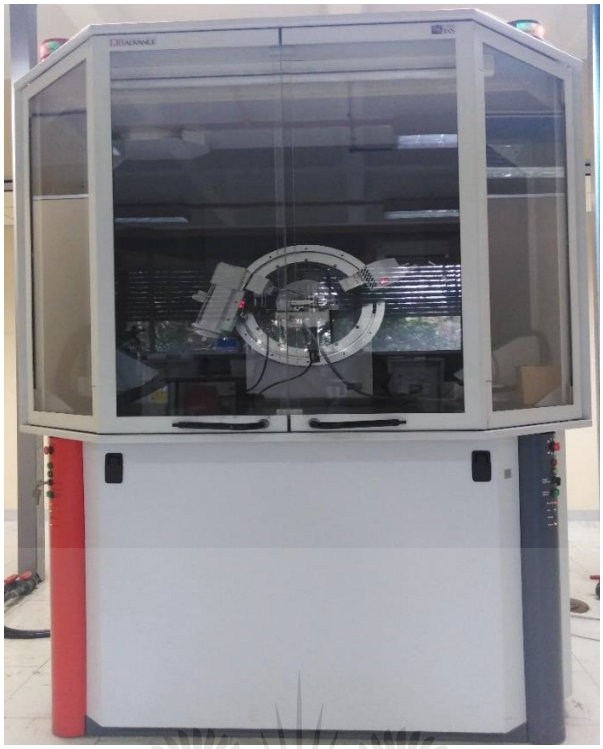

Figure 3.1: Digital image of the XRD equipment.

3.2 Transition Electron Microscopy (TEM)

The digital image of the high-resolution Transmission Microscopy (HRTEM) is depicted in Figure 3.2. HRTEM is spatial imagine equipment whereby a beam of electrons is propagated through a specimen and detected on the other side of the sample, resulting in an image. The resultant image is then enlarged and focused to appear on a fluorescent screen [2]. The HRTEM is often used to determine the size and morphology of the nanomaterials. In this study, JEOL TEM-2100F, JEM-200kV transmission electron microscopy (TEM) operating at 200kV was used to investigate the size and morphology of AuNPs, CNTs and ZnO nanostructures. The CNTs and ZnO nanostructures were prepared by dispersing them in ethanol and ultra-sonicated, while the AuNPs were dispersed in water. The droplets of individual solutions of the homogeneous mixture were placed in fomvar film-coated copper grid. After the solution is dry, it was mounted in the TEM.

Figure 3.2: Digital image of TEM equipment

3.3 Brunauer–Emmett–Teller (BET)

BET is a technique used to measure pore volume and surface area of the nanomaterials. The BET works by physical adsorption of a monolayer of gas on the surface of the solid. A monolayer of nitrogen gas at -70^{0}C from the BET isotherms is usually used because of the weak interaction between gaseous and solid phases. The principle of capillary condensation together with the equivalent capillary model is used to determine the pores, pore distribution and volume while the monolayer formation is used to determine the surface area. Different pores are treated as capillaries with different sizes [3]. The pore size distribution is calculated by the quantity of the adsorbed gas molecules. The gas is adsorbed on the pore walls and the thickness increases with the increase in pressure. The digital image of BET is shown in Figure 3.3.

For this study, the surface area (S_{BET}) of ZnO and composites were measured by the isotherms of nitrogen physical adsorption and desorption of raw Na-Bt and PILCs using TRISTAR 3000 analyser. The BET equation is shown in Equation 3.3. Nitrogen gas adsorption was used to measure the surface area of the ZnO. The samples were degassed under vacuum at 150^{0}C for 4h.

$$\frac{1}{V_a(\frac{P_O}{P}-1)} = \frac{C-1}{V_m C} \times \frac{P_O}{P} + \frac{1}{V_m C} \ldots\ldots\ldots\ldots\ldots\ldots (3.3)$$

Where V_a is the volume of the absorbed gas at standard temperature and pressure, P_O is the saturated pressure of the adsorbed gas, P is the partial vapour pressure of the adsorbed gas, C is a constant and V_m is the volume of gas adsorbed to produce monolayer on the sample surface.

Figure 3.3: Schematic diagram of the BET equipment

3.4 Raman Spectroscopy

Raman spectroscopy is a technique generally used to observe vibrational modes of the molecules. The digital image of Raman spectroscopy is shown in Figure 3.4. Vibrations are referred to as quantum of energies caused by the collective vibration of atoms in the lattice [4]. During the experiment, a monochromatic laser radiation with a single wavelength is incident upon a sample. The light will either be reflected, absorbed or scattered as it interacts with the sample. The scattering of the laser radiation present data about the molecular structure of the sample, while the change in wavelength provides chemical information. In this study, the Perkin Elmer Raman spectroscopy 400r was used with a 514 nm excitation laser. The ZnO nanostructures and CNTs in powder form were placed in the sample holder and mounted in the spectroscopy.

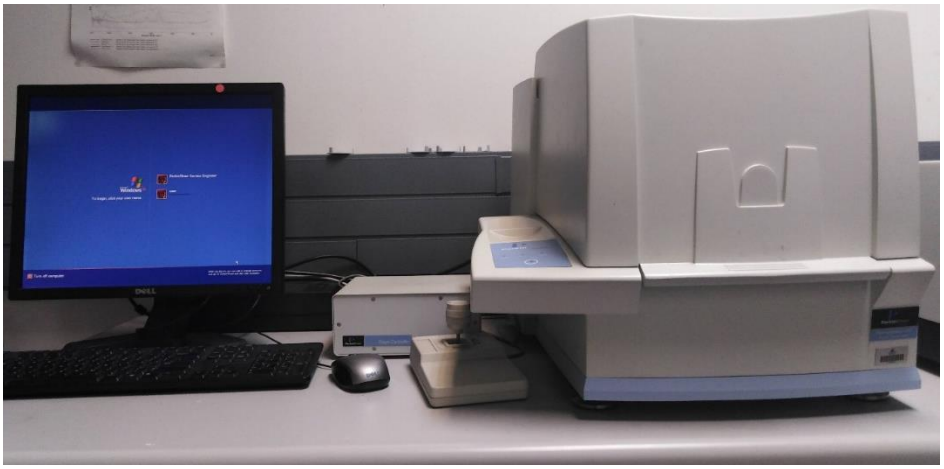

Figure 3.4: Digital image of Raman Spectroscope

3.5 Gas Sensing Measurement

The gas sensing instrument was used for gas sensing analysis of the prepared nanostructures. For this study KENOSISTEC KSGAS6S gas sensor station was used for all testing. The setup of the system consists of a sample stage, four different gas inlet, twelve mass flow controllers to control the gas capacity in the chamber, wet and dry air inlet and mixer, six heaters that supplied voltage to the system and six KEITHLEY Pico ammeter for measuring the conductance [5]. The digital image of the gas sensing station is shown in Figure 3.5.

In this study, the powder ZnO, CNTs/ZnO and Au/ZnO composites samples were dispersed in ethanol to make a paste and subsequently forming the sensing film. The paste was drop coated into the alumina substrate interdigitated Au/Pt electrodes. The sensing film was dried at room temperature before calcination at 500^0C. The sensing films were mounted in the sample holder inside the sensing chamber. The analyte gases are directed to the chamber, the heaters supply voltage throughout the sample and the picommeters record the gas concentrations.

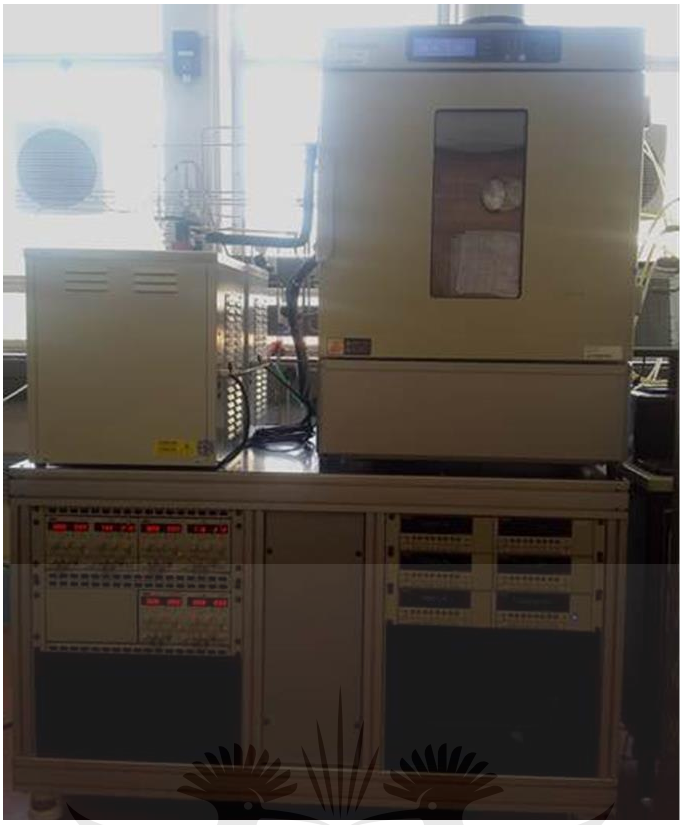

Figure 3.5: Schematic diagram gas sensing station

3.6 Fourier Transform Infrared Spectroscopy (FTIR)

The Fourier Transform Infrared Spectroscopy (FITR) is a technique used to determine amongst other things the functional groups of different nanomaterials. It is used to characterise the structural properties such as vibration frequencies of molecules and crystal structures. FTIR is the analysis of infrared light interacting with the molecules. Typically, the technique measures the wavelength and the intensity of the absorption of infrared light by the sample. The absorbance is measured as a function of frequency containing information about sample vibrations [6]. The frequencies of vibrations between the atom bonds corresponds to the absorption peaks. The digital image of the FTIR is shown in Figure 3.6.

The FTIR consist of infrared energy source, a sample compartment, detector and a computer. The infrared energy source beam passes through the energy control of the sample and subsequently to the detector. The beam enters the interferometer to make precise measurements. The beam passes into the detector for measurement and signal is sent to the computer where the Fourier Transform spectrum takes place. For this study, the FTIR used is the Perkin Elmer UATR, spectra Two. The powder samples of the ZnO and CNTs were mounted in the sample holder.

Figure 3.6: Digital Image of the FTIR technique.

3.7 Ultraviolet-Visible Spectroscopy (UV-Vis)

The Ultraviolet-Visible Spectroscopy (UV-Vis) is a technique used to determine the optical properties of different materials. The UV-Vis works on a principle whereby the sample absorbs the ultraviolet and visible light due to electronic transitions, resulting in the energy absorption versus wavelength. When the sample absorbs the light at a certain wavelength, the transmitted light will be reduced, and the intensity will be plotted as a function of the light wavelength to give a spectrum of the sample absorption. The principle of absorption spectroscopy can be explained using the Beer's and Lambert's law, which states that fraction of incident radiation absorbed is directly proportional to the number of absorbing molecules in its path [4], meaning that the molecules that absorbs the light are directly proportional to the peak intensity in the absorption spectrum. The law is given by (Equation 3.4);

$$\log\frac{I_O}{I} = \varepsilon cI \ldots\ldots\ldots\ldots\ldots\ldots (3.4)$$

Where I_O is the intensity of the incident light, I is the intensity of the light transmitted through the sample, ε is the molar absorptivity of the sample and c is the concentration of the solute.

For this study, the UV-Vis spectrometer used is the Perkin Elmer Lambda 750 and is shown in Figure 3.7. The spectrometer covers the wavelengths between 190 nm to 900 nm and is divided into the ultraviolet (190 nm to 400 nm) and visible (400 nm to 900 nm) regions. The concentration of the sample is also an important fact, because if it is too high then it will lead to saturated absorption. The samples were prepared by sampling the ZnO and Au solutions during synthesis. Before the sample can be placed in the equipment, background should be taken. The background is the cuvette containing the solvent that was used to make the sample

solution. The absorption spectrum of the nanoparticles can be used to determine the particles sizes by observing if the spectrum is blue-shifted. Blue-shift is a shift towards lower wavelengths, which suggest that the size of the nanoparticles is decreasing. There is also red-shift, which is a shift towards higher wavelengths, suggesting that the particle sizes are increasing.

Figure 3.7: Digital image of UV-Vis equipment.

3.8 References

[1] Schoenbeck, T. and Gateshki, M. (2010). PDF Analysis of Nanomaterials using High-energy Radiation on a Laboratory XRD System. Journal of inorganic and general chemistry ,636(11), pp.2096-2096.

[2] Oku, T. (2012). Direct structure analysis of advanced nanomaterials by high-resolution electron microscopy. Nanotechnology Reviews, 1(5). pp. 1-7

[3] Motaung, D., Mhlongo, G., Kortidis, I., Nkosi, S., Malgas, G., Mwakikunga, B., Ray, S. and Kiriakidis, G. (2013). Structural and optical properties of ZnO nanostructures grown by aerosol spray pyrolysis: Candidates for room temperature methane and hydrogen gas sensing. Applied Surface Science, 279, pp.142-149.

[4] Gesquiere, A. (2010). Optical Properties and Spectroscopy of Nanomaterials Optical Properties and Spectroscopy of Nanomaterials. Journal of the American Chemical Society, 132(10), pp.3637-3638.

[5] Barreto, G., Morales, G. and Quintanilla, M. (2013). Microwave Assisted Synthesis of ZnO Nanoparticles: Effect of Precursor Reagents, Temperature, Irradiation Time, and Additives on Nano-ZnO Morphology Development. Journal of Materials, 2013, pp.1-11.

[6] Baraton, M. (2000). FTIR Spectrometry as a Quality Control Method for Surface Engineering of Nanomaterials. MRS Proceedings, 636, pp1-4

CHAPTER 4

4.0 Synthesis of Composite Additives: Gold Nanoparticles and Carbon Nanotubes

4.1 Introduction

Gold is a noble metal which exists in different morphologies with various properties and applications. Gold in nanoscale has become a subject of interest because of its stability in an aqueous medium, toxicity index, and high electrical conductivity [1-3]. Hence, gold nanoparticles are applicable in electrochemical sensors, catalysts, electronics and surface-enhanced Raman spectroscopy. The wide range of applications is attributed to different morphologies of gold such as spherical, triangular, rods and rectangular to mention a few [5].

Different methods have been used in the past to synthesise the gold nanoparticles (AuNPs) such as the Turkevich method, Sonolysis and Brust-Schifffrin. The Turkevich method has been commonly used for the synthesis of AuNPs because it is the simplest, efficient and cost-effective method when compared to other methods [4]. It involves the use of citrate as a reducing agent and capping agent [4-6]. The use of citrate is preferred because it produces uniform, well-distributed and stable AuNPs. Citrate forms a protective layer during the formation of nanoparticles which enables size control. The citrate concentration relative to the gold precursor is an important factor as it affects the surface charge which leads to size-selective formation [6].

Carbon materials exist in various morphologies such as carbon nanotubes, activated carbon, fullerene, mesoporous carbon and graphite [7]. CNTs have been used in different applications such as gas sensing and high-performance electronics [10]. The method used to synthesise the CNTs is the chemical vapour deposition method (CVD). CVD was chosen because it is simple, less energy cost and produces a large quantity of CNTs. Recent studies have shown that properties of CNTs can be enhanced by chemical functionalisation using mostly acids to introduce functional groups on the surface of CNTs [11-13].

4.2 Experimental Procedure

4.2.1 Chemicals

Hydrogen tetrachloroaurate (III) tri-hydrate ($HAuCl_4.3H_2O$, >99% purity), trisodium citrate dehydrate (> 99% purity) and ferrocene (>98% purity) were all purchased from Sigma Aldrich SA and used without further purification. Nitrogen, argon and acetylene gases were purchased from AFROX. Deionised water was used to prepare all the solutions.

4.2.2 Characterisation Techniques

Characterisation of the samples was done using UV-Vis spectra (Lambda 35), high resolution transmission electron microscopy (HRTEM, JOEL-2100F-200 kV), X-ray diffraction (D8 Advance, Lynx-eye XE detector), FTIR and Raman spectroscopy.

4.2.3 Preparation of Gold Nanoparticles

The synthesis of spherical gold nanoparticles was done using the Turkevich method according to Elahi et al. [4]. A solution of 10 mL of $HauCl_4.3H_2O$ (0.029 M) was added to a round bottom flask containing boiling deionized water (1000 mL). The solution was allowed to stir for 5 minutes, followed by the addition of 28 mL of trisodium citrate solution (0.034 M). After two minutes of citrate addition, the solution turned grey then dark purple and then ruby red. The solution was then refluxed on a hotplate for further 30 minutes until the ruby red colour was stable. Finally, the hotplate was switched off, and the solution was further stirred for four (4) hours to complete the growth of gold nanoparticles. Two other solutions of gold nanoparticles were prepared to produce different sizes. This was achieved by different citrate concentrations of 1 mM, 0.8 mM and 0.3 mM. The schematic diagram of the synthesis procedure for AuNPs is shown in Figure 4.1.

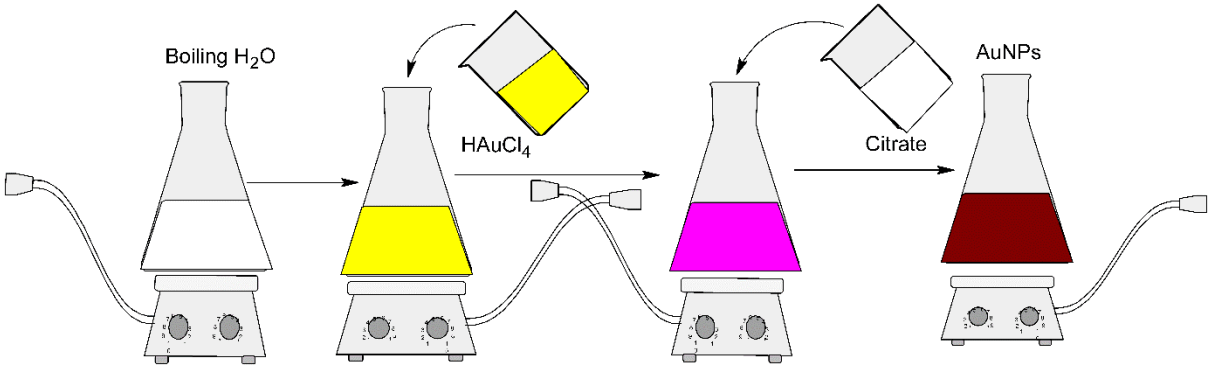

Figure 4.1: Schematic diagram of gold nanoparticles synthesis.

4.2.4 Preparation of Carbon Nanotubes

The carbon nanotubes were prepared by chemical vapour deposition (CVD) technique according to Elsehly et al [11]. Acetylene gas was used as a carbon source and ferrocene (1 g) was used as the catalyst. Nitrogen was used as a carrier gas and to create an inert atmosphere. The reaction was conducted at a temperature of 900˚C to produce carbon nanotubes. Different flowrates of the carbon source gas (150m^3/min, 200 m^3/min, 250 m^3/min) were used. The furnace was allowed to cool down to room temperature and the product formed was collected on the quartz boat and the walls of a quartz tube [7-8, 11]. Figure 4.2 depicts the schematic diagram of the CVD.

The CNTs were functionalized by refluxing them in a 3:1 mixture of sulphuric acid and nitric acid for 6 hours at 120^{0}C under inert conditions using nitrogen. After refluxing, the CNTs (1.5g) were filtered using Whiteman filter paper and then washed in de-ionized water using centrifugation until the pH was neutral (pH~7). The CNTs were dried in an oven overnight at 100℃ before use [11].

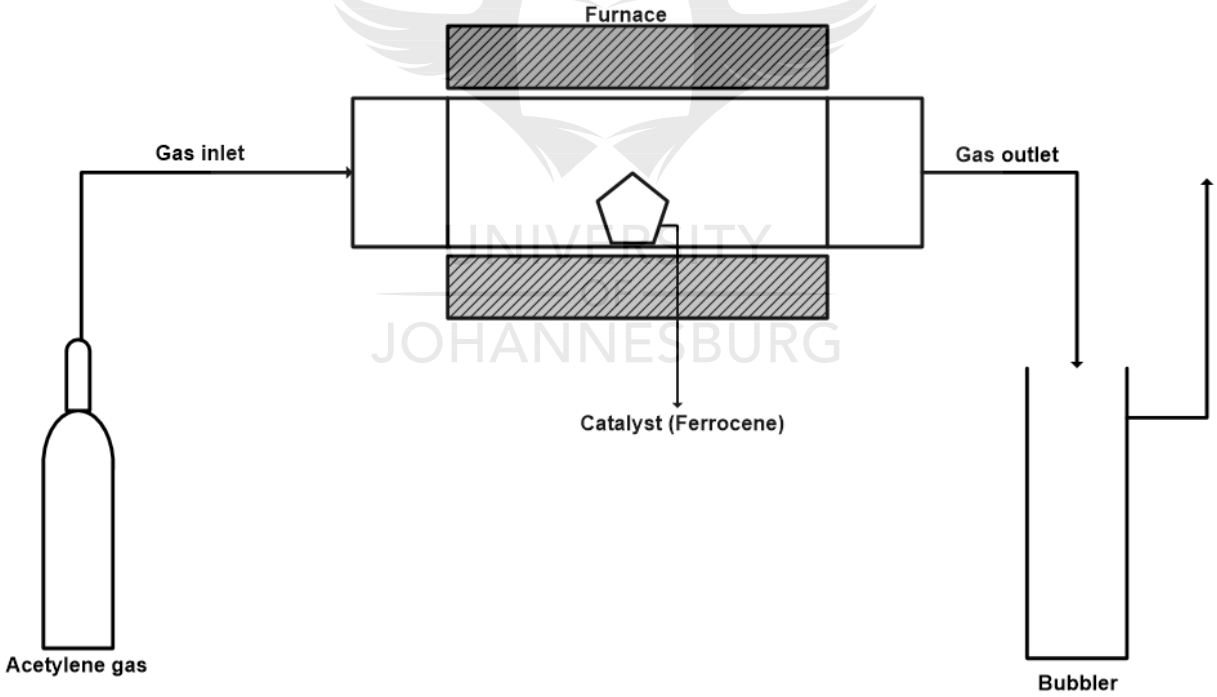

Figure 4.2: Schematic diagram of the chemical vapour deposition.

4.3 Results and Discussion

4.3.1 Part A: Synthesis and Characterisation of Different Sizes of Gold Nanoparticles (AuNPs)

The XRD spectra of samples prepared with citrate concentrations of 0.3 mM, 0.8 mM and 1 mM are shown in Figure 4.3. The XRD spectra of all the samples showed the presence of similar diffraction peaks at a 2-theta angle of 46^0[200], 54^0[110], 78^0[220] and these are characteristics of crystalline Au. The Au peaks were relatively broad which was attributed to the size of gold crystallite, suggesting Au in nanoscale (AuNPs). However, at the citrate concentration of 0.3 mM, there was a presence of extra peaks at a 2-theta angle of 33^0 and 38^0. The presence of the extra peak at 38^0 [111] was indexed to Au, it was caused by the citrate molecules which were not sufficient to hinder the size growth of the particles, which suggest the formation of different shape of AuNPs. Au peaks are typical of face-centred-cubic (FCC) structure of the AuNPs (JCPDS, Card No. 47-784). As the citrate concentration was increased from 0.3 to 1 mM, the XRD spectra showed that the peaks became narrower, which was attributed to a decrease in particle size and highly crystalline.

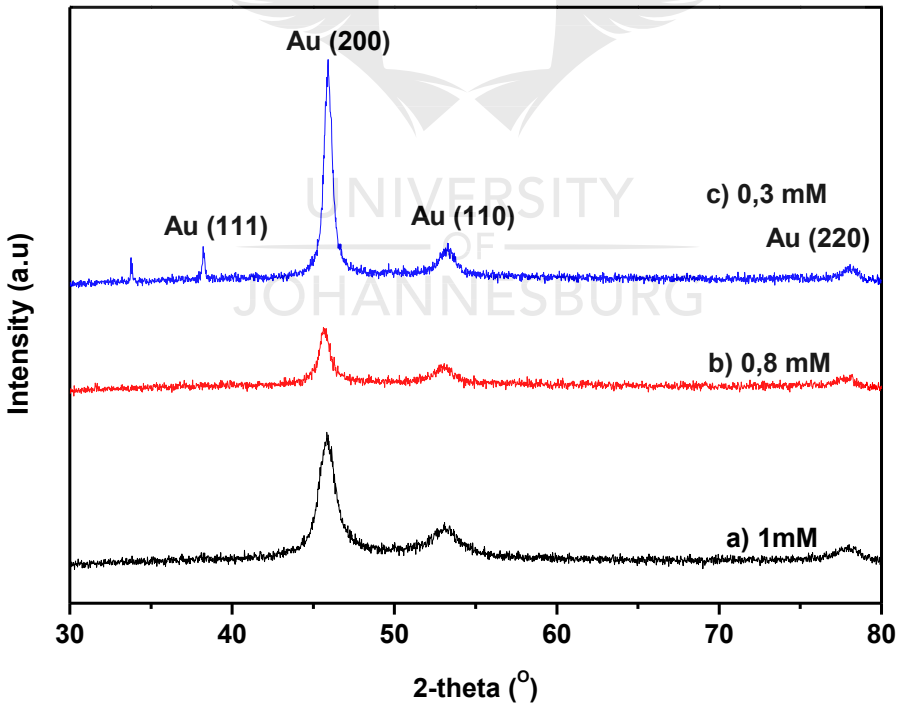

Figure 4.3: XRD patterns of Au nanostructures prepared using different citrate concentrations (a) 1 mM, (b) 0.8 mM and (c) 0.3 mM.

TEM images of samples prepared with citrate concentrations of 0.3 mM, 0.8 mM and 1 mM and their respective particles size distribution histograms are shown in Figure 4.4. The citrate concentration of 1 mM, 0.8 mM and 0.3 mM yielded AuNPs with sizes 14, 27 and 40 nm, respectively. The spherical Au nanoparticle size increased with a decrease in the citrate concentration. This means that as the citrate molecules were reduced, they became insufficient in stopping Au growth hence the size increased. There was also an introduction of irregular shapes that were observed as the citrate concentration was decreased and these were not considered to obtain the particle size distribution of the samples. The histograms showed that the particle size distribution became progressively wider as the size increased. This could be attributed to Au nuclei not growing at a similar rate hence forming AuNPs with varied particle sizes resulting in wider distribution, this was also observed by Nyembe *et al,* [15].

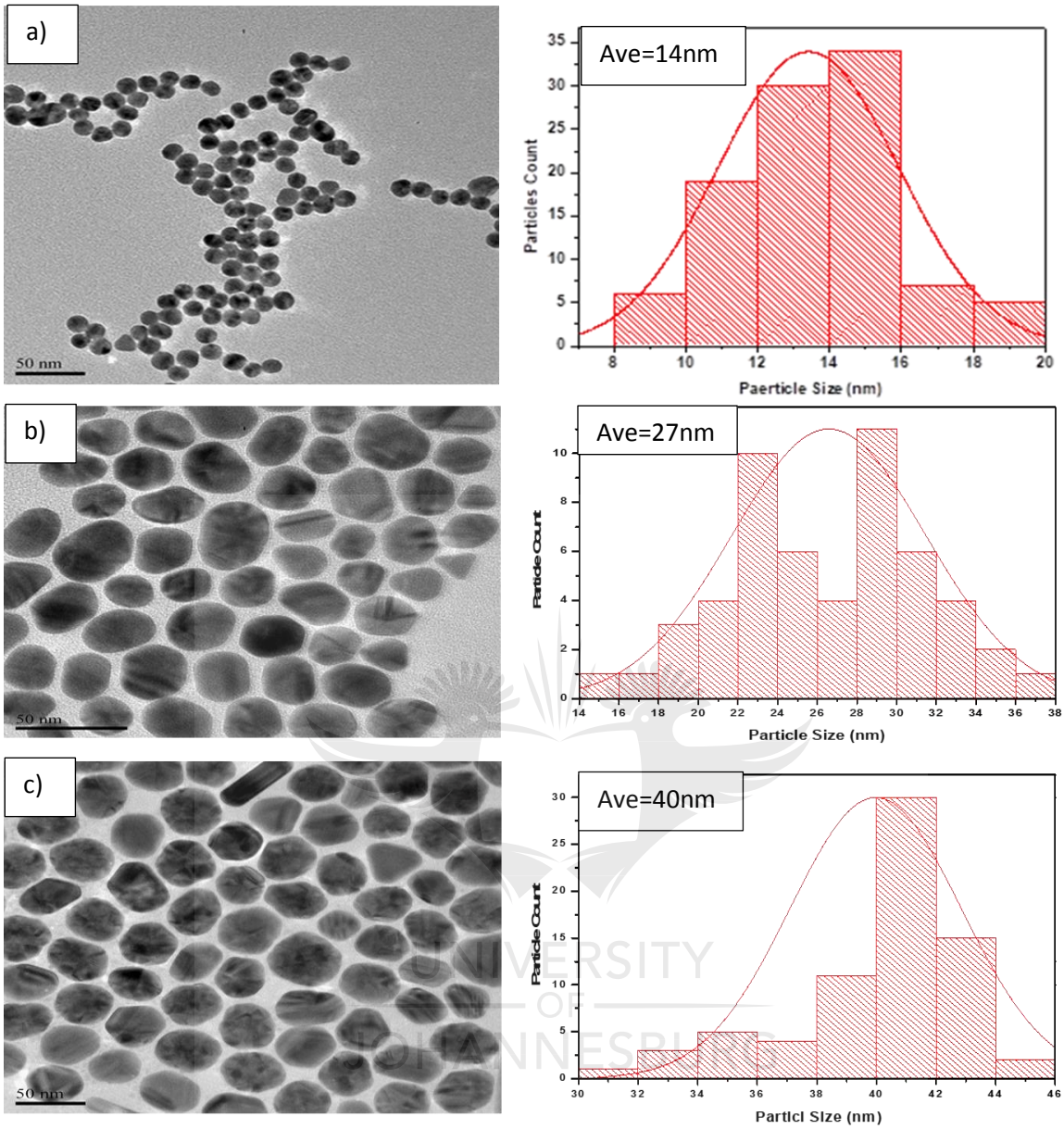

Figure 4.4:TEM images and size distribution histograms of AuNPs with citrate concentration of (a) 1 mM (b) 0.8 mM and (c) 0.3 mM.

The UV-Vis spectra of the AuNPs prepared using different citrate concentrations corresponding to different particles sizes is depicted in Figure 4.5. The UV-Vis spectra showed a monomodal peak for all the samples at wavelengths of 527 nm (particle size = 40 nm), 519 nm (particle size = 27 nm) and 516 nm (particle size = 14 nm). The presence of these peaks at the wavelength 527 nm, 519 nm and 516 nm, suggest the formation of AuNPs which appears between the wavelengths of 450-550 nm [3]. This is in agreement with both the XRD (Figure 4.3) and TEM (Figure 4.4) which both showed that the particles were of Au. The monomodal

peak suggests that the AuNPs in solutions were monodispersed, which suggests that the citrate stabilizer was effective in isolating each particle [15]. The increase in Au particle size from 14 to 40 nm was confirmed by the UV-Vis red-shift from a wavelength of 516 nm (particle size = 14 nm) to 527 nm (particle size = 40 nm). Furthermore, this trend of increasing particle size with a decrease in citrate concentration was also observed by TEM analysis (Figure 4.4).

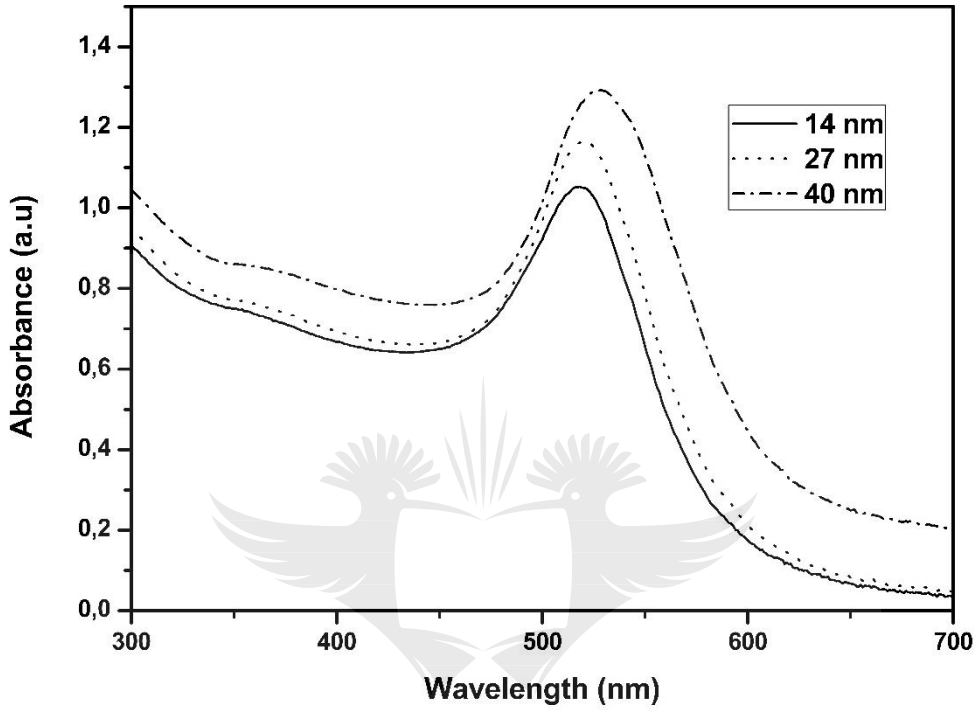

Figure 4.5: UV-Vis spectra of AuNPs of different particles sizes.

4.3.2 Part B: Synthesis of Carbon Nanotubes

The TEM images of CNTs synthesised at different flowrates of the acetylene gas are depicted in Figure 4.6. At the flowrate of 150 m^3/min, the CNTs average size was 95 nm and showed less formation of amorphous carbon. However, at the flowrate of 200 m^3/min, the produced CNTs with an average size of 120 nm showed a significant formation of amorphous carbon on the walls of the CNTs. The average diameter of the CNTs increased at the flowrate of 250 m^3/min to 150 nm and more amorphous carbon was observed. This might be due to the high concentration of the acetylene gas in the furnace resulting in the formation of more amorphous carbons. The TEM images also show that the nanotubes contained an outer and inner diameter. The size of the thickness between the outer and inner diameters suggests that these were multi-walled carbon nanotubes. Furthermore, the synthesis temperature range of 700°C to 900 °C has been reported in literature to yield multi-walled carbon nanotubes [12, 14]

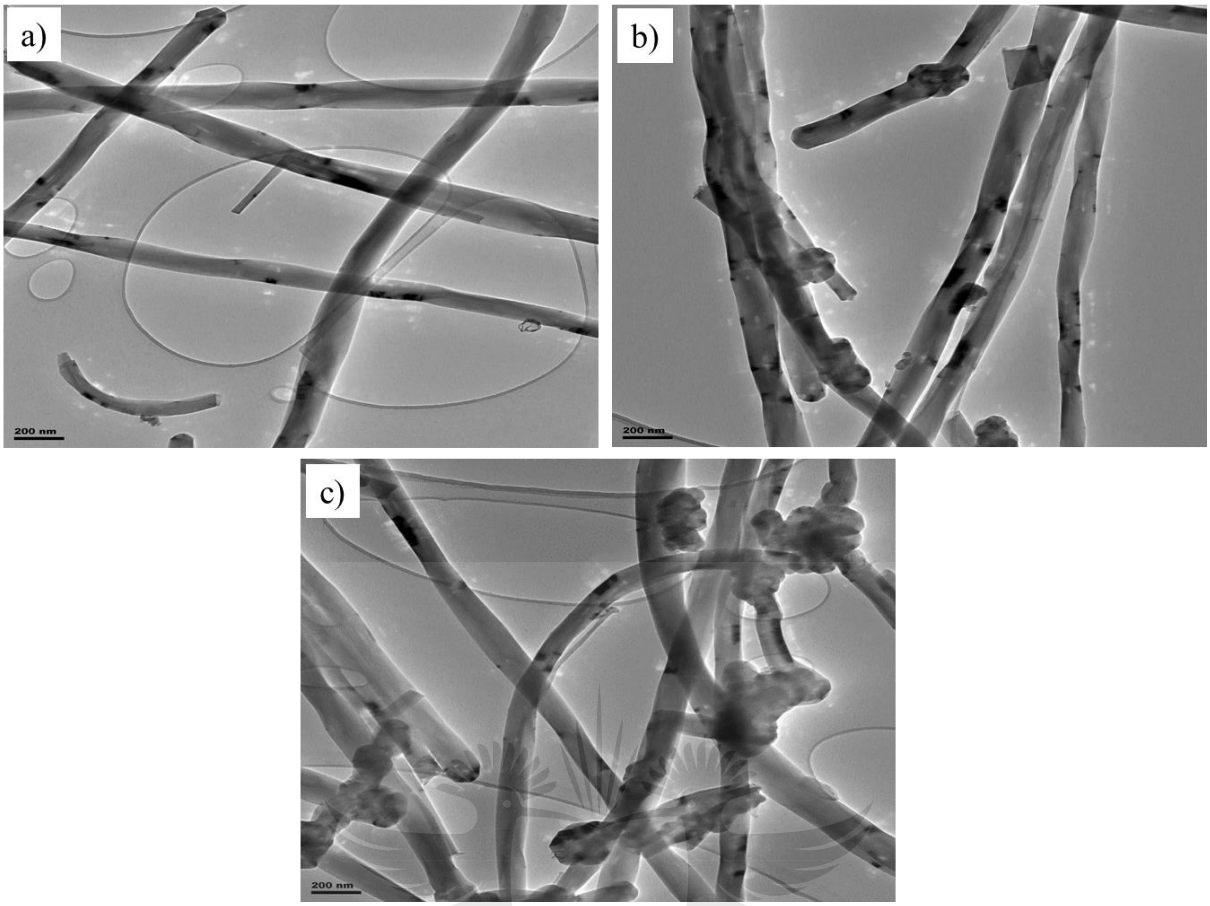

Figure 4.6: TEM images of carbon nanotubes synthesised at carbon source flowrates of (a) 150 m^3/min (b) 200 m^3/min (c) 250 m^3/min.

The FTIR spectra of CNTs after H_2SO_4/HNO_3 functionalisation is depicted in Figure 4.7. The FTIR spectra of the functionalized CNTs at different flowrates indicated common bands representing five different types of bonding. The first broad band at 3437 cm^{-1} was due to the (O-H) functional group vibration stretch. The second vibrational band at 2921 cm^{-1} was due to the C-H bond stretch of the –CHO aldehyde group. This confirmed the direct oxidation of the carbon atoms on the walls of the CNTs by the nitric acid oxidation [16]. The aromatic C=C double bond stretching frequency, which was detected at 1624 cm^{-1} suggested the formation of the graphene structures during the synthesis of the CNTs [17]. The peak at 1394 cm^{-1} was due to an O-H bending mode. The vibrational band at 1102 cm^{-1} occurred due to the presence of the carboxylate ion C-O functional groups.

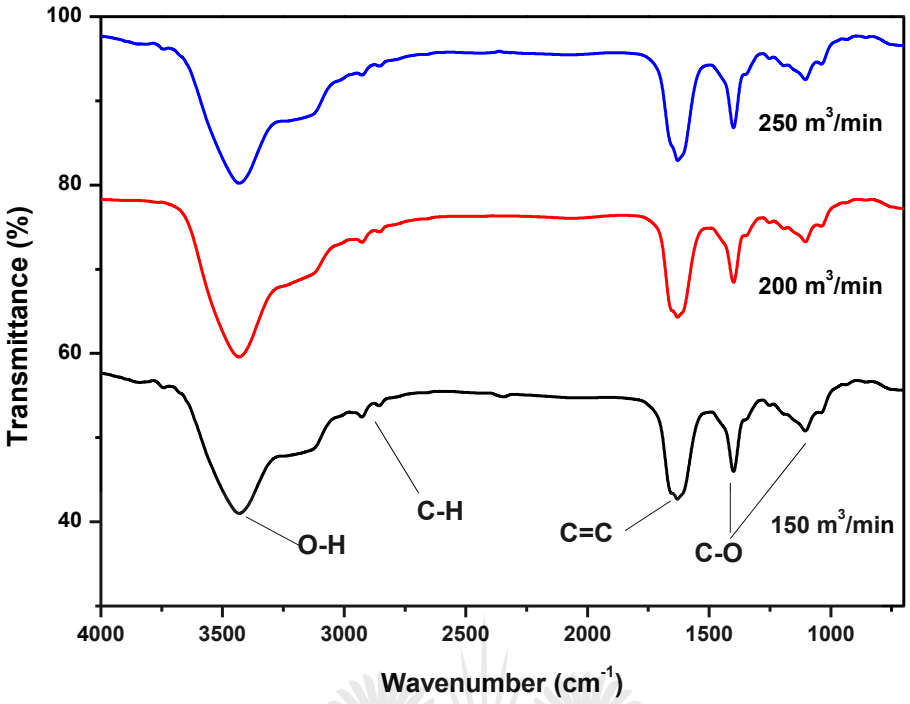

Figure 4.7: FTIR spectra of functionalised carbon nanotubes synthesised at different acetylene gas flowrates.

XRD patterns of CNTs synthesised at different flowrates are depicted in Figure 4.8. All the XRD patterns showed a peak at 30^0 (001) which was consistent with the formation of the graphene layers. The peaks at 50^0 (101) and 65^0 (110) were indexed to carbon nanotubes. The XRD peaks showed a purer species of the CNTs at flowrate of 150 m^3/min, this was shown by the peaks which were more pronounced. TEM analysis (Figure **4.6**) revealed that the 150m^3/min flowrate was the optimal flowrate as it gave CNTs with no or minimal amorphous carbons which was supported by the XRD. From this point on-wards, only the results obtained from 150 m^3/min flowrate will be discussed.

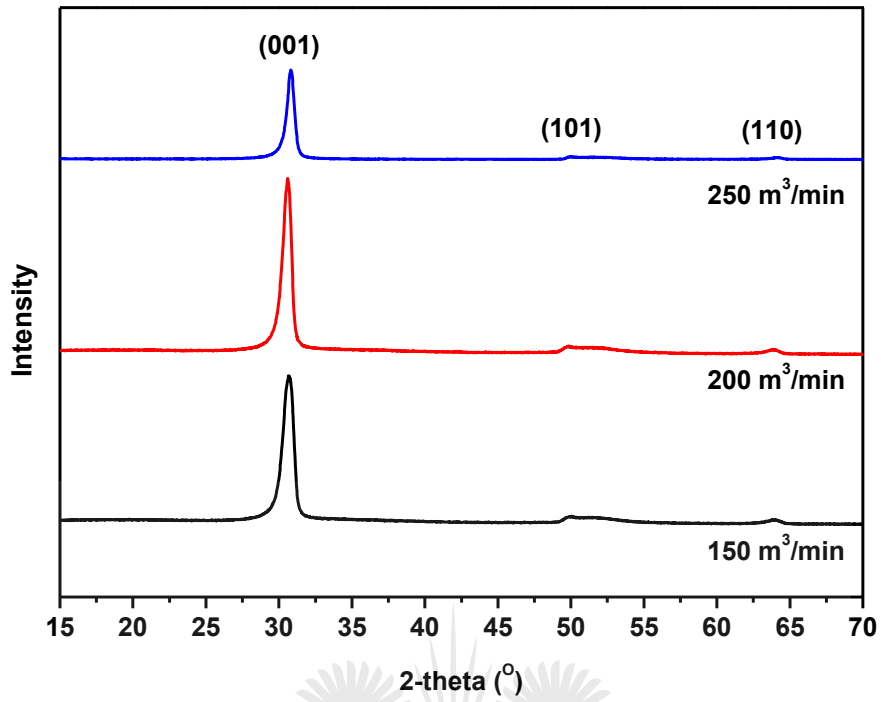

Figure 4.8: XRD pattern of CNTs synthesised at different flowrates

The Raman spectra of CNTs is shown in Figure 4.9. Raman spectroscopy was used to evaluate the extent of functionalization of the MWCNTs. The Raman analysis was conducted on functionalised and non-functionalised CNTs samples obtained at a flowrate of 150 m^3/min. Raman spectrum of the pristine MWCNTs showed two distinct bands at Raman shifts of 1341 cm^{-1} and 1583 cm^{-1}, these bands were associated with the D-band G-bands, respectively [12]. The D-band was a characteristic of C=C bonds on the graphitic plane on the CNTs, while the G-band was the indication of the graphitic structure of the CNTs [18]. The ratio of the intensity of the D-band (I_D) and the G-band intensity (I_G) {i.e. I_D/I_G}, indicated the degree of distortion of the graphitic structure on the CNTs [18]. Upon acid functionalisation of the MWCNTs, the D-band and G-band Raman shifts were retained, however, the I_D/I_G ratio decreased from 0.47 (i.e. for pristine MWCNTs) to 0.41 (i.e. for –COOH functionalized MWCNTs). This indicated that the intensity of the G-band increased upon –COOH functionalisation, indicating some form of disorder on the graphitic planes of the MWCNTs, thus also confirming effective functionalisation of the CNTs which is in agreement with the FTIR results (Figure 4.7).

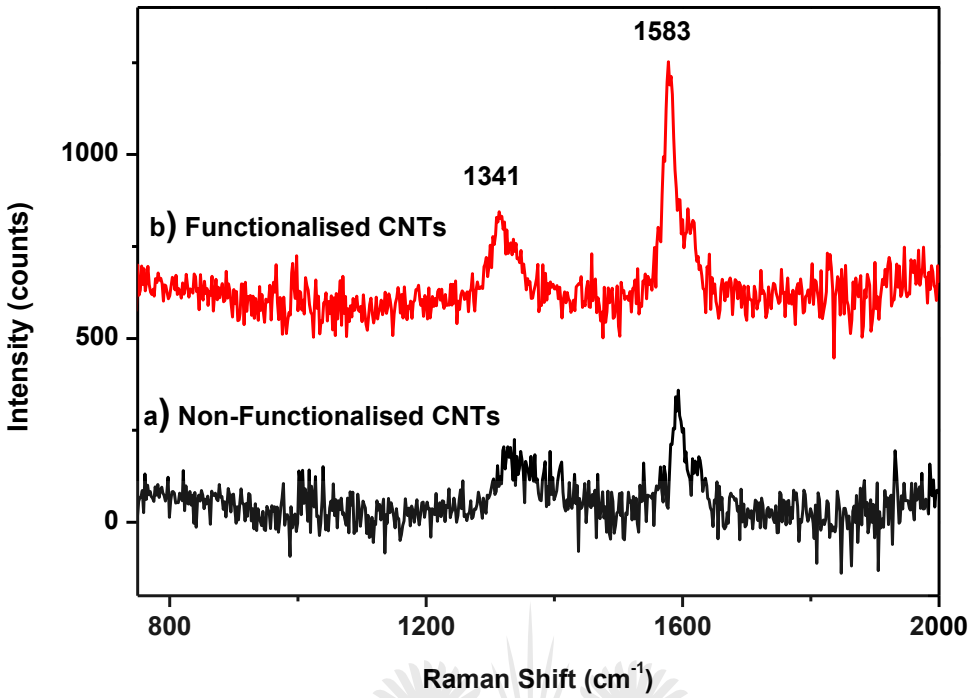

Figure 4.9: The Raman spectroscopy of the (a) pristine (i.e. produced using a flowrate of 150 m3/min) and (b) –COOH functionalised MWCNTs, 6 hours after being subjected to acidification.

4.4 Conclusions

Different citrate concentrations were used to synthesize different sizes of spherical AuNPs. The different particles sizes (14 nm, 27 nm and 40 nm), were achieved by systematically reducing the concentrations of the citrate, thereby affecting the pH which then affects the size of the formed particles. As the concentration of the citrate was decreased from 1 mM to 0.3 mM, the particle sizes increased, and particle shape became more irregular. At high citrate concentration, the stabiliser effect was apparent as it sufficiently capped the gold nanoparticles thus forming smaller sizes, however, at low citrate concentrations the protecting effect of the stabiliser was less, leading to a particle size growth as seen in the TEM micrographs (Figure 4.4). The ratio of citrate molecules to gold ions is crucial for precise particle formation (specific size). The citrate molecules get attached to the crystal planes and inhibit further growth of the AuNPs which led to the formation of a specific particles size. The AuNPs (14 nm) synthesised using 0.1 mM was chosen as ideal to make a composite for gas sensing application, because the particles were well dispersed with relatively narrow size distribution.

Different flowrates of the CNTs were varied to optimise the formation of CNTs. All the synthesised CNTs were functionalised using acids (Nitric and sulphuric acid) to produce –COOH functionalised CNTs. The CNTs were successfully functionalised as the O-H and C-O groups were observed in the FTIR. The well dispersed and pure CNTs were observed at the flowrate of 150 m^3/min. However, as the flowrate increase (i.e. from 200 m^3/min to 250 m^3/min) the presence of amorphous carbons became more apparent.

4.5 References

[1] Maciejewska-Prończuk, J., Oćwieja, M., Adamczyk, Z. and Pomorska, A. (2018). Formation of gold nanoparticle bilayers on gold sensors. Colloids and Surfaces A: Physicochemical and Engineering Aspects, 560, pp.393-401.

[2] Goldys, E. and Sobhan, M. (2012). Gold nanoparticles: fluorescence of colloidal gold nanoparticles is controlled by the Surface Adsorbate. Advanced Functional Materials, 22(9), pp.1989-1989.

[3] Agunloye, E., Panariello, L., Gavriilidis, A. and Mazzei, L. (2018). A model for the formation of gold nanoparticles in the citrate synthesis method. Chemical Engineering Science, 191, pp.318-331.

[4] Elahi, N., Kamali, M. and Baghersad, M. (2018). Recent biomedical applications of gold nanoparticles: A review. Talanta, 184, pp.537-556.

[5] Kimling, J., Maier, M., Okenve, B., Kotaidis, V., Ballot, H. and Plech, A. (2006). Turkevich method for gold nanoparticle synthesis revisited. The Journal of Physical Chemistry B, 110(32), pp.1570-1577.

[6] Grasseschi, D., de O. Pereira, M., Shinohara, J. and Toma, H. (2018). Facile synthesis of labile gold nanodiscs by the Turkevich method. Journal of Nanoparticle Research, 20(2). Pp.25-30.

[7] Kumar, M. (2010). Carbon nanotube synthesis and growth mechanism. Nanotechnology Perceptions, 6(1), pp.7-28.

[8] Kumar, M. and Ando, Y. (2010). Chemical vapour deposition of carbon nanotubes: A review on growth mechanism and mass production. Journal of Nanoscience and Nanotechnology, 10(6), pp.3739-3758.

[9] Zhang, W. and Zhang, W. (2009). Carbon nanotubes as active components for gas sensors. Journal of Sensors, 2009, pp.1-16.

[10] Aroutiounian, V.M. (2015). Metal oxide gas sensors decorated with carbon nanotubes. Lithuanian Journal of Physics, 55(4).

[11] Elsehly, E., Chechenin, N., Makunin, A., Motaweh, H., Vorobyeva, E., Bukunov, K., Leksina, E. and Priselkova, A. (2016). Characterization of functionalized multi-walled carbon nanotubes and application as an effective filter for heavy metal removal from aqueous solutions. Chinese Journal of Chemical Engineering, 24(12), pp.1695-1702.

[12] Gumbi (2015). Fabrication of nanosilver / carbon nanotube polyamide thin-film composite membranes for water treatment. Masters dissertation, University Of Johannesburg, Available at: http://hdl.handle.net/10210/15182.

[13] Balasubramanian, K. and Burghard, M. (2018). Chemically functionalized carbon nanotubes. Journal of Membrane Science, 281(1-2), pp.325-333.

[14] Kong, J., Cassell, A. and Dai, H. (1998). Chemical vapour deposition of methane for single-walled carbon nanotubes. Chemical Physics Letters, 292(4-6), pp.567-574.

[15] Nyembe, S., Mpelane, S., Shumbula, P., Harris, R., Moloto, N. and Sikhwivhilu, L. (2015). The Effects of gold seeds stabilizing agent on gold nanostructures morphologies. Materials Today: Proceedings, 2(7), pp.4149-4157.

[16] Atieh, M.A., Bakather, O.Y., Al-Tawbini, B., Bukhari, A.A., Abuilaiwi, F.A. and Fettouhi, M.B. (2010). Effect of carboxylic functional group functionalized on carbon nanotubes surface on the removal of lead from water. Bioinorganic chemistry and applications, 2010.

[17] Ngo, C.L., Le, Q.T., Ngo, T.T., Nguyen, D.N. and Vu, M.T. (2013). Surface modification and functionalization of carbon nanotube with some organic compounds. Advances in Natural Sciences: Nanoscience and Nanotechnology, 4(3), p.035017.

[18] Saito, R., Hofmann, M., Dresselhaus, G., Jorio, A. and Dresselhaus, M.S. (2011). Raman spectroscopy of graphene and carbon nanotubes. Advances in Physics, 60(3), pp.413-550.

CHAPTER 5

5.0 Synthesis of ZnO Nanostructures and Gas Sensing Application

5.1 Introduction

Zinc Oxide (ZnO) is an n-type semiconductor metal oxide, with an average bandgap of 3.37eV, a relatively large binding energy of 60meV, thermally stable at room temperature and relatively high electron mobility [1-6]. Furthermore, ZnO is non-toxic, easy to produce in bulk quantity and a typical chemiresisitive material making it change its electrical resistance when its surface interacts with reducing or oxidising gas molecules [5].

Different synthesis methods have been developed for the synthesis of ZnO nanostructures. Methods such as chemical precipitation, mechano-chemical process, hydrothermal techniques, and sol-gel have been used to synthesise ZnO nanostructures [7-9]. Different precursors such as zinc sulphate heptahydrate ($ZnSO_4.7H_2O$) and zinc nitrate ($Zn(NO_3)_2$) has been used as the metal precursors. Reducing agents such as NaOH and diethanolamine have been used [8]. The microwave technique is preferred for the synthesis of ZnO because it saves time and is efficient. The microwave technique also provides uniform constant heating of the samples, making it more accurate in the synthesis [10-13].

5.2 Experimental Procedure

5.2.1 Synthesis of Zinc Oxide Using Microwave Oven Digestion

Zinc sulphate heptahydrate ($ZnSO_4.7H_2O$, >99% purity) and sodium hydroxide pallets (NaOH,> 99% purity), were both used as purchased from Sigma Aldrich South Africa. Zinc sulphate ($ZnSO_4.7H_2O$) was used as a metal precursor and NaOH was used as a reducing agent. Deionised water (d-H_2O) was used as the solvent for all the reactions. A zinc sulphate solution of 0.1 M concentration was prepared by dissolving a mass of 7188.53 mg of $ZnSO_4.7H_2O$ in 100 ml of deionised water. Different concentrations of NaOH (0.1 M, 0.2 M, 0.3 M, 0.4 M and 0.5 M) were prepared by dissolving NaOH in 100 ml of deionised water. A concentration of $ZnSO_4.7H_2O$ was kept constant at 0.1 M and was mixed with the various solutions of the NaOH with different concentrations and placed inside the microwave oven. The microwave oven was set at 510 W for 15 minutes and then increased to 680W for 10 minutes. The microwave was then shut down and cooled to room temperature naturally. The precipitates that were produced were allowed to settle and then dried in an oven overnight at 70^0C. The dried precipitates were calcined in air at 500^0C for 2 hours using a muffle furnace after calcination

studies, which showed that 500°C was the optimal temperature for calcination. The muffle furnace temperature was increased gradually at a rate of 5^0C/min, this was done to uniformly heat the sample. The temperature of 500^0C was an optimised calcination temperature. The Schematic diagram of the process is depicted in Figure 5.1.

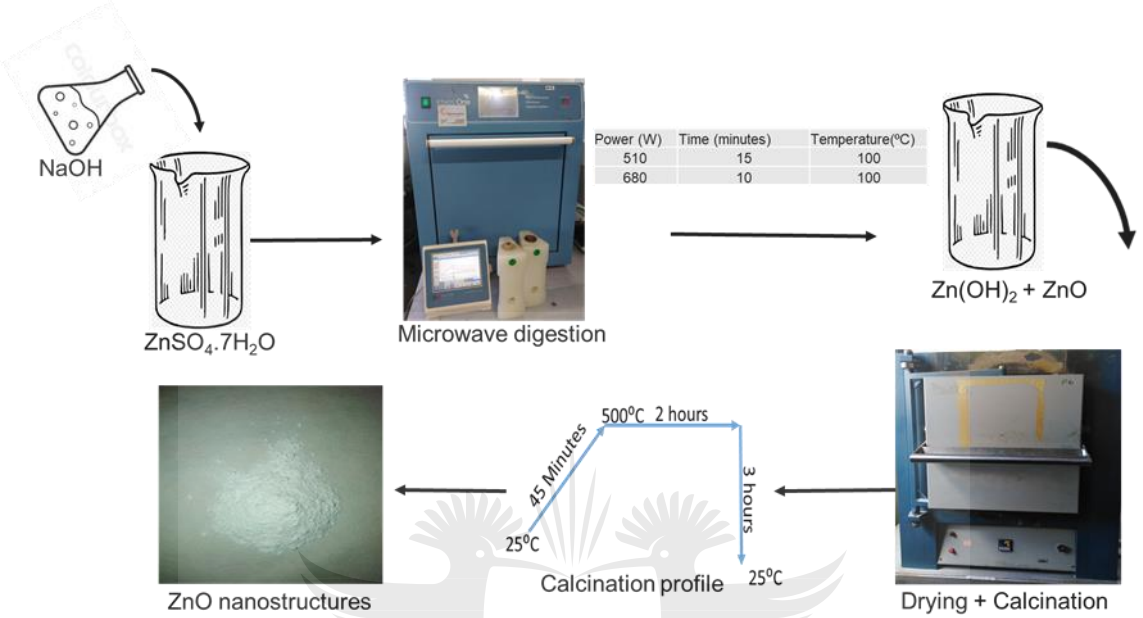

Figure 5.1: Schematic diagram of the synthesis of ZnO.

5.2.2 Brunauer–Emmett–Teller (BET) Analysis

The surface area (S_{BET}) of ZnO (and all other nanomaterials) were measured by the isotherms of nitrogen physical adsorption and desorption of raw Na-Bt and PILCs using a TRISTAR 3000 analyser. The samples were degassed under vacuum at 150^0C for 4h. Other characterisation techniques used are explained in Chapter 3.

5.2.3 Gas Sensor Fabrication and Measurement

ZnO based gas sensor was prepared by mixing the ZnO powder with ethanol to form a paste. The paste was drop-coated onto alumina substrates interdigitated with Au electrodes then dried for 2h. After it was heated at 400^0C for 2 hours to increase the stability, the gas sensing measurements were done using a computer-controlled gas sensing testing station. Carbon monoxide (CO) was injected into the sensing chamber to give out desired gas concentrations. The gas concentrations were varied from 10 ppm to 200 ppm, while the operating temperature was kept constant at 250^0C. The electrical resistance measurements were recorded by Keithley 3706 source meter. The gas sensing performance was analysed in terms of response time and sensitivity.

5.3 Results and Discussion

5.3.1 Characterisation of ZnO nanostructures

The UV-Vis spectra of samples prepared using NaOH concentrations of 0.1 M, 0.2 M, 0.3 M, 0.4 M, and 0.5 M before calcination is depicted in Figure 5.2. The sample prepared using NaOH concentration of 0.1 M showed a peak at 283 nm. This peak was consistent with the formation of the $Zn(OH)_2$ species [14]. However, the spectra of the samples prepared using NaOH concentrations of 0.2 to 0.5 M showed a peak at 365 nm. The presence of the peak at the wavelength of 365 nm is consistent with the presence of ZnO nanostructures. The formation of the ZnO species could be due to the pH levels and temperature effect as stated in the literature [14].

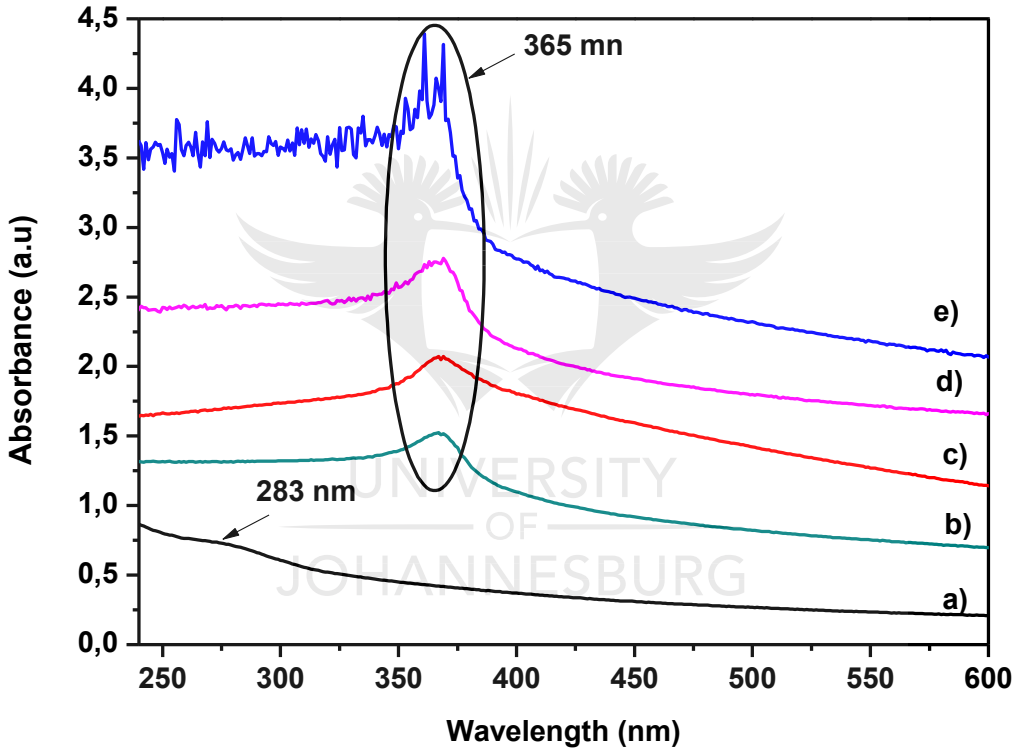

Figure 5.2: UV-Vis spectra of samples synthesised using different NaOH concentration of (a) 0.1 M, (b) 0.2 M, (c) 0.3 M, (b) 0.4 M and (e) 0.5 M.

The XRD patterns of the samples prepared using different NaOH concentrations of 0.1 M, 0.2 M, 0.3 M, 0.4 M, and 0.5 M before calcination is depicted in Figure 5.3. All the samples showed peaks at a 2-theta angle of 10^0(200) and 23^0 (212) which were indexed to $Zn(OH)_2$. The peak at a 2-theta angle of 30^0 (100) was indexed to ZnO. The presence of the peaks at a 2-theta angle of 10^0(200) and 23^0 (212) suggests that $Zn(OH)_2$ was a prevalent phase. However, UV-Vis (Figure 5.2) could not detect the presence of $Zn(OH)_2$ at higher NaOH concentrations of

0.2 M – 0.5 M, possibly due to low concentration or the UV-Vis technique having a higher detection limit for ZnO nanostructures than the concentration of $Zn(OH)_2$ in the sample. The $Zn(OH)_2$ species were pH dependant, and mostly formed at low pH than ZnO [14]. At 0.1 M, the pH was low enough to favour the formation of a significant amount of $Zn(OH)_2$ which was detectable using UV-Vis spectrometer. The concentration of $Zn(OH)_2$ might have been within the detection limit of the UV-Vis spectrometer hence it was able to be detected.

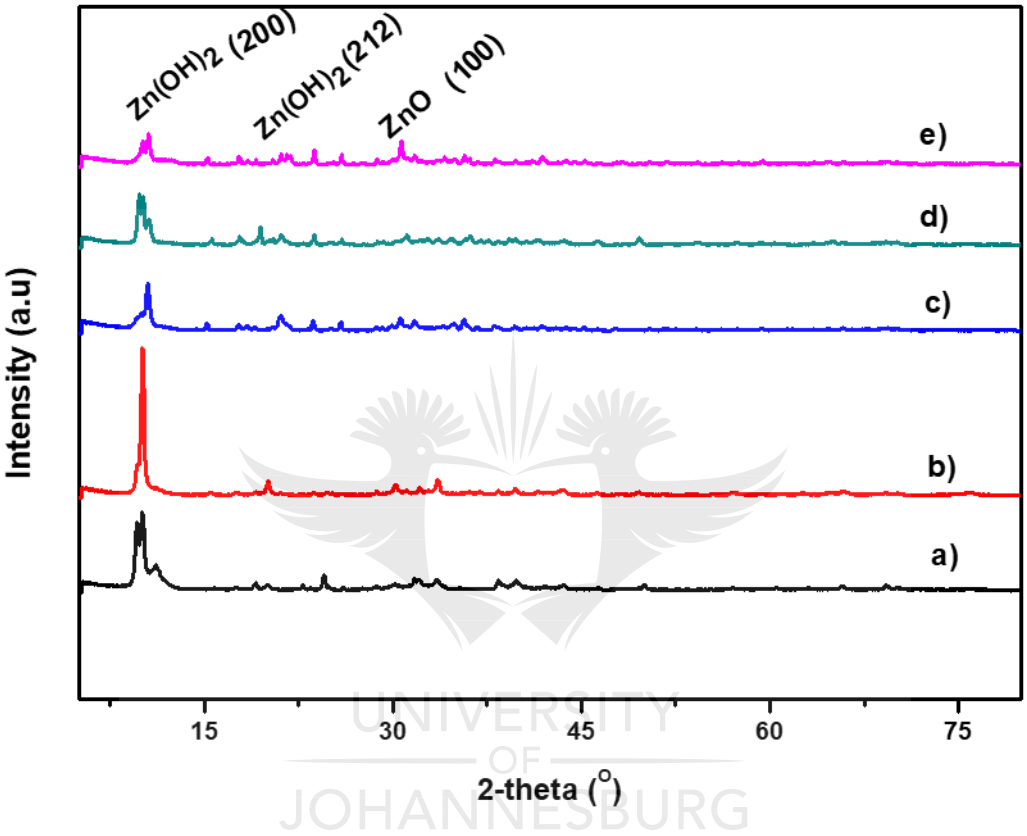

Figure 5.3: XRD patterns of the sample before calcination synthesised using different NaOH concentrations. (a) 0.1 M, (b) 0.2 M, (c) 0.3 M, (b) 0.4 M and (e) 0.5 M.

The FTIR spectra of samples synthesised using different concentrations of NaOH before calcination is depicted in Figure 5.4. The spectra showed a peak at a wavenumber of 3400cm^{-1}, which is consistence with the O-H bond [6]. The presence of this O-H group further suggests the formation of the $Zn(OH)_2$ species which was also detected by the UV-Vis (Figure 5.2) and the XRD (Figure 5.3). The formation of predominantly $Zn(OH)_2$ species suggested that calcination was required. Calcination was done to thermally convert the $Zn(OH)_2$ into ZnO [5].

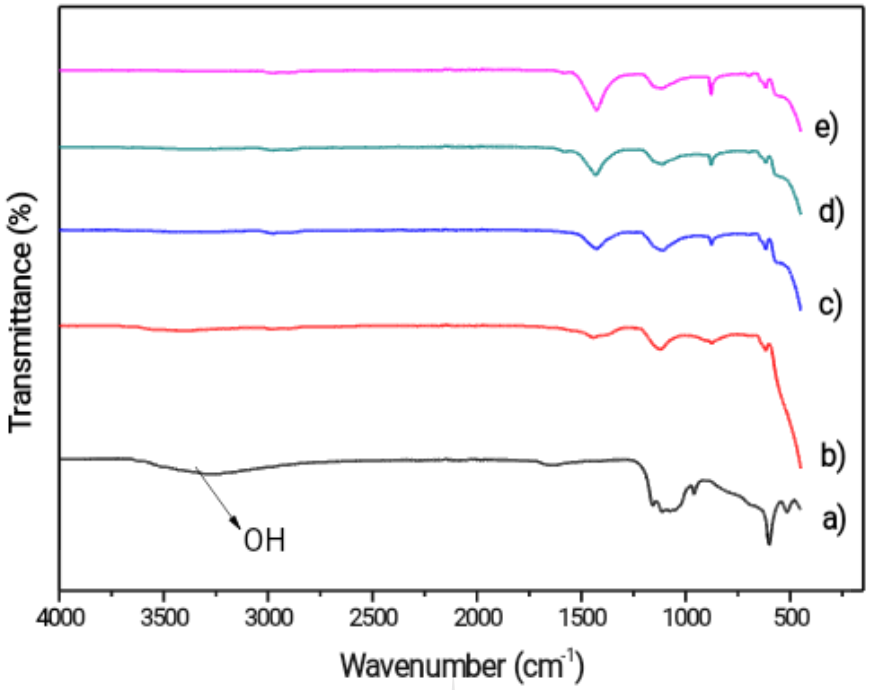

Figure 5.4: FTIR spectra of ZnO before calcination of different NaOH concentrations. (a) 0.1 M, (b) 0.2 M, (c) 0.3 M, (b) 0.4 M and (e) 0.5 M.

Calcination was conducted using the optimised temperature of 500^0C for 2 hours in air. The XRD pattern of ZnO nanostructures after calcination is shown in Figure 5.6 and it revealed the presence of narrow peaks suggesting a crystalline material. The peaks at a 2-theta angle of 34^0 (100), 37^0 (002), 39^0 (101), 52^0 (102), 64^0 (110) and 71^0 (112) were all indexed to pure wurtzite structure of ZnO [10]. This suggested that the ZnO produced after calcination was phase pure. Similar diffraction peaks were observed by Shingange *et al* [19], who synthesised ZnO using the microwave technique at different times.

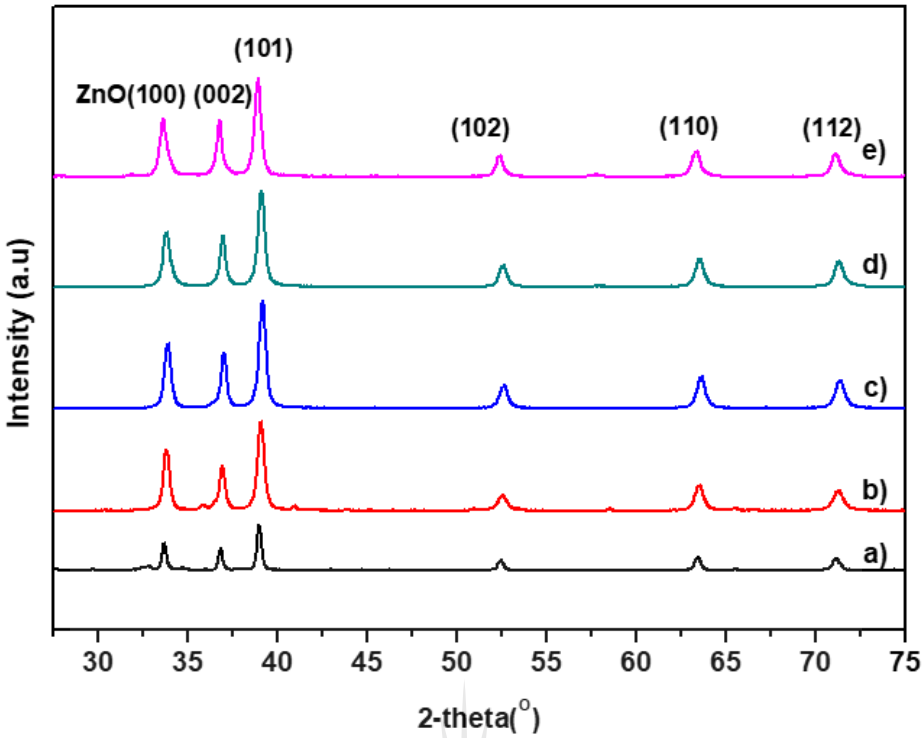

Figure 5.5: XRD patterns of the sample after calcination synthesised at different NaOH concentrations of (a) 0.1 M, (b) 0.2 M, (c) 0.3 M, (b) 0.4 M and (e) 0.5 M.

Figure 5.6 showed the FTIR spectra of the ZnO after calcination of different NaOH concentrations of (a) 0.1 M, (b) 0.2 M, (c) 0.3 M, (b) 0.4 M and (e) 0.5 M. The absence of the O-H peak at a wavenumber of 3400cm^{-1} which was observed before calcination suggest that the ZnO was relatively pure which was the same trend observed in the XRD analysis (Figure 5.5). The formation of a relatively pure ZnO is crucial for gas sensing application in order to avoid any ambiguity of the phase responsible for gas sensing [19]. The use of impure ZnO for gas sensing will give unreliable results in terms of gas sensing parameters.

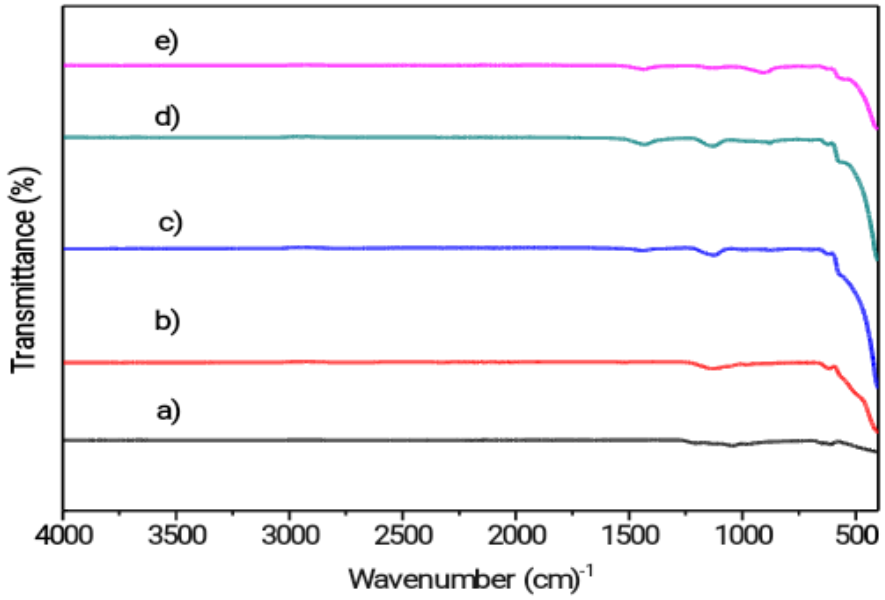

Figure 5.6: FTIR spectra of ZnO after calcination at different NaOH concentrations of (a) 0.1 M, (b) 0.2 M, (c) 0.3 M, (d) 0.4 M and (e) 0.5 M.

Figure 5.7 showed the TEM images of ZnO prepared using different NaOH concentrations. The TEM analysis was conducted after calcination. The TEM images clearly shows different morphologies of ZnO from the various samples. When the concentration of NaOH was 0.1 M, the ZnO formed was hexagonal in shape. Increasing the concentration of the NaOH to 0.2 M changed the morphology of the ZnO to flower-like structures. When the concentration of the NaOH was increased from 0.3 M to 0.5 M, the ZnO became sheet-like. The degree of agglomeration of nanosheets was observed to be increasing with an increase in NaOH concentration (0.3-0.5 M). The change in the morphology of ZnO was due to change in pH as the concentration of the NaOH is increased [14]. The concentration ratio of the precursor and reducing agent also affect the morphology.

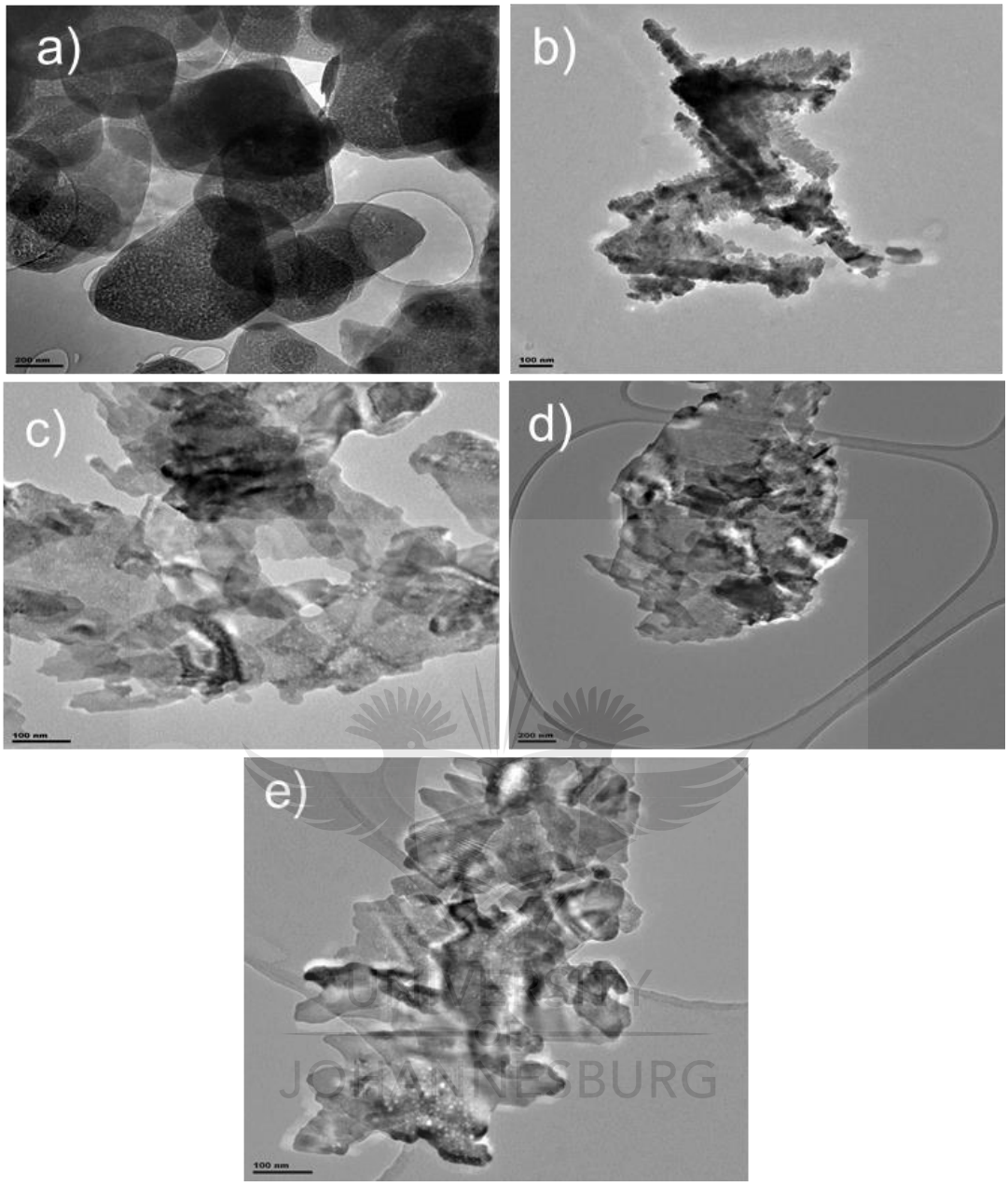

Figure 5.7: TEM images of ZnO synthesised with different concentrations of NaOH. (a) 0.1 M, (b) 0.2 M, (c) 0.3 M, (d) 0.4 M and (e) 0.5 M.

Figure 5.8 showed the Raman spectra of ZnO. The peaks observed from the Raman spectra indicate Raman active modes. The Raman peaks at 452 cm^{-1} and 440 cm^{-1} were ascribed to E_2 (High) Raman shifts, which are characteristics of the ZnO wurtzite crystal formations, which is in agreement with XRD analysis (Figure 5.5). The Raman shifts assigned to Raman active modes in ZnO nanocrystals occurring at relatively higher wavenumbers indicated the formation of nanostructures of ZnO [15]. Increasing the concentration NaOH from 0.1 M to 0.2 M induced a blue-shift (i.e. shift to lower wavenumbers) for the E_2 high Raman shift from 452

cm^{-1} (i.e. 0.1 M NaOH) to 440 cm^{-1} (i.e. 0.2 M NaOH). A shift in the E_2 high Raman spectrum of the ZnO nanostructures indicates internal strains within the wurtzite crystals due to dissimilar growth directions [16]. Thus, ZnO nanostructures with E_2 high Raman shifts resemble different morphologies which were consistent with TEM analysis (Figure 5.7). No stokes shift in the E_2 high bands was observed when 0.2 M, 0.3 M, 0.4 M and 0.5 M NaOH concentrations were used. However, when 0.5 M NaOH was used to prepare the ZnO nanocrystals, it further induced the internal strains on the ZnO wurtzite crystals. These internal strains on the crystal were correlated to the presence of other Raman vibrational modes that occurred at both 440 cm^{-1} and 450 cm^{-1} Raman shifts as highlighted in the spectrum (i.e. for 0.1 M NaOH) [15-16].

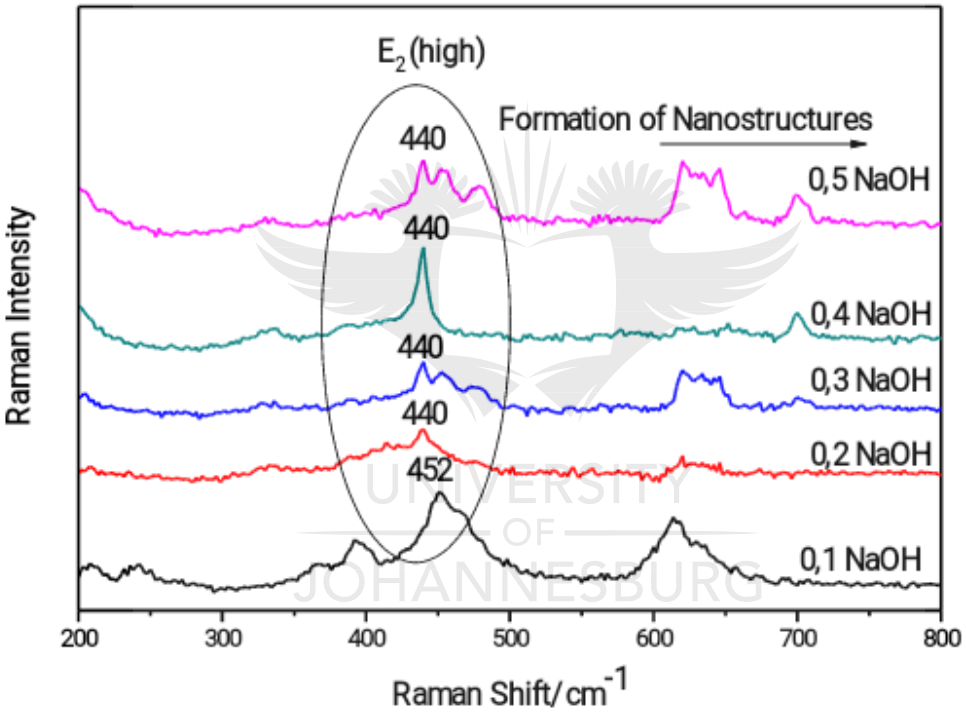

Figure 5.8: Raman spectra of ZnO prepare using various NaOH concentrations

5.3.2 Brunauer–Emmett–Teller (BET)

The surface area results of the samples measured by BET are shown in Table 5.1. The surface area (S_{BET}) was done on 3 different samples prepared using NaOH concentrations of 0.1 M, 0.3 M and 0.5 M in order to get the average trend of the surface area. The surface area increased from 60 m^2/g to 102 m^2/g as the concentration of NaOH increased from 0.1 M to 0.3 M. This could be due to a morphological change of ZnO from hexagonal shape to nanosheets, which have a relatively higher surface area. However, as the concentration of NaOH was increased to 0.5 M, the surface area decreased to 80 m^2/g, this might be due to clustering of ZnO nanosheets

as shown by the TEM image (Figure 5.7). The decrease in the surface area might also be due to excess NaOH as its concentration increases, filling the pores of ZnO resulting in a decrease in surface area. The sample prepared using NaOH concentration of 0.3 M had the highest surface, which was considered ideal for gas sensing because larger surface area results in more binding sites for gas molecules. All the gas sensing analysis were done on this sample. Figure 5.9 showed the graphical representation of ZnO surface area with respect to the NaOH concentration.

Table 5.1: Specific surface area of ZnO samples synthesised using NaOH concentration of 0.1 M, 0.3 M, and 0.5 M

Sample Name	**Specific Surface Area (S_{BET}) (m^2/g)**
0.1 M NaOH	60
0.3 M NaOH	102
0.5 M NaOH	80

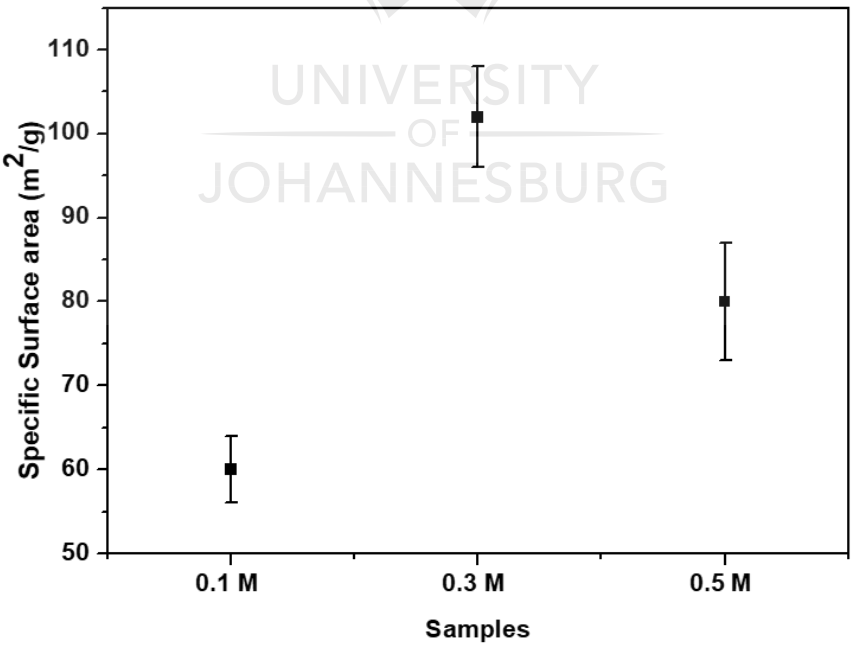

Figure 5.9: ZnO surface area in different NaOH concentration

5.3.3 ZnO based Gas Sensor

Figure 5.10 showed the electrical conductivity changes of the ZnO nanosheets in the presence and absence of carbon monoxide (CO) analyte gas. The CO gas concentration was varied from 10 ppm to 200 ppm and the temperature was kept constant at 250^0C throughout the analysis. In the presence of the CO gas in the surface of ZnO, the electrical conductivity of the ZnO increased. ZnO is a stable n-type semiconductor and upon exposure to a reducing gas such as CO the electrical conductivity increases, which explains the increase in the observed electrical conductivity [15]. However, the electrical conductivity of ZnO did not revert to the initial value when the CO gas was removed, suggesting that the ZnO nanomaterial was not given enough time to fully recover before exposure to the next gas concentration. This is typical of most nanomaterials as they require a relatively long time to fully recover, and for this study, the focus was only on the response time and not the recovery time.

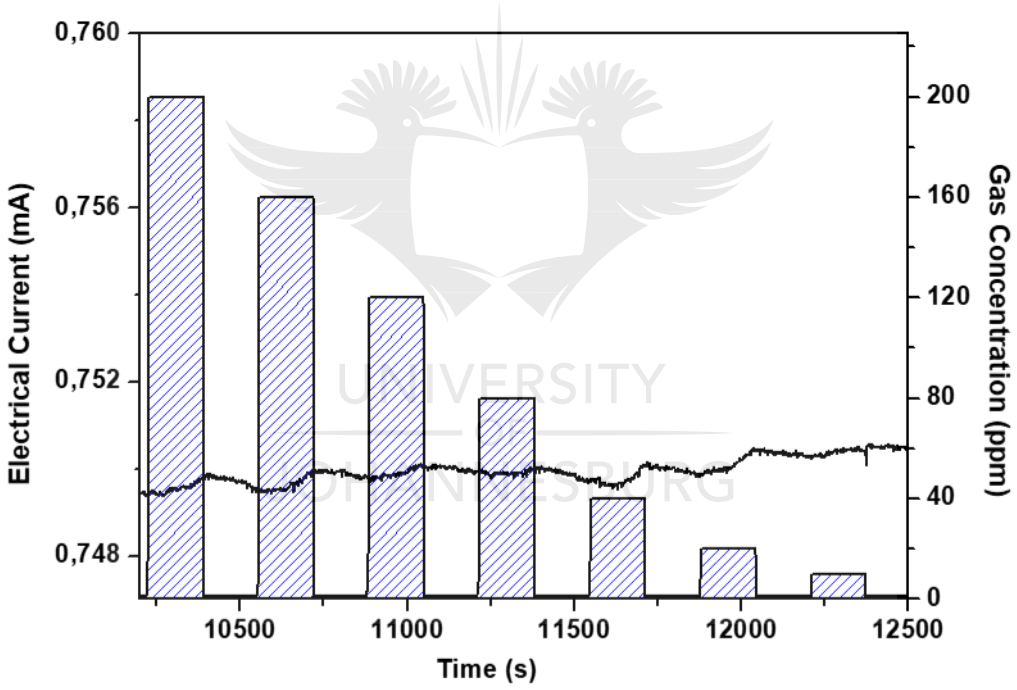

Figure 5.10: Electrical conductivity changes of ZnO exposed to different CO concentration

The sensitivity of the gas is defined as the sensor response to different analyte gas concentrations. It is influenced by the interaction between the material surface and the gas. This interaction is directly proportional to the surface area of the material and the concentration of the analyte gas [18]. The sensitivity (S) of the sensor was determined by measuring the change in the electrical resistance of the ZnO and is expressed as

$$S(\%) = \left[\frac{R_a - R_g}{R_a}\right] \times 100 \ldots\ldots\ldots\ldots\ldots\ldots\ldots (5.1)$$

Where, R_a is the resistance of a sensor in the reference gas, which was air and R_g is the resistance of a gas sensor in the presence of a target gas. In this study, a voltage of 5 V was used for the analysis as it was generated by the system, it was also used to convert electrical current into electrical resistance to calculate the sensitivity. The sensitivity of the sensor was calculated to be it 9.7, 9.8 and 9.9 % at different gas concentrations of 120 ppm, 160 ppm and 200 ppm respectively. The sensor sensitivity depends on the interaction between the target gas and the chemisorbed oxygen species on the surface of the semiconductor, which then leads to a change in electrical conductivity. Therefore, the difference in the sensitivity is attributed to the difference in the interaction between the gas and the surface of the sensor as the gas concentration increases. The more chemisorbed oxygen molecules the better the sensitivity [16]. This trend was expected because the sensitivity of the sensor mainly depends on the removal of the absorbed oxygen species, which generate electrons. Hence at high concentrations of the target gas, there was enough gas to cover the materials resulting in relatively high sensitivity. The TEM (Figure 5.7) also showed a high surface area at ZnO nanosheets synthesized from 0.3 M NaOH, which correspond with high sensitivity. These findings are consistent with what is found in the literature, by Kim *et al* [17] and Ahlers *et al* [18].

Another parameter that was investigated was the response time and is defined as the time required to reach 90% of a stable electrical current after the gas exposure. The response time was calculated at the CO concentration of 200 ppm because this concentration produced relatively higher sensitivity. The response time was calculated to be 114 seconds. Response time of 114 seconds for CO concentration of 200 ppm is not ideal, as by the time the sensor responds, the CO gas would have caused disorientation, unconsciousness or even possible death to living organisms, especially in the mining industry whereby high levels CO gas are produced. A need to improve the response time of ZnO nanosheets is crucial possibly through doping or making a composite with another nanomaterial [18]. Shingange *et al*, [19] investigated the effect of doping on the response time, the findings revealed that the response time was improved by doping the ZnO with AuNPs for NO_2 detection. This shows the need and importance of doping or making a composite with other nanomaterials such as Au and CNTs in order to improve the electrical conductivity and surface area thus improving gas sensing performance [19].

5.4 Conclusions

Different morphologies of ZnO have been successfully synthesised using a microwave-assisted hydrothermal method. Hexagonal, flowerlike and sheets like structures were obtained. The different morphologies depended on the concentration of the reducing agent (NaOH). The NaOH concentrations affected the pH, which in turn determined the morphology and formation of ZnO. A concentration of 0.3 M NaOH, yielded sheet-like nanostructures. These nanostructures were considered to be optimum for gas sensing as it is was phase pure and had the highest surface area of 102 m^2/g, which is crucial for gas sensing. The ZnO nanosheets showed an increasing trend in the sensitivity as the concentration of CO gas increased. The response time was calculated to be 114 seconds at a concentration of 200 ppm. However, there is a need to improve the rapid responsiveness of the ZnO nanosheets. This can be done through making of ZnO nanosheets composites with various nanomaterials in order to improve their response time.

5.5 References

[1] Gentry, S. and Jones, T. (1983). A comparison of metal oxide semiconductor and catalytic gas sensors. Sensors and Actuators, 4, pp.581-586.

[2] Govardhan, K. and Grace, A. (2016). Metal/metal oxide doped semiconductor-based metal oxide gas sensors - A Review. Sensor Letters, 14(8), pp.741-750.

[3] Liu, C., Chen, C. and Leu, J. (2009). Fabrication and CO sensing properties of mesostructured ZnO gas sensors. Journal of The Electrochemical Society, 156(1), pp.16-16.

[4] Leonardi, S. (2017). Two-dimensional zinc oxide nanostructures for gas sensor applications. Chemisensors, 5(2), pp.17-18.

[5] Yadav, B.C., Srivastava, R. and Yadav, A. (2009). Nanostructured Zinc Oxide Synthesized via Hydroxide Route as Liquid Petroleum Gas Sensor (S & M 0750). Sensors and Materials, 21(2), pp.87-87.

[6] Senthilkumar, N., Ganapathy, M., Arulraj, A., Meena, M., Vimalan, M. and Vetha Potheher, I. (2018). Two step synthesis of ZnO/Ag and ZnO/Au core/shell nanocomposites: Structural, optical and electrical property analysis. Journal of Alloys and Compounds, 750, pp.171-181.

[7] Mansournia, M. and Ghaderi, L. (2017). CuO@ZnO core-shell nanocomposites: Novel hydrothermal synthesis and enhancement in photocatalytic property. Journal of Alloys and Compounds, 691, pp.171-177.

[8] Abdullah, M., Shibamoto, S. and Okuyama, K. (2004). Synthesis of ZnO/SiO_2 nanocomposites emitting specific luminescence colors. Optical Materials, 26(1), pp.95-100.

[9] Al-Hada, N., Saion, E., Shaari, A., Kamarudin, M. and Gene, S. (2013). The influence of calcination temperature on the formation of zinc oxide nanoparticles by thermal-treatment. Applied Mechanics and Materials, 446-447, pp.181-184.

[10] Yates, B., Cooper, R. and Kreitman, M. (1971). Low-temperature thermal expansion of zinc oxide. Vibrations in zinc oxide and sphalerite zinc sulfide. Physical Review B, 4(4), pp.1314-1323.

[11] Mohan Kumar, K., Mandal, B., Appala Naidu, E., Sinha, M., Siva Kumar, K. and Sreedhara Reddy, P. (2013). Synthesis and characterisation of flower shaped Zinc Oxide

nanostructures and its antimicrobial activity. Spectrochimica Acta Part A: Molecular and Biomolecular Spectroscopy, 104, pp.171-174.

[12] Krishnakumar, T., Jayaprakash, R., Pinna, N., Singh, V., Mehta, B. and Phani, A. (2009). Microwave-assisted synthesis and characterization of flower shaped zinc oxide nanostructures. Materials Letters, 63(2), pp.242-245.

[13] Kołodziejczak-Radzimska, A. and Jesionowski, T. (2014). Zinc oxide—from synthesis to application: A review. Materials, 7(4), pp.2833-2881.

[14] Moezzi, A., Cortie, M. and McDonagh, A. (2011). Aqueous pathways for the formation of zinc oxide nanoparticles. Dalton Transactions, 40(18), p.4871.

[15] Beniwal, A. (2016). A study & real time monitoring of metal oxide semiconductor (MOS) gas sensor. IOSR Journal of Electronics and Communication Engineering, 01(01), pp.07-12.

[16] Hwang, I. and Lee, J. (2012). Highly sensitive and selective gas sensors using catalyst-loaded SnO_2 nanowires. Journal of Sensor Science and Technology, 21(3), pp.167-171.

[17] Kim, H. and Lee, J. (2014). Highly sensitive and selective gas sensors using p-type oxide semiconductors: Overview. Sensors and Actuators B: Chemical, 192, pp.607-627.

[18] Ahlers, S., Müller, G. and Doll, T. (2005). A rate equation approach to the gas sensitivity of thin film metal oxide materials. Sensors and Actuators B: Chemical, 107(2), pp.587-599.

[19] Shingange, K., Swart, H. and Mhlongo, G. (2018). Au functionalized ZnO rose-like hierarchical structures and their enhanced NO_2 sensing performance. Physica B: Condensed Matter, 535, pp.216-220.

CHAPTER 6

6.0 Fabrication and Gas sensing Performance of Composites

6.1 Introduction

Semiconductor metal oxides (SMOs) such as ZnO, SnO_2, TiO_2 and WO_2 have been used as gas sensing material because they produce highly sensitive sensors [1-3]. However, they have been reported to have high response times [4]. Structural and morphological optimization of these materials has been done to improve the gas sensor performance [5]. Furthermore, material modifications such as doping and chemical surface treatment have been proven to be effective ways of improving the gas sensing performance of the SMOs [5-6]. Metals such as gold (Au) and palladium (Pd) nanoparticles can enhance that catalytic activity of the SMOs [6-7] by enhancing their catalytic oxidation which is important for gas sensing. Carbon nanomaterials such as carbon nanotubes (CNTs) have also been reported to introduce a relatively high surface area, crucial for gas sensing [8-10]. It has been reported in the literature that SMO like titanium oxide has been used for gas sensing and its sensitivity was improved by the use of dopants [11]. Sarala Devi *et al*, [11] investigated the effect of CuO addition on tin dioxide on hydrogen sulphide gas (H_2S) sensor and the sensitivity of the sensor was improved at low concentration. Hosseini *et al* [12] showed that ZnO nanorods doped with Au showed an improved response time compared to undoped ZnO nanorods.

Zak *et al*, [13] investigated the doping of Pb nanoparticles on ZnO nanowires synthesised from thermal evapouration method and found out that the Pb reduced the crystalline quality of the nanowires. Similarly, Gao *et al* [14] synthesised Pd/ZnO composite with simple chemical precipitation and found that the Pb controlled the size and formation of ZnO.

6.2 Experimental Procedure

6.2.1 Preparation of Zinc Oxide and Gold Nanoparticles (Au/ZnO) Composite.

A mass of 400 mg of ZnO powder was mixed with 50 ml of 14 nm gold (Au) solution making 5 w/w% of AuNPs in ZnO nanosheets [10]. The resulting solution was stirred using a magnetic stirrer bar for 1 hour at a rate of 500 rpm. A ruby red to pinkish colour change was noticed. The solution was then dried overnight and characterised. The composite of AuNPs in ZnO nanosheets was done using 0.3 M NaOH concentration because it gave the best ZnO nanostructures (nanosheet) as shown in Chapter 5.

6.2.2 Preparation of Zinc Oxide and Carbon Nanotubes (CNTs/ZnO) Composite.

ZnO (400 g) was mixed with a solution of dispersed CNTs in ethanol making 1 w/w% of CNTs in ZnO nanosheets [11]. The solution was ultra-sonicated for 45 minutes using an electrical sonicator. After ultra-sonication, the composite solution was stirred using a stirrer bar for 1 hour until the mixture was homogenous. The solution turned purple-black in colour. The resulting solution was dried overnight at 70°C and then characterised. The concentration of 0.3 M NaOH was used to make the composite because it showed best ZnO nanosheets which were ideal for gas sensing as shown in Chapter 5.

6.2.3 Brunauer-Emmett-Teller (BET)

The BET analysis was done on three different samples prepared by 0.3 M NaOH concentration, which are ZnO nanosheets, Au/ZnO and CNTs/ZnO.

6.2.4 Gas Sensing

Gas sensing analysis was done on Au/ZnO, CNTs/ZnO and CNTs. The analysis was done using CO gas with a concentration range of 10-200 ppm at a constant temperature of 250^0C. The gas sensing parameters investigated were response time and sensitivity.

6.3 Results and Discussion

6.3.1 Part A: Zinc Oxide (ZnO) Incorporated with Gold Nanoparticles (AuNPs) Composite (Au/ZnO)

Figure 6.1 showed the XRD patterns of (a) ZnO and (b) Au/ZnO samples. The XRD patterns of Au/ZnO composite showed peaks at a 2-theta angle of 37^0 (111), 44^0 (200), 67^0 (220), 34^0 (100), 38^0 (002), 41^0 (101), 54^0 (102), 65^0 (110) and 73^0 (112). The peaks at 37^0 (111), 44^0 (200) and 67^0 (220) were indexed to AuNPs [17], this is consistent with the XRD peaks of pure AuNPs (Figure 4.3) suggesting that the crystal structure of the AuNPs was not altered when incorporated into the ZnO nanosheets. The peaks at a 2-theta angle of 34^0 (100), 38^0 (002), 41^0 (101), 54^0 (102), 65^0 (110) and 73^0 (112) were indexed to pure ZnO [12]. This also shows that the crystalline phase of ZnO was also not altered during the addition of AuNPs. This implies that the Au/ZnO composite synthesis was successful [17].

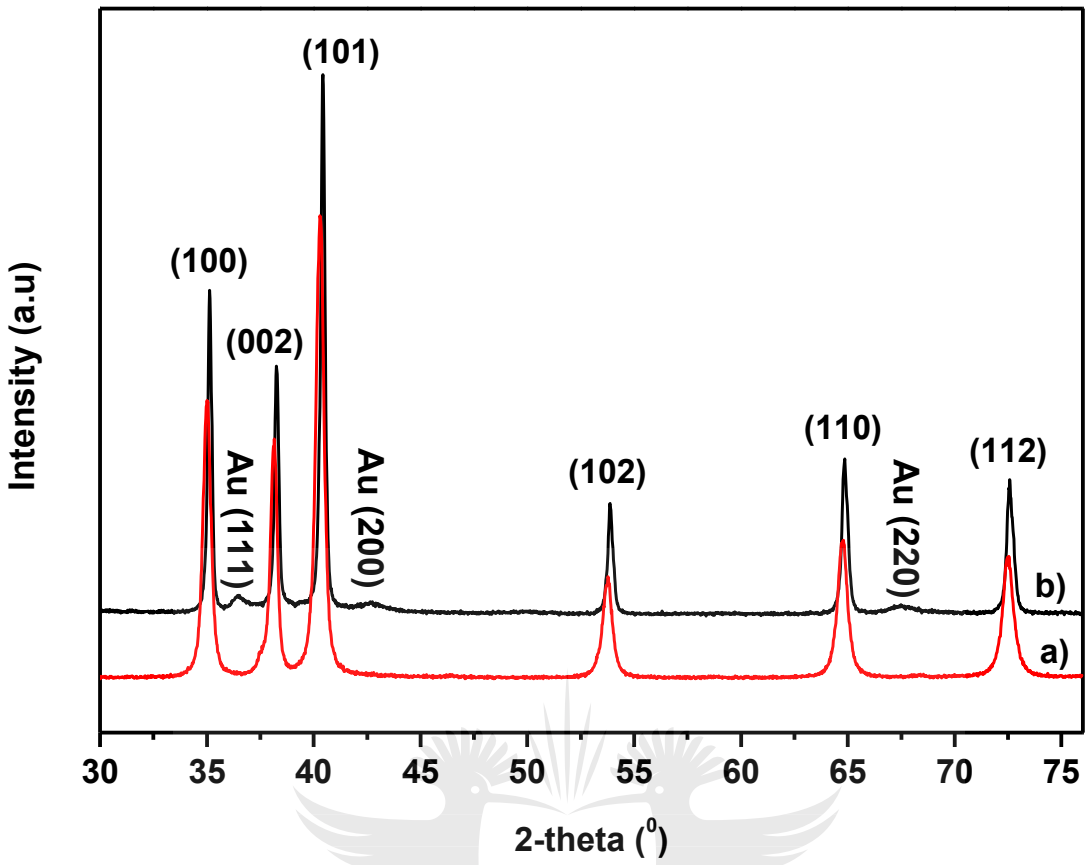

Figure 6.1: XRD patterns of (a) ZnO and (b) Au/ZnO samples

Figure 6.2 depicted TEM image of Au/ZnO composite. The TEM image showed the Au nanoparticles within the ZnO nanosheets. The AuNPs were well dispersed throughout the ZnO nanosheets suggesting that the synthesis of the composite was successful. Well dispersed AuNPs within the composite increases the reactivity of the composite, since the average size is kept constant, even though there was a slight clustering of nanoparticles as shown in Figure 6.2 represented by C-AuNPs. The AuNPs are attached on the surface of the ZnO nanosheet and are not attached on the edges of the nanosheets, which has a potential for uniform reactivity [13] and spill-over effect of the composite [15-17]. There appears to be relatively good adhesion between AuNPs and the ZnO nanosheets since there were no AuNPs that were found outside the ZnO nanosheets which may make the composite more stable [15]. The addition of the AuNPs is expected to increase the surface area of the ZnO nanosheet and spill over some of its electrons to the ZnO nanosheets which can improve its sensitivity and response time. However, there are more factors that affect gas sensing performance such as electrical conductivity, porosity, binding sites of material and interaction of the material with the analyte gas (chemisorption and physisorption) [17].

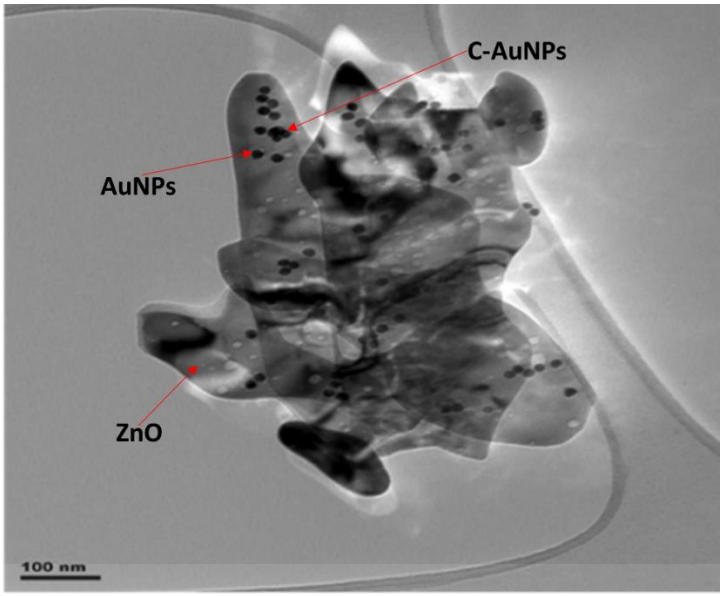

Figure 6.2: TEM image of Au/ZnO composite

6.3.2 Part B: Zinc Oxide (ZnO) Incorporated with Carbon Nanotubes (CNTs) composite (CNTs/ZnO)

Figure 6.3 showed the XRD patterns of (a) pure ZnO and (b) CNTs/ZnO composite. The XRD pattern of CNTs/ZnO composite showed diffraction peaks at a 2-theta angle of 27^0 (001) 34^0 (100), 37^0 (002), 39^0 (101), 52^0 (102), 64^0 (110) and 71^0 (112). The peak at 27^0 (001) was consistent with the presence of pure CNTs in the sample as shown by the XRD of CNTs (Figure 4.8) [4], which suggest that the composite was successfully made. The other peaks were indexed to pure ZnO (Figure 5.5) suggesting that the crystalline structure of the ZnO was not affected during the incorporation of CNTs [4].

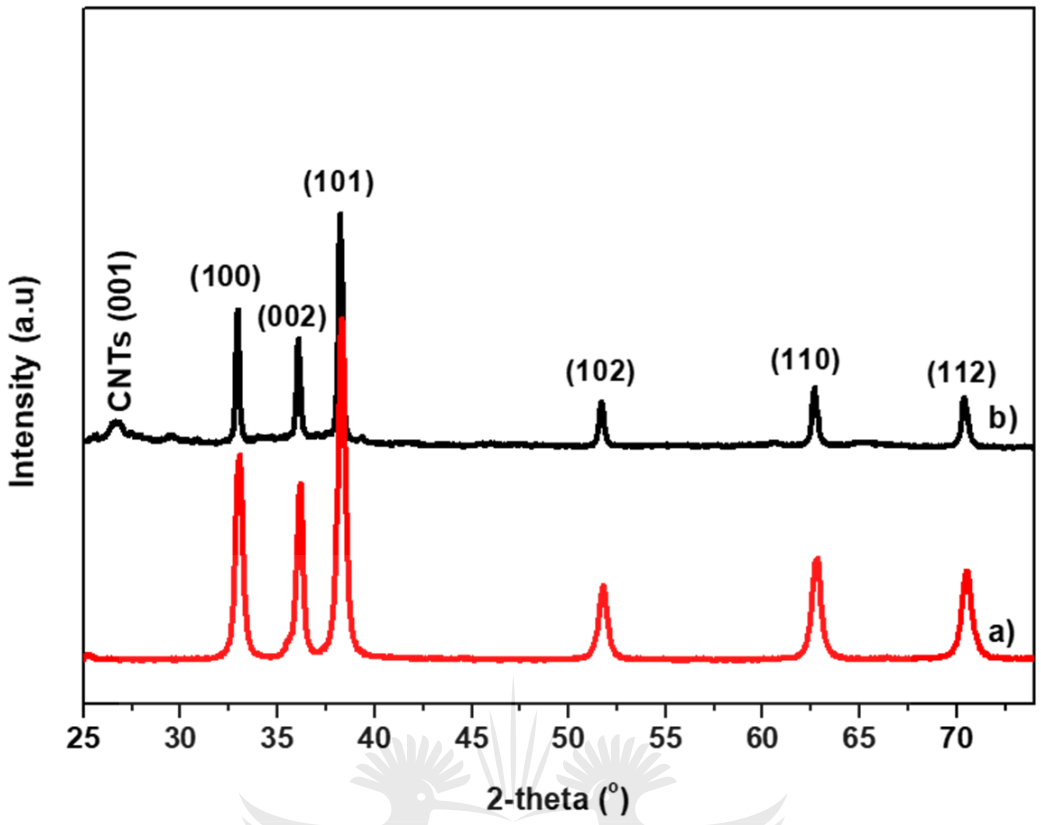

Figure 6.3: XRD pattern of (a) pure ZnO and (b) CNTs/ZnO composite

Figure 6.4 showed the TEM image of CNTs/ZnO. The image showed the ZnO nanosheets attached to the walls of the CNTs. It is evident that the ZnO is attached to the walls of the CNTs and this is because the CNTs are larger in size. Some of the ZnO nanosheets were not entirely attached to the walls of CNTs due to the concentration ratio of the ZnO nanosheets to CNTs, which was 95% ZnO nanosheets. The surface area of the CNTs/ZnO is expected to be higher than that of the ZnO, because of the hollow nature of the CNTs [2, 7]. High electron density of CNTs through SP^2 hybridisation makes them highly electron-conducting, this is ideal for improving the response time and sensitivity for ZnO nanosheets [6].

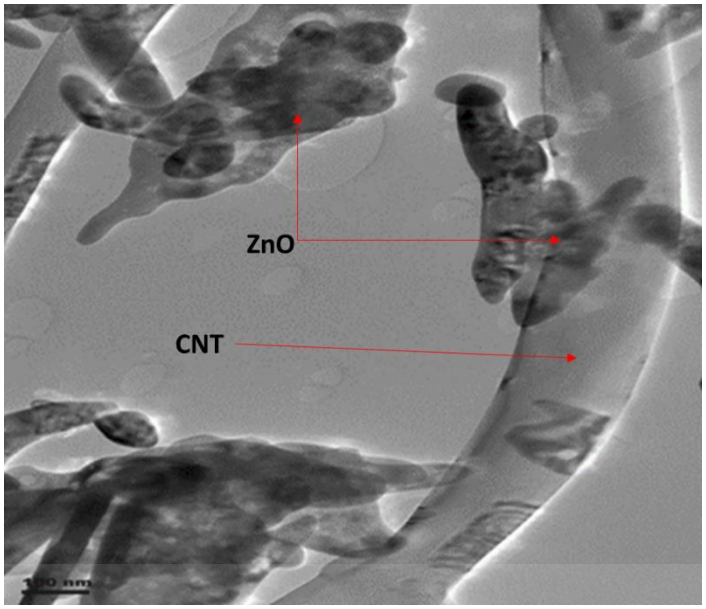

Figure 6.4: TEM image of CNTs/ZnO composite

6.3.3 Part C: BET and Gas Sensing of Au/ZnO and CNTs/ZnO Composites.

Table 6.1 showed specific surface areas (S_{BET}) of ZnO, Au/ZnO and CNTs/ZnO. There was a noticeable increase in the surface area of the ZnO nanosheets with the addition of AuNPs and CNTs. The surface area increased from 102 to 131 m^2/g with the addition of Au and 102 to 153 m^2/g with the addition of CNTs. Figure 6.5 showed a graphical presentation of specific surface areas (S_{BET}) of ZnO, Au/ZnO composite and CNTs/ZnO composite. The CNTs/ZnO showed the highest surface area as compared to pure ZnO and Au/ZnO. This is due to the hallow nature of the CNTs resulting in a higher surface area [7]. The surface area of CNTs has been reported in the literature to be around 150 m^2/g [16]. The Au nanoparticles at low loadings do not affect the surface area of the material, however, at the Au loading of 5 w/w%, the Au particles start to increase the surface, possibly due to their concentration and size.

Table 6.1: Specific surface area of ZnO, Au/ZnO composite and CNTs/ZnO composite

Samples	**Surface Area (m^2/g)**
ZnO	102
Au/ZnO	131
CNTs/ZnO	153

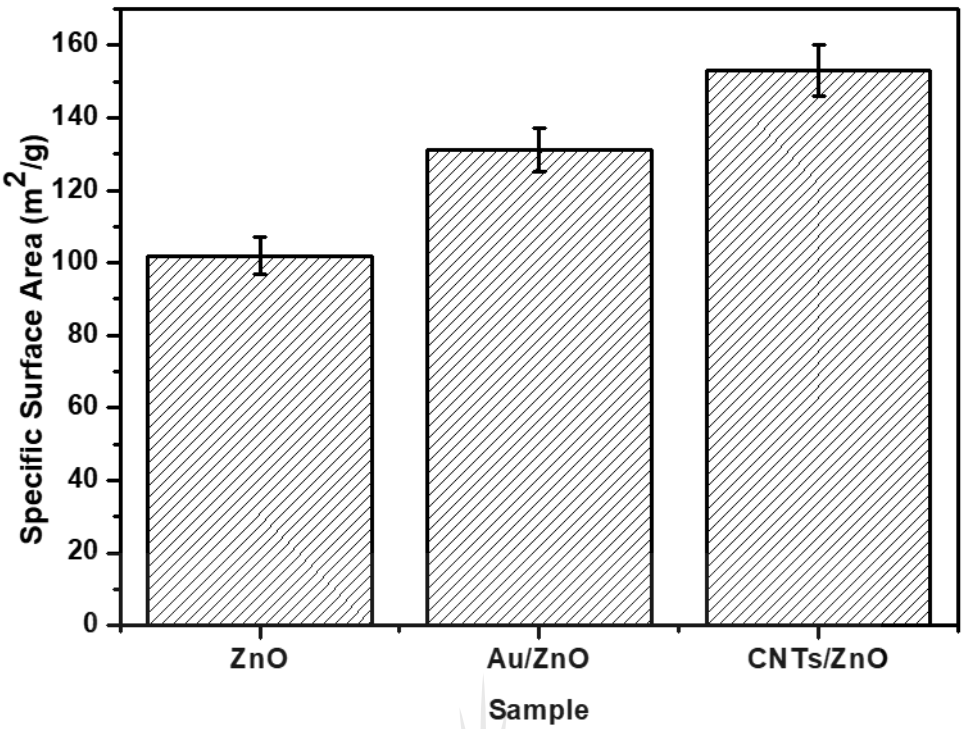

Figure 6.5: Specific surface areas (S_{BET}) of ZnO, Au/ZnO and CNTs/ZnO

Figure 6.6 showed the electrical conductivity changes of Au/ZnO, CNTs/ZnO and CNTs in the presence and absence of analyte gas (CO) with varying concentrations. To investigate the effect of nanomaterials addition on the sensor performance, different sensors with surface modifications were tested. The analyte gas was varied from 10 to 200 ppm for all the samples and the temperature was kept constant at 250^0C as it is the lowest reported temperature in the application of gas sensors. The temperature of 250^0C was preferred over room temperature because at high temperature there is improved mobility of the electrons for ZnO semiconductor [15]. The electrical conductivity increased when the samples were exposed to CO gas throughout the concentrations range. The increase in electrical conductivity when the sensor was exposed to CO (reducing gas), suggests that the composites behaved as an n-type semiconductor, similarly to pure ZnO [17].

The exposure of the ZnO nanosheets in synthetic air causes free oxygen molecules to be absorbed in the surface. The absorbed oxygen captures electrons from the surface of ZnO leading to the formation of oxygen ions [18]. After the formation of oxygen ions, the electrical resistance increases, due to the formation of depletion layers on the ZnO surface. Exposing ZnO electron depleted surface to a reducing gas (CO), induces a reaction between CO and O^{2-} and subsequently forming CO_2 [17]. The formation of the CO_2 molecules decreases the concentration of the oxygen ions on the surface of the ZnO sensor leading to an increase in the

concentration of electrons in the surface of ZnO, which subsequently made the depletion layer thinner, hence an increase in electrical conductivity as depicted in Figure 6.6 [18].

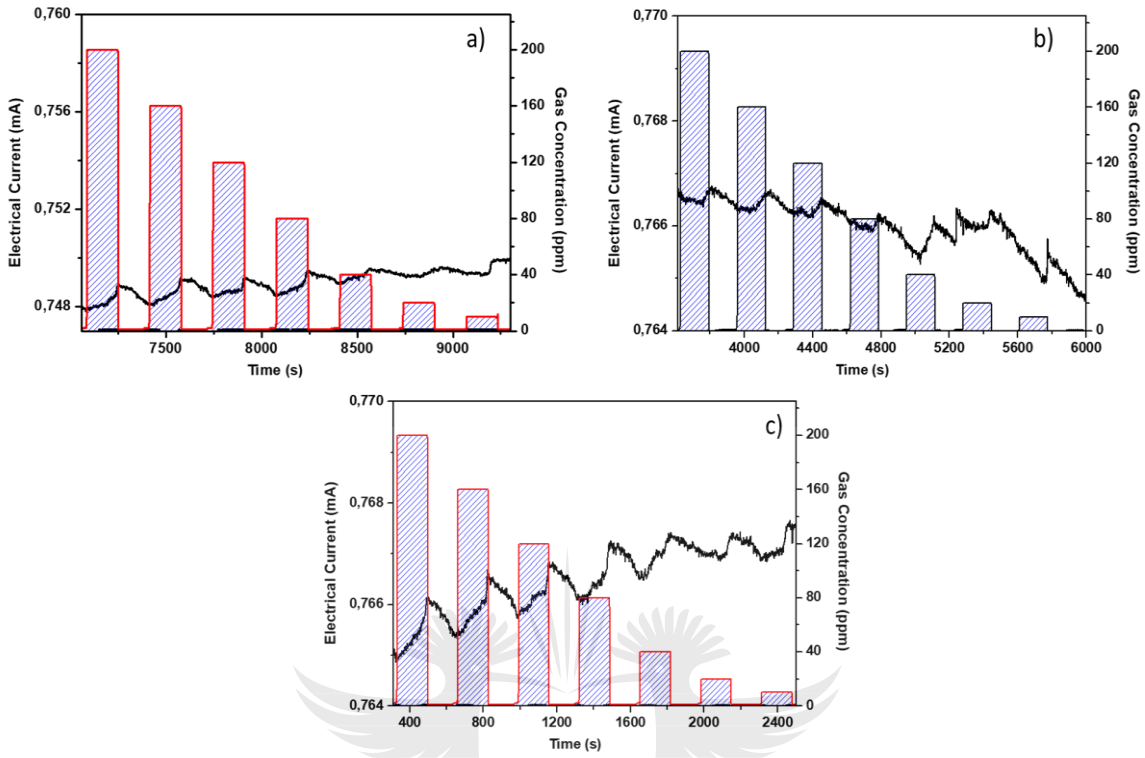

Figure 6.6: Electrical conductivity changes of a) Au/ZnO, b) CNTs/ZnO and c) CNTs when exposed to different concentrations of CO gas.

Figure 6.7 showed the graph of sensitivity of various sensors versus the CO concentration of 200 ppm since it had the highest sensitivity for pure ZnO (Chapter 4). Sensitivity was calculated (Equation 5.1) to be 9.97, 9.96, 9.99 and 9.98% for ZnO, Au/ZnO, CNTs/ZnO and CNTs respectively. The sensitivity of the sensor depends on the interaction between the analyte gas and the surface of the sensing material. This explains the observed differences in the sensitivity values for different samples (Au/ZnO, CNTs/ZnO and CNTs) which can be related to differences in the morphology of the material. The morphology affects the surface area and surface defects resulting in different sensitivity values. The mechanism of sensitivity can be explained in terms of the chemisorbed oxygen molecules [18]. The more chemisorbed oxygen molecules on the surface of the sensor the better the sensitivity. However, the adsorption of these oxygen molecules depends on other factors, such as material porosity. A large surface area leads to more chemisorbed oxygen molecules resulting in increased sensitivity [18]. Hence different morphologies showed different sensitivity values because they exhibited different surface areas. This explains the reason the sensitivity value of the CNTs/ZnO (9.99%) is

relatively higher than ZnO nanosheets and Au/ZnO composite. This is because the CNTs/ZnO has the highest surface area resulting in a larger quantity of the O^-ions being absorbed.

Guo *et al* [12] investigated the effect of AuNPs loading on the ZnO nanorods. The study showed that thinner nanorods exhibited higher sensitivity as compared to thicker nanorods, and this is because thinner nanorods had a larger effective surface area resulting in more chemisorbed oxygen molecules. The study also demonstrated that the addition of Au in the ZnO nanorods improved the gas sensor performance.

Based on Figure 6.7, it is apparent the CNTs/ZnO composite showed better sensitivity followed by the CNTs. The BET surface area (Figure 6.5) studies showed that the CNTs/ZnO had the highest surface area of 153 m^2/g compared to ZnO nanosheets and Au/ZnO composite at 102 and 130 m^2/g respectively. Therefore, the better sensitivity can be explained in terms of the surface area, whereby the high surface area of CNTs/ZnO resulted in more chemisorbed oxygen molecules which led to better sensitivity. Both the CNTs/ZnO and CNTs exhibited better sensitivity as compared to bare ZnO nanosheets and Au/ZnO. These differences are mainly due to the hollow nature of the CNTs resulting in higher surface area. The Au/ZnO composite showed a lower sensitivity value compared to other samples. This might be due to the slight increase in AuNPs sizes due to clustering as observed in the TEM analysis (Figure 6.2).

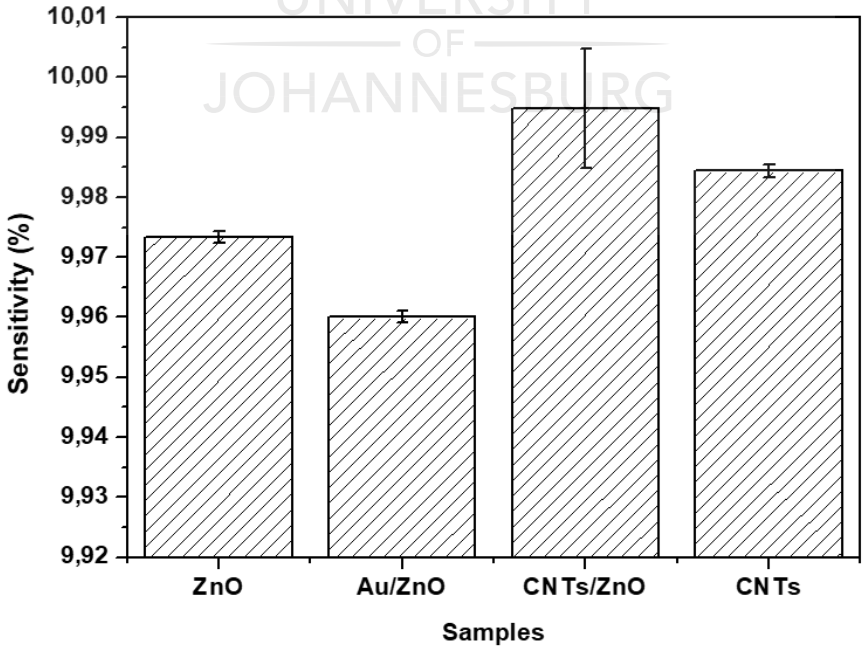

Figure 6.7: Sensitivity (%) of ZnO, Au/ZnO, CNTs/ZnO and CNTs exposed to a concentration of 200 ppm of CO gas

Figure 6.8 showed the graph of the response time of different samples (ZnO, Au/ZnO, CNTs/ZnO and CNTs) exposed to a gas concentration of 200 ppm. Response time is one of the important parameters in determining the performance of the gas sensor and it is defined as the time required to reach 90% of a stable electrical current after the gas exposure [17]. The CNTs/ZnO composite gave the fastest response time of 49 seconds as compared to other samples. Further showing the effect of surface area in the performance of the sensor, as the sample with the highest surface area showed the fastest response time. Pure ZnO nanosheets showed a faster response time compared to Au/ZnO composite, this might be due to the interaction between the AuNPs and the ZnO. The difference might be explained by the spill-over effect [15], whereby the amount and distribution of the AuNPs govern the performance of the Au/ZnO sensor. This effect only occurs when the AuNPs are well dispersed on the surface of the ZnO nanosheets (Figure 6.2), in this study the spill-over effect refers to the Au as a metal dissociated molecule that can spill over the surface of the ZnO. The mechanism of this process involves, first, the adsorption of molecules on the surface of the Au, and subsequently migrating to the surface of the ZnO nanosheets. The migrated molecules react with the oxygen species in the surface, hence the change in electrical conductivity [12-13]. However, more of the AuNPs in the surface can cause clustering which subsequently makes the spill-over effect less effective since fewer gas molecules can dissociate and spill over the ZnO nanosheets. Hence a relatively higher response time of the Au/ZnO as compared to bare ZnO nanosheets [16]. The CNTs/ZnO composite and CNTs both have the same surface area however, their response time differs as depicted in Figure 6.8. The difference in response times might be due to the electrons being transferred from the CNTs to the ZnO thus increasing the electrical conductivity of the material, while on CNTs alone, it does not have the ZnO effect hence having a longer response time.

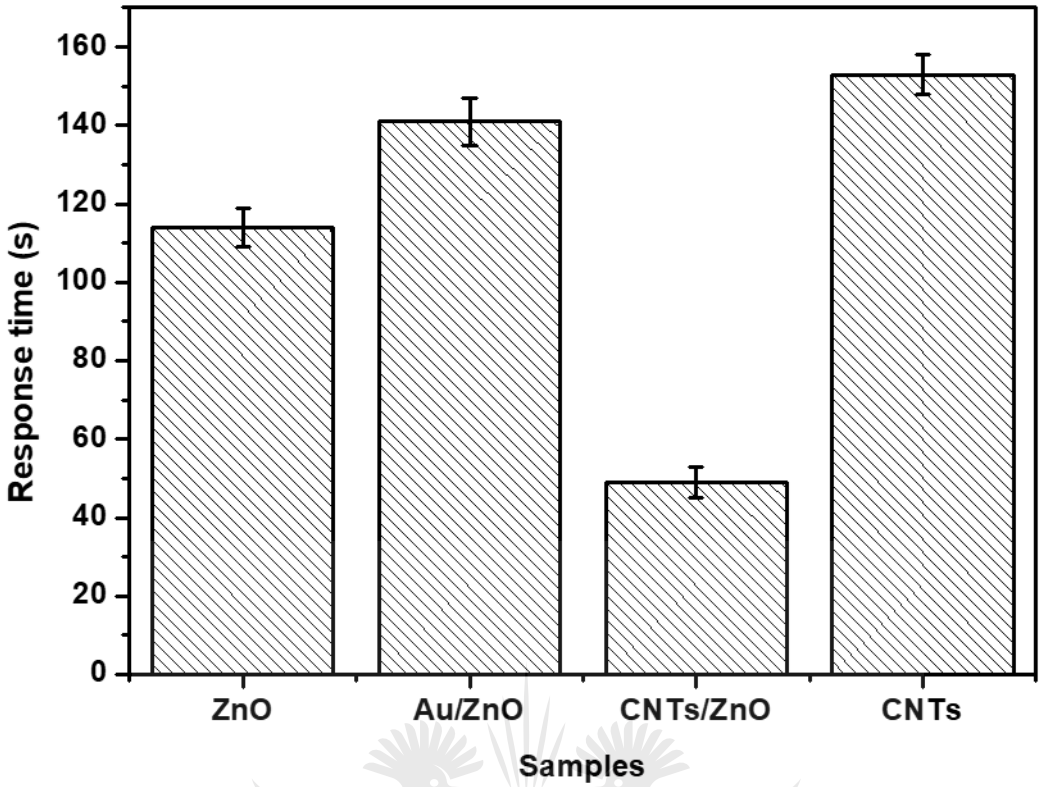

Figure 6.8: Response time of different sensors exposed to CO gas concentration of 200 ppm

6.4 Conclusion

The Au/ZnO composite was successfully synthesised by mixing the ZnO nanosheets with AuNPs (14 nm). The characterisation showed that neither AuNPs nor ZnO crystal structure was altered during the incorporation. The AuNPs were well dispersed in the ZnO nanosheet. The Au/ZnO had a higher surface area than ZnO nanosheets alone. The synthesis of the CNTs/ZnO composite was successful. Both the pure ZnO and CNTs were not changed during synthesis of the composite, further suggesting that both retained their crystal structure. The ZnO nanosheets were attached on the walls of the CNTs. The CNTs/ZnO composite had a higher surface area as compared to the ZnO nanosheet before incorporation. The CNTs/ZnO composite showed an improved sensitivity and response time as compared to bare ZnO, suggesting that making composite with the CNTs improved the material.

6.5 References

[1] Park, S., Kim, S., Kheel, H., Park, S. and Lee, C. (2015). Synthesis and hydrogen gas sensing properties of TiO_2-decorated CuO nanorods. Bulletin of the Korean Chemical Society, 36(10), pp.2458-2463.

[2] Leghrib, R., Llobet, E., Pavelko, R., Vasiliev, A., Felten, A. and Pireaux, J. (2009). Gas sensing properties of MWCNTs decorated with gold or tin oxide nanoparticles. Procedia Chemistry, 1(1), pp.168-171.

[3] Wang, S., Li, Z., Wang, P., Xiao, C., Zhao, R., Xiao, B., Yang, T. and Zhang, M. (2014). Facile synthesis and enhanced gas sensing properties of In_2O_3 nanoparticle-decorated ZnO hierarchical architectures. CrystEngComm, 16(25), pp.5716-5723.

[4] Kwon, Y., Mirzaei, A., Kang, S., Choi, M., Bang, J., Kim, S. and Kim, H. (2017). Synthesis, characterization and gas sensing properties of ZnO-decorated MWCNTs. Applied Surface Science, 413, pp.242-252.

[5] Korotcenkov, G., Han, S. and Cho, B. (2016). Metal Oxide Nanocomposites: Advantages and Shortcomings for Application in Conductometric Gas Sensors. Materials Science Forum, 872, pp.223-229.

[6] Ju, W., Li, T., Zhou, Q., Li, H. and Li, X. (2018). First-principles study of Au-decorated carbon nanotubes. Physica E: Low-Dimensional Systems and Nanostructures, 101, pp.273-277.

[7] Kumar, D., Chaturvedi, P., Saho, P., Jha, P., Chouksey, A., Lal, M., Rawat, J., Tandon, R. and Chaudhury, P. (2017). Effect of single wall carbon nanotube networks on gas sensor response and detection limit. Sensors and Actuators B: Chemical, 240, pp.1134-1140.

[8] Batzill, M. and Diebold, U. (2007). Surface studies of gas sensing metal oxides. Physical Chemistry Chemical Physics, 9(19), p.2307.

[9] Motaung, D., Mhlongo, G., Bolokang, A., Dhonge, B., Swart, H. and Sinha Ray, S. (2016). Improved sensitivity and selectivity of pristine zinc oxide nanostructures to H_2S gas: Detailed study on the synthesis reaction time. Applied Surface Science, 386, pp.210-223.

[10] Geng, L. (2010). Gas sensitivity study of polypyrrole/WO_3 hybrid materials to H_2S. Synthetic Metals, 160(15-16), pp.1708-1711.

[11] Sarala Devi, G., Manorama, S. and Rao, V. (1995). High sensitivity and selectivity of a SnO_2 sensor to H_2S at around 100 °C. Sensors and Actuators B: Chemical, 28(1), pp.31-37.

[12] Hosseini, Z., Mortezaali, A., Iraji zad, A. and Fardindoost, S. (2015). Sensitive and selective room temperature H_2S gas sensor based on Au sensitized vertical ZnO nanorods with flower-like structures. Journal of Alloys and Compounds, 628, pp.222-229.

[13] Zak, A., Abrishami, M., Majid, W., Yousefi, R. and Hosseini, S. (2011). Effects of annealing temperature on some structural and optical properties of ZnO nanoparticles prepared by a modified sol–gel combustion method. Ceramics International, 37(1), pp.393-398.

[14] Gao, X. and Zhang, T. (2018). An overview: Facet-dependent metal oxide semiconductor gas sensors. Sensors and Actuators B: Chemical, 277, pp.604-633.

[15] Dai, H., Feng, N., Li, J., Zhang, J. and Li, W. (2019). Chemiresistive humidity sensor based on chitosan/zinc oxide/single-walled carbon nanotube composite film. Sensors and Actuators B: Chemical, 283, pp.786-792.

[16] Govardhan, K. and Grace, A. (2016). Metal/metal oxide doped semiconductor based metal oxide gas sensors—A Review. Sensor Letters, 14(8), pp.741-750.

[17] Shingange, K., Tshabalala, Z., Ntwaeaborwa, O., Motaung, D. and Mhlongo, G. (2016). Highly selective NH_3 gas sensor based on Au loaded ZnO nanostructures prepared using microwave-assisted method. Journal of Colloid and Interface Science, 479, pp.127-138.

[18] Firooz, A. (2017). Fabrication of highly selective sensor based on Mn-doped ZnO nanostructures. Nano Research and Applications, 03(03) pp.1345-1350

CHAPTER 7

7.0 General Conclusions and Recommendations

7.1 Conclusions

The formation of ZnO nanostructures was achieved by microwave digestion method using different concentrations of NaOH. It was found that different concentrations of NaOH affect the morphology of the ZnO. ZnO nanostructures such as hexagonal, flower-like and sheets-like were achieved. The nanosheets showed the highest surface area compared to other nanostructures. The ZnO was tested for gas sensing capabilities and showed a response time of 144 seconds when exposed to 200 ppm of CO gas.

AuNPs were synthesised using gold salt as the metal precursor and citrate was used as both a reducing agent and stabiliser. Spherical AuNPs with sizes of 14, 30 and 40 nm were successfully synthesized by systematically varying the concertation of citrate. Carbon nanotubes were synthesised using ferrocene as a catalyst and acetylene as the carbon source. Average size of 95 nm of CNTs was achieved by varying the flowrate of acetylene gas into the chemical vapour deposition furnace.

The two additives (AuNPs and CNTs) were synthesised in order to make composites with the ZnO. The composites showed an increased surface area compared to pure ZnO, however, the CNTs/ZnO composite showed the highest surface area of them all. The gas sensing performance of the composites was investigated and CNTs/ZnO composite showed the fastest response time of 49 seconds when exposed to 200 ppm CO gas.

7.2 Recommendations

The following are recommended for future studies to fully understand the behaviour of ZnO:

- Detailed characterisation techniques Photoluminescence (PL) and high-resolution TEM to investigate the d-spacing and fringes (crystal planes) and compare with XRD data.
- Investigate the effect of different AuNPs and CNTs loadings on ZnO nanosheets.
- Investigate more gas sensing parameters such as selectivity of ZnO based gas sensor.
- Investigate the interaction between Au-ZnO and CNTs-ZnO, since these will have implications on the reproducibility of the ZnO based gas sensor.
- Conduct molecular modelling of the ZnO composites and the analyte gas to investigate the binding sites.

- Perform BET long scans to obtain isotherms for calculating properties such as pore shapes and binding sites.

Appendices

Appendix A: Technical Trainings

- Microsoft Excel: Spreadsheet as an Engineering Tool, Mintek, Randburg, **28-29 May 2018**.
- Mastering Business Communication Training, Mintek, Randburg, **21-22 June 2018**.
- Project Management Training, Mintek, Randburg, **21-23 August 2018**.
- Presentation Techniques Training, Mintek, Randburg, **03-04 October 2018**.

Appendix B: Calcination temperature optimization

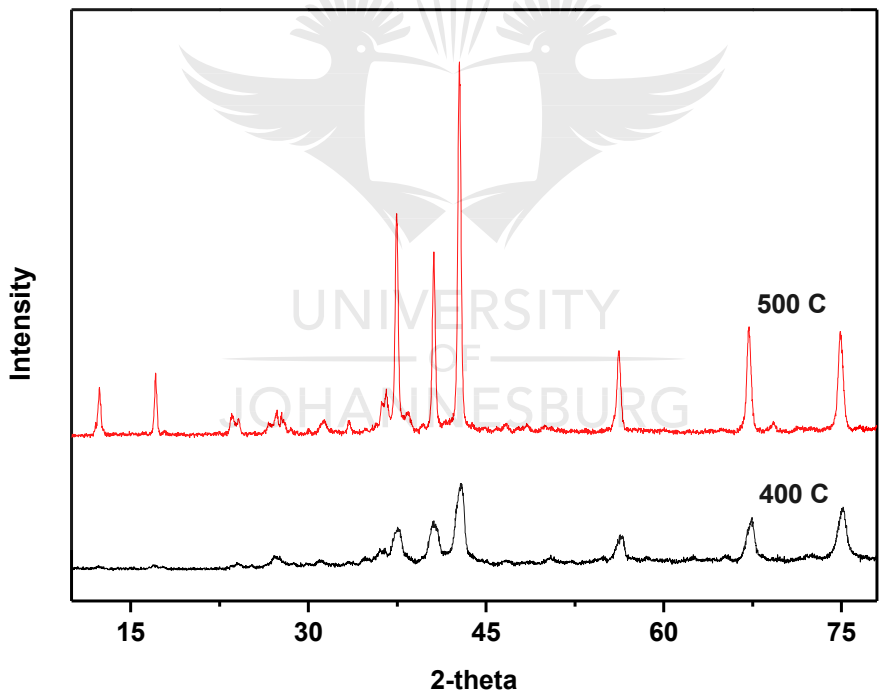

Figure 1B: The calcination temperature study of ZnO

Appendix C: Concentration study of $ZnSO_4$

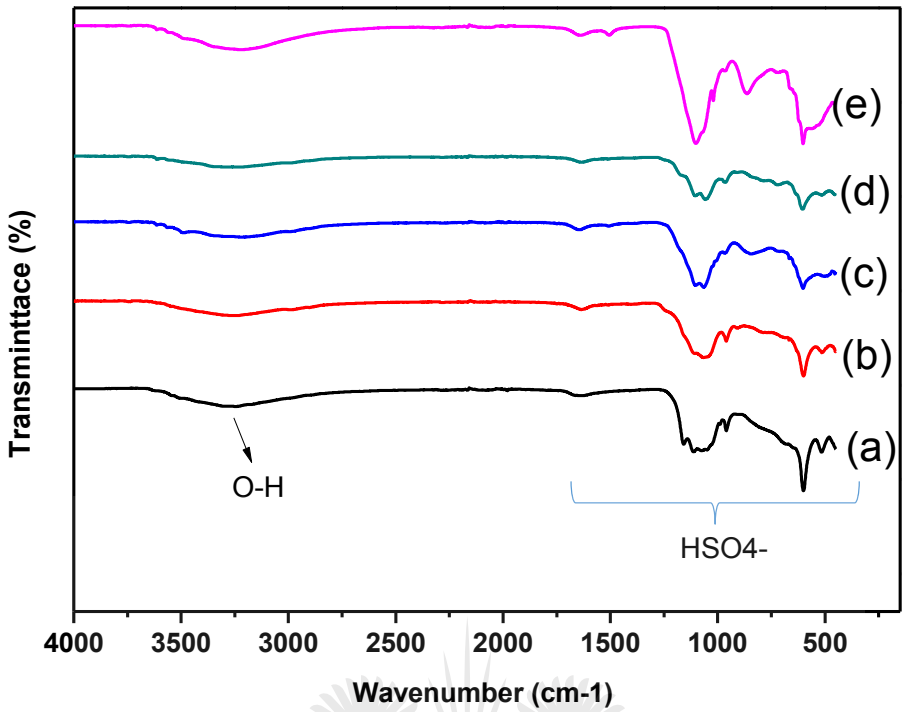

Figure 2C: FTIR spectra of ZnO synthesised using $ZnSO_4$ concentrations of (a) 0.1 M, (b) 0.2 M, (c) 0.3 M, (d) 0.4 M and (e) 0.5 M

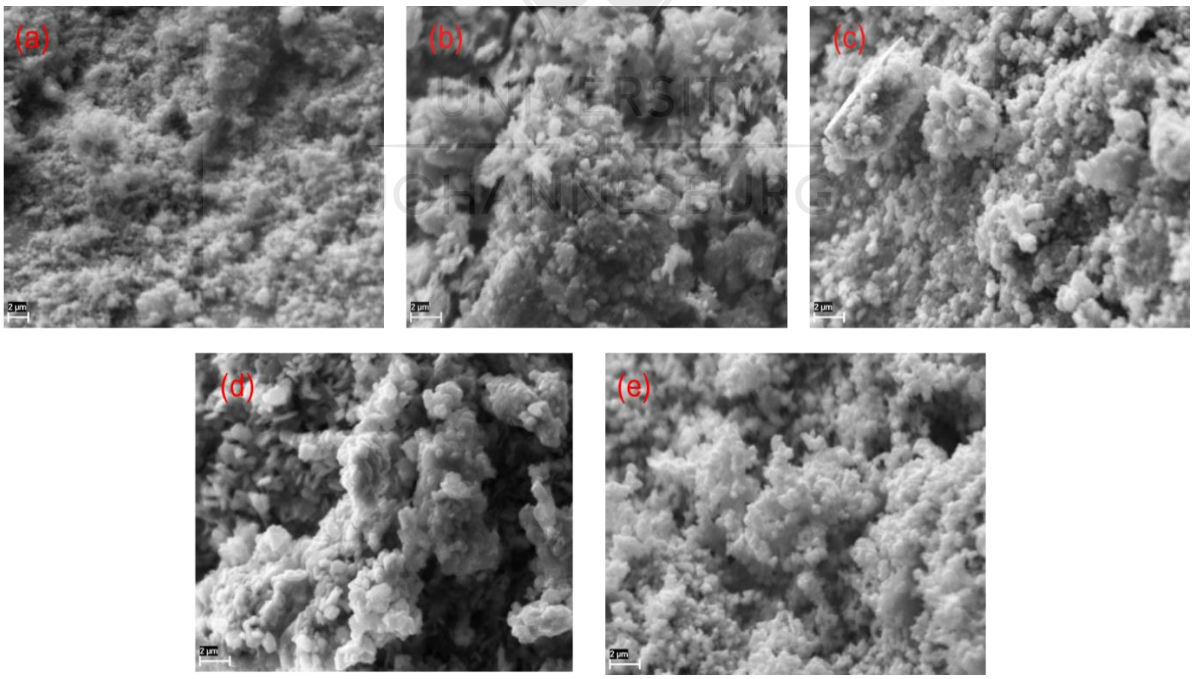

Figure 3C: SEM images of ZnO synthesised using NaOH concentrations of (a) 0.1 M, (b) 0.2 M, (c) 0.3 M, (d) 0.4 M and (e) 0.5 M

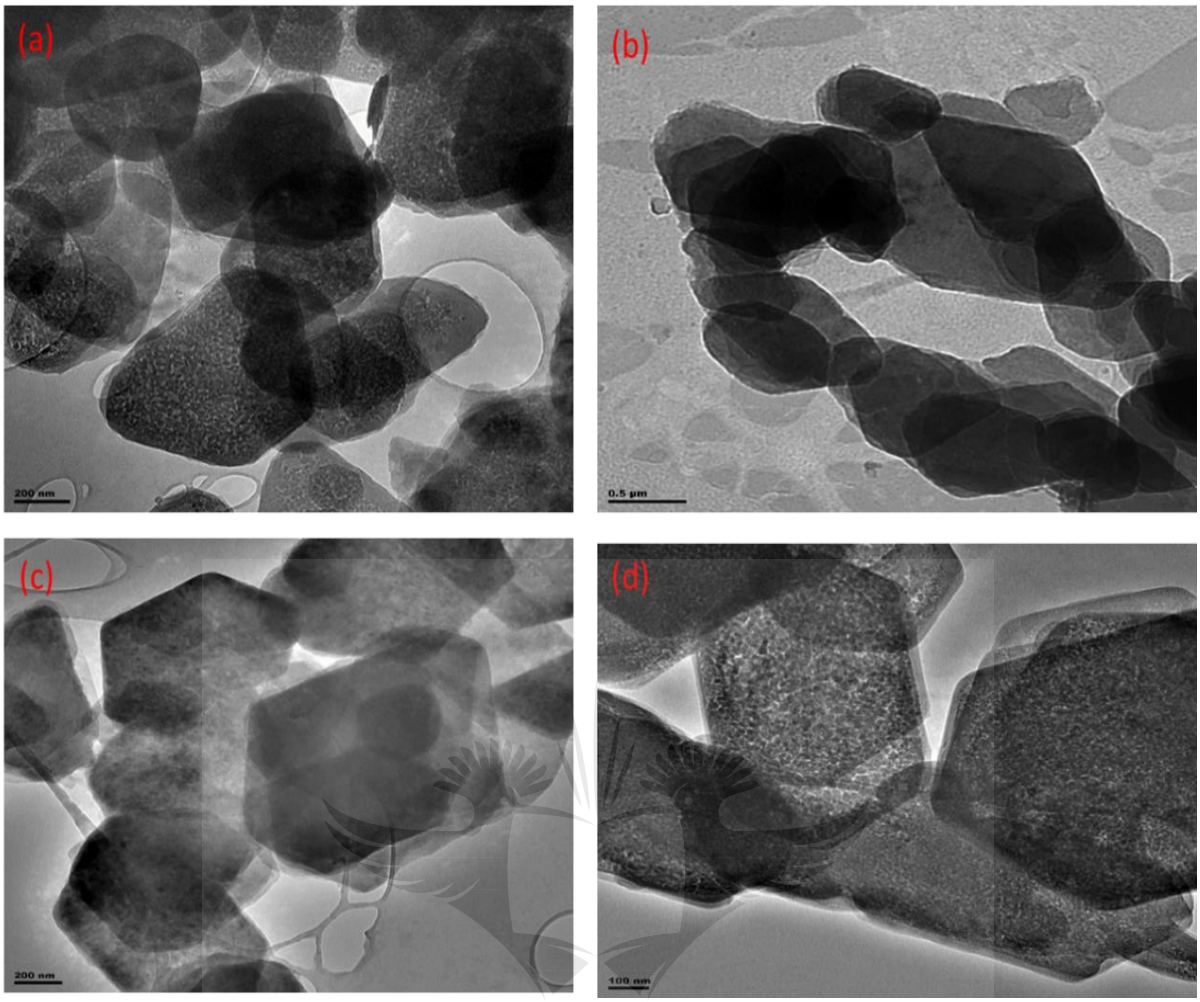

Figure 4C: TEM images of ZnO synthesised at different temperatures with 0.1 M of ZnSO4 and NaOH at (a) 40^0 C, (b) 60^0 C, (c) 80^0 C and (d) 100^0 C

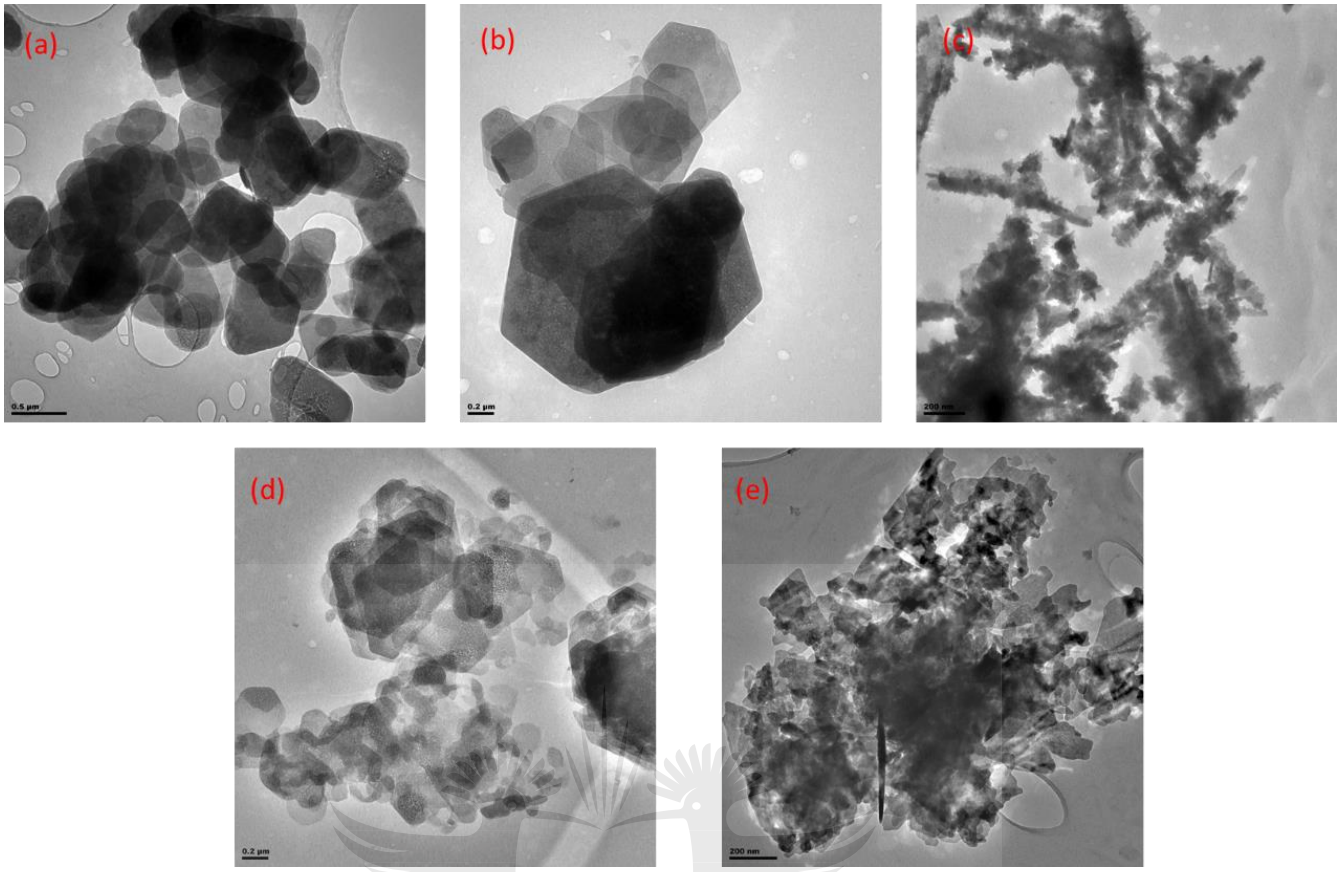

Figure 5C: TEM images of ZnO synthesised using $ZnSO_4$ concentrations of (a) 0.1 M, (b) 0.2 M, (c) 0.3 M, (d) 0.4 M and (e) 0.5 M